U.PORTO
FACULDADE DE CIÊNCIAS
UNIVERSIDADE DO PORTO

PhD

PhD

PhD

Probing Particle Physics With Gravitational Waves

David Grüber

Thesis carried out as part of the Doctor's Degree in Astronomy

Institute of Astrophysics and Space Sciences

2025

Supervisor
Lara Sousa, Institute of Astrophysics and Space Sciences

Co-supervisor
Pedro P. Avelino, Institute of Astrophysics and Space Sciences

Acknowledgements

Moving to the beautiful city of Porto and spending the last couple of years here to work on this thesis was a huge undertaking that I never could have managed on my own. Below is an (incomplete) list of people who have contributed to making this possible.

First of all, I would like to thank my supervisors, Lara Sousa and Pedro Avelino, for sharing their knowledge and expertise and continuously helping me with invaluable advice and fresh ideas to advance my work. While consistently pushing me to grow, they were never overly demanding and always friendly on a personal level, which surely was key to bringing my PhD to a successful end. My gratitude also goes to the Instituto de Astrofísica, which not only provided all the necessary working conditions but also made it possible to connect with experts from various fields within astrophysics.

Next, of course, I would like to thank my family, Pia and Christoph, who steadily helped me in all possible ways during this long stay abroad and visited me here regularly. Their support was crucial in ensuring that I had the best possible conditions to pursue this doctorate. My stay here would have been far more challenging as well without my good friends Natacha and Markus, whom I could always count on and share countless joyful moments with. The same clearly holds true for my friends back in Germany, who stayed in close contact and honored me with their visits.

I would also like to thank the students from CAUP's cosmology group — namely, Sergei, Ricarda, and Clara — as well as all the other PhD students of IA, with whom I not only engaged in many interesting discussions but also shared nice experiences at one or another conference or outside the academic setting. Among them, I would like to especially highlight José, who has been a close friend ever since we attended the machine learning lecture at the beginning of our PhDs together, who taught me so much about our night sky and astrophotography, and with whom I spent uncountable memorable adventures in and outside of Porto.

Furthermore, I would like to thank Paul Tol for developing and providing the colorblind-friendly color schemes [1] used in many of the plots within this thesis. Over the past four years, I was supported by the Fundação para a Ciência e a Tecnologia (FCT) through the PhD fellowship 2020.07632.BD. Funding for this work has also been provided by FCT through national funds (PTDC/FIS-PAR/31938/2017 and 2022.03495.PTDC).

Resumo

As paredes de domínio, defeitos topológicos bidimensionais que podem surgir em transições de fase com quebra espontânea de simetria no universo primordial, servem como ponte entre a cosmologia e a física de partículas e podem, assim, proporcionar-nos uma oportunidade única de sondar teorias além do Modelo Padrão da Física de Partículas. No contexto cosmológico, as paredes de domínio formariam redes extensas, que tipicamente evoluiriam para um regime invariante de escala, com sensivelmente uma parede por região de Hubble. No entanto, as observações astrofísicas restringem fortemente as redes estáveis de paredes de domínio que subsistam até aos dias de hoje impondo que sejam muito leves. Mas, estas paredes também podem decair mais cedo na evolução do universo por diversos mecanismos, conseguindo assim contornar estes limites rigorosos. É o que sucede, por exemplo, no caso de paredes de domínio enviesadas (*biased domain walls*), previstas em muitas teorias além do Modelo Padrão. Essas paredes podem ter tido um papel cosmológico mais relevante e, por isso, ser mais fáceis de detetar. Um elemento crucial para compreender possíveis assinaturas observacionais das redes de paredes de domínio é uma caracterização rigorosa da sua dinâmica. Esta tese explora os aspetos teóricos, numéricos e observacionais da evolução de paredes de domínio, focando-se especialmente nas suas assinaturas em ondas gravitacionais.

Começamos por apresentar uma panorâmica do modelo cosmológico padrão e do papel dos campos escalares na física do universo primordial, salientando a sua ligação com defeitos topológicos. Exploramos a formação destes defeitos e discutimos o estado da arte no que respeita à física de paredes de domínio. Nesse contexto, revemos o modelo de uma escala dependente da velocidade (*Velocity-dependent One-scale Model*), que se tornou o modelo analítico padrão para descrever a dinâmica de redes de paredes de domínio em larga escala, bem como o modelo não paramétrico (*Parameter Free Model*) que foi introduzido mais recentemente.

As simulações de teoria de campos tornaram-se numa das ferramentas mais essenciais para o estudo da dinâmica das paredes, já que permitem não só testar e refutar as previsões de modelos, mas também aprofundar a compreensão de aspetos da dinâmica de paredes de domínio que ultrapassam a capacidade descritiva das abordagens analíticas. Implementar simulações de teoria de campos em *Python* foi, por isso, um dos objetivos iniciais do meu doutoramento, tendo estas sido uma base importante para muitos dos trabalhos subsequentes. Um capítulo desta tese descreve o algoritmo que utilizámos e

a forma como optimizámos o código para maximizar o desempenho em sistemas comparáveis a computadores pessoais. Nesse mesmo capítulo, examinamos os diferentes métodos de extração do comprimento característico — uma quantidade termodinâmica usada para descrever a dinâmica de redes em larga escala —– e analisamos as suas propriedades e interpretação física. Identificámos, assim, uma dependência implícita dessas medições de comprimento na velocidade quadrática média da rede de domínio, o que nos permitiu introduzir um método inovador e computacionalmente económico para medir esta grandeza.

Em seguida, exploramos o modelo não-paramétrico, que pode ser utilizado para estimar a velocidade quadrática média e o comprimento característico em redes de paredes de domínio. Derivamos aproximações analíticas que permitem calcular estas variáveis em dois limites distintos: primeiro, num fundo estático semelhante ao espaço-tempo de Minkowski, e depois num universo em expansão rápida (mas ainda decelerada). Isto permitiu-nos desenvolver uma função de ajuste simples que faz a interpolação entre estes casos limite e que descreve o comprimento característico e a velocidade quadrática média para uma vasta gama de taxas de expansão (incluindo os regimes cosmologicamente mais relevantes de domínio de matéria e de radiação). Aprofundamos de seguida a comparação entre o modelo não paramétrico e o modelo de uma escala dependente da velocidade em universos em rápida expansão e demonstramos que ambos os modelos são consistentes nesse limite. Como já havia sido salientado na literatura, em regimes de expansão mais lenta há discrepâncias significativas entre as previsões do modelo não paramétrico e os resultados das simulações. Para investigar essas discrepâncias, realizámos simulações de teoria de campos do colapso de paredes de domínio cilíndricas e esféricas, já que este é o fenómeno em que se baseia a descrição da dinâmica das redes no modelo não paramétrico.

Para obter uma visão mais abrangente, analisamos também outros modelos de paredes de domínio. No capítulo 5, introduzimos um modelo simples em que as paredes de domínio interagem não minimamente com distribuições compactas de matéria. Examinamos de que forma os parâmetros de acoplamento podem afetar o resultado das colisões entre paredes e esses objetos, desenvolvemos um modelo analítico simples que prevê se uma parede atravessará o objeto ou, em alternativa, será refletida, e testamos estas previsões com simulações. Ainda nesse capítulo, estudamos outro fenómeno associado à dinâmica das paredes de domínio: a possibilidade de ocorrer uma transição de fase cosmológica tardia induzida pelo colapso de domínios de falso vácuo num potencial ϕ^6

modificado.

Um dos pilares fundamentais desta tese é o estudo da emissão de ondas gravitacionais pelas paredes, abordado no capítulo 6. Desenvolvemos um novo modelo semianalítico para calcular o Fundo Estocástico de Ondas Gravitacionais emitido por redes de paredes de domínio sem fricção, complementando os trabalhos existentes na literatura, que em grande medida se baseiam em estimativas oriundas de simulações numéricas. Obtivemos também expressões analíticas capazes de descrever essa emissão durante as eras de matéria e de radiação com excelente precisão, e analisámos as possíveis assinaturas de uma rede que decai devido ao enviesamento (*bias*). Posteriormente, comparamos os nossos resultados com as restrições observacionais atuais resultantes da radiação cósmica de fundo e de experiências de cronometragem de pulsares (*Pulsar Timing Arrays*), discutindo as implicações para as paredes de domínio enquanto potencial fonte do Fundo Estocástico de Ondas Gravitacionais recentemente detetado.

Palavras-chave: física, astronomia, cosmologia, defeitos cósmicos

Abstract

Domain walls, two-dimensional topological defects that may emerge in spontaneous symmetry breaking phase transitions in the early universe, serve as a bridge between cosmology and particle physics and might therefore provide a unique window to probe theories beyond the Standard Model of Particle Physics. In a cosmological setting, domain walls would form extended networks, which typically approach a scaling regime with roughly a single wall per Hubble patch. Stable domain walls that were to survive until the present day, however, are heavily constrained by astrophysical observations to be very light. Walls, on the other hand, could also decay earlier in the evolution of the universe through various mechanisms, in which case they could evade these strict limits on their mass scale. This is the case, for instance, for biased domain walls that are predicted in many relevant beyond standard model scenarios. These may then have played a more relevant cosmological role and might therefore be easier for us to detect. A crucial element in understanding possible observational signatures of domain wall networks is a precise characterization of their dynamics. This thesis explores the theoretical, numerical, and observational aspects of domain wall evolution, with a particular focus on their gravitational wave signatures.

We begin with an overview of the cosmological standard model and the role of scalar fields in early universe physics, emphasizing their connection to topological defects. We explore the formation of such defects and discuss the state-of-the-art understanding of domain wall physics. In this context, we review the Velocity-dependent One-Scale model, which has evolved to be the standard analytical model in describing large-scale dynamics of domain wall networks, as well as the more recent Parameter-Free Model.

Field theory simulations have become one of the most essential tools for studying the dynamics of walls. They can help to verify or falsify model predictions and improve our understanding of aspects of domain wall dynamics that go beyond the scope of analytic modeling. Implementing field theory simulations in *Python* was hence one of the early goals within my doctorate, and they proved to be an important foundation that we would employ in many of our follow-up studies. A chapter within this thesis is hence dedicated to describing the algorithm we used and the optimization of the code done in order to maximize performance on systems comparable to personal computers. In the course of this chapter, we will also investigate the different methods to extract the characteristic length — a thermodynamical quantity used to characterize large scale network dynamics — and

study their properties and physical interpretation. This lead us to identify an implicit dependence of the different length-scale measurements on the root mean squared velocity of the domain network, which allowed us to introduce a novel and computationally cheap method to measure this quantity.

We will then venture into exploring the Parameter-Free Model, which can be used to estimate this root mean squared velocity and the characteristic length of domain wall networks. We will derive analytical approximations that allow us to calculate the values of those two quantities in two limits: a static, Minkowski-like background as well as a rapid, but still decelerated power-law expansion of the background. This allows us to introduce a simple fitting function, which can interpolate between these limiting cases and therefore predict the characteristic length and the root mean squared velocity for a broad range of expansion rates, including the cosmologically most relevant regimes of matter and radiation domination. At this point, we will delve further into a comparison between the Velocity-Dependent One-scale Model and the Parameter-Free Model in the regime of rapidly expanding backgrounds and show that indeed both models are consistent in this limit. As it was pointed out in the literature, in the regime of slower expansion rates, however, significant discrepancies between predictions of the Parameter-Free Model and simulations become apparent. Here, we investigate these discrepancies by performing field theory simulations of collapsing cylindrical and spherical domain walls, whose behavior is the foundation of the modeling of network dynamics in the Parameter-Free Model.

To get a complete picture, we will study non-standard domain wall models as well. In chapter 5 we introduce a toy model that allows domain walls to interact with compact matter distributions. We investigate how the coupling parameters may affect the outcome of collisions between walls and those objects, develop a simple analytical model to predict if a wall will transit the object, or on the other hand get reflected, and eventually test those predictions with simulations. We will also study another effect related to domain wall dynamics, namely the possibility of a late time cosmological phase transition induced by collapsing false vacuum domains in a modified ϕ^6 potential.

A cornerstone of this thesis is the study of the gravitational wave emission of walls, which we dedicated ourselves to in chapter 6. We develop a new semi-analytical framework to compute the Stochastic Gravitational Wave Background emitted by frictionless domain wall networks which complements the existing studies in the literature that are largely based on estimations stemming from numerical simulations. We also obtain analytical

expressions that can describe this emission in the matter- and radiation-era to a very good approximation and calculate the potential signatures of a network decaying due to the effect of bias. We then compare our results with current observational constraints from the Cosmic Microwave Background and Pulsar Timing Arrays, discussing the implications for domain walls as a potential source of the recently detected Stochastic Gravitational Wave Background.

Keywords: physics, astronomy, cosmology, cosmic defects

Declaration

The work in this thesis, except where reference is made to the work of others, is my own and to the best of my knowledge original. This work was carried out together with Lara Sousa and Pedro Avelino. Moreover, the work presented in section 5.2 was performed in collaboration with Fabiano de Carvalho Simas, who carried out simulations of kink-kink collisions, Caroline Silva and Adalto Gomes, who gave valuable theoretical input, as well as Sergei Mukovnikov and Clara Winckler who contributed to the discussions on the topic. Parts of this thesis appeared in various papers [2–4], however, the complete set of results has never been submitted for any other degree, diploma or qualification.

Units and Notation

Throughout this thesis, we will use natural units in which the values of the speed of light, the reduced Planck's constant, and the Boltzmann constant are set to unity: $c = \hbar = k_B = 1$. Furthermore, we will use a (+,-,-,-) metric signature and unless otherwise specified, a dot over a variable represents differentiation with respect to physical time t: $\dot{x} = dx/dt$.

Acronyms and Abbreviations

ALP Axion-Like Particle

BAO Baryon Acoustic Oscillations

CERN European Organization for Nuclear Research

CMB Cosmic Microwave Background

CPTA Chinese Pulsar Timing Array

DESI Dark Energy Spectroscopic Instrument

DW Domain Wall

EOM Equation Of Motion

EOS Equation of State

EPTA European Pulsar Timing Array

ESA European Space Agency

ET Einstein Telescope

FCT Fundação para a Ciência e a Tecnologia

FLRW Friedmann-Lemaître-Robertson-Walker

FT Field Theory

GR General Relativity

GUT Grand Unified Theory

GW Gravitational Wave

ΛCDM Lambda Cold Dark Matter - Cosmological Standard Model

LHC Large Hadron Collider

LHS/RHS Left/Right Hand Side

LISA Laser Interferometer Space Antenna

NG Nambu-Goto

PDF Probability Density Function

PFM Parameter-Free Velocity-dependent One-Scale model

PPTA Parkes Pulsar Timing Array

PTA Pulsar Timing Array

RMS Root Mean Square

SDSS Sloan Digital Sky Survey

SGWB Stochastic Gravitational Wave Background

SKA Square Kilometre Array

VEV Vacuum Expectation Value

VOS Velocity-dependent One-Scale

WRT With Respect To

List of Symbols

Fundamental Constants

G Newton's Gravitational Constant

c Speed of Light

$\hbar$ Reduced Planck's Constant

k_B Boltzmann Constant

Spacetime and Coordinates

t Cosmic Time

η Conformal Time

$g_{\mu\nu}$ Metric Tensor

$\eta_{\mu\nu}$ Minkowski Metric

$G_{\mu\nu}$ Einstein Tensor

$T_{\mu\nu}$ Energy-Momentum Tensor

$R_{\mu\nu}$ Ricci Tensor

γ Lorentz Factor

Cosmological Parameters

$a(t)$ Scale Factor

λ Power-Law Expansion Exponent

$\mathcal{C}_{\mathrm{r}}$, $\mathcal{C}_{\mathrm{m}}$ Power-Law Expansion Proportionality Constants

a_{eq} Scale Factor at Matter-Radiation Equality

z Redshift

H Hubble Parameter

$\mathcal{H}$ Conformal Hubble Parameter

h Dimensionless Hubble Parameter

k Spatial Curvature Parameter

Λ Cosmological Constant

Λ_{inf} Inflationary Vacuum Energy

d_{eh} Comoving Event Horizon

ϵ_H Hubble Slow-Roll Parameter

Density Parameters

ρ Energy Density

$\bar{\rho}$, $\langle\rho\rangle$ Mean Energy Density

p Pressure

w Equation of State Parameter

$\rho_{\mathrm{crit}}(t)$ Critical Density at Time t

ρ_{c} Today's Critical Density

Ω_i Today's Density Parameter for component i=r, m, Λ, k

Field Theory and Potentials

$\mathcal{L}$ Lagrangian Density

S Action

ϕ, Φ, θ Scalar Fields

$V(\phi)$ Scalar Field Potential

m Field's Mass

V_0 Potential Energy Scale Parameter

η Symmetry Breaking Scale

λ Self-Coupling Constant

ϕ_0 Vacuum Expectation Value of ϕ

T Temperature

Domain Wall Physics

σ_0 Wall Rest Mass per Unit Area

w_0 Wall Thickness at Rest

ϵ Parameter Specifying Boundaries of Walls in Simulations

κ_0 Rest Wall Width According to ϵ-criterion

V_{box} Simulation Box Volume

N_{DW} Domain Wall Number

q, q_i, q_* Comoving/Initial/Rescaled Domain Wall Radius

R Invariant Radius

τ, τ_* Conformal/Rescaled Domain Wall Collapse Time

Topological Quantities

$\mathcal{M}$ Vacuum Manifold

G Symmetry Group

H Unbroken Subgroup of G

π_n nth-Homotopy Group

$\mathbb{1}$ Identity Element

Network Evolution Parameters

L Physical Characteristic Length

$\bar{v}, \sigma_v$ Root Mean Squared Velocity

ξ Scaling Length Parameter

ζ Comoving Scaling Length Parameter

$L^{(\mathrm{count})}$ Comoving Char. Length (counting method)

$L^{(\mathrm{PRS})}$ Comoving Char. Length (PRS method)

$L^{(\rho)}$ Comoving Char. Length (energy density method)

k_w Curvature Parameter (VOS Model)

$\tilde{c}$ Chopping Parameter (VOS Model)

l_{d} Damping Length Scale

l_{f} Friction Length Scale

β Initial Number Density (PFM)

$\mathcal{P}(q)$ Probability Distribution for Initial Radii

s Geometry Parameter for Spherical/Cylindrial Domains

Model Specific Parameters

ϱ_0 Compact Object Density

r_0 Object Radius

r_e Effective Object Radius

Θ Coupling Constant for Domain Wall Matter Interaction

ε Parameter Quantifying Non-Elasticity of Collisions

w_1, σ_1 Width and Rest Mass per Unit Area of Wall Inside a Compact Object

I_e, $I_{e,c}$ (Critical) Effective Coupling Strength

$\mathcal{V}(r)$, $\mathcal{A}(r)$ Domain Volume and Surface Area

V_0, A, $\triangle$ Parameters of Biased ϕ^6 Potential

σ_{ff}, σ_{tf} Rest Mass per Unit Area of Walls Between False/False And True/False Vacua

ΔV_1, ΔV_2 Height of Potential Barrier and Depth of True Vacuum in Biased ϕ^6 Potential

$q_{\min}$ Minimal Domain Radius for Inducing a Cosmological Phase Transition

$\sigma_{\mathrm{Z}} = (10^6\,\mathrm{eV})^3$ Zel'Dovich Bound

$\mathcal{F}$ Fraction of Energy Lost by Network Going Into GWs

$\mathcal{A}_\lambda$ $(= \tilde{c}\bar{v}_\lambda/\xi_\lambda^2)$ Scaling Constant

$p(f)$ PDF for Spectral Distribution of GWs

ν Power-Law Index of $p(f)$

α Parameter Quantifying Ratio of Char. Scale of GW Emission and Char. Length

f_{p} Peak Frequency

Ω_{gw}, $\Omega_{\mathrm{gw}}(f)$ Fractional Energy Density Contribution and Full Spectrum of GWs Today

Table of Contents

1. Introduction 1
   1.1. ΛCDM: The Cosmological Standard Model 3
      1.1.1. Cosmic Distances and the Geometry of Spacetime 3
      1.1.2. The Friedmann Equations 4
      1.1.3. State of Observations 7
   1.2. Scalar Fields in Cosmology 8
   1.3. Cosmic Inflation 9
      1.3.1. The Shortcomings of ΛCDM 10
      1.3.2. A Theory to Solve Them All 11
      1.3.3. Slow-Roll Inflation and the Reheating Epoch 13
      1.3.4. Implications of Inflation for Structure Formation 15
   1.4. Cosmic Topological Defects 16
      1.4.1. Defect formation: The Kibble Mechanism 16
      1.4.2. Classification of Topological Defects 19
2. Domain Walls in Cosmology:
   A Brief Overview of the State-of-the-Art 21
   2.1. Domain Walls in the Goldstone Model 22
   2.2. Modeling Domain Wall Network Evolution I:
      The Velocity-Dependent One-Scale Model 25
   2.3. Modeling Domain Wall Network Evolution II:
      The Parameter-Free Velocity-Dependent One-Scale Model 28
   2.4. Biased Domain Walls and Their Decay Mechanisms 31
3. Simulating Domain Walls 33
   3.1. The PRS Equation 34
   3.2. Implementing the PRS Algorithm in Python 35
      3.2.1. Performance Optimizations 35
      3.2.2. Selecting Numerical Parameters 38
   3.3. Measuring the Characteristic Length from Simulations 41
      3.3.1. Influence of Spatial Discretization 43
      3.3.2. Dependence of Measured Lengths on Wall Velocities 49
      3.3.3. Velocity From Lengths 53
4. Exploring the Parameter-Free Model 55
   4.1. An Analytical Approximation to the Parameter-Free Model 55
      4.1.1. The $\lambda \to 1^-$ Case 55
      4.1.2. The $\lambda = 0$ Case 59

4.1.3. Fitting the Scaling Predictions of the Parameter-Free VOS Model 60
4.2. Comparison to the VOS Model 63
4.3. Testing the Parameter-Free Model With Collapsing Domains 67
4.3.1. Simulating Collapsing Spherical and Cylindrical Domains 67
4.3.2. Numerical Tests of the PFM 70
5. Non-Standard Domain Wall Scenarios 77
5.1. Domain Wall Interactions with Compact Objects 77
5.1.1. Estimating the Critical Coupling Strength 79
5.1.2. Collision-Induced Small-Scale Structure 83
5.2. Late Time Phase Transitions Triggered By Collapsing Domain Walls 86
6. Gravitational Waves from Domain Wall Networks 93
6.1. A New Framework to Calculate the SGWB by Domain Walls 94
6.1.1. Basic Assumptions on the Emission of Gravitational Waves 95
6.1.2. Energy Density in Gravitational waves 97
6.1.3. Spectrum of the Stochastic Gravitational Wave Background 101
6.1.4. Full Numerical Computation in a ΛCDM Background 101
6.1.5. Analytical Approximation to the Domain Wall SGWB 103
6.1.6. Shape of the Full Spectrum 107
6.1.7. The Contribution of Bias 109
6.1.8. Comparison With Previous Computations 111
6.2. Observational Constraints from the CMB and PTAs 117
6.2.1. Cosmic Microwave Background Constraints 118
6.2.2. Domain Wall Interpretation of PTA Data 121
7. Summary and Outlook 125

References 133

1. Introduction

Modern cosmology aims to study the origin, the evolution as well as the structure and composition of our universe. Today, the paradigm of the universe starting out with a hot big bang and its subsequent expansion is one of its cornerstones, and the late-time acceleration of this expansion is largely uncontroversial. Yet, the exact value of the present rate of expansion is subject to debates in the field, infamously often referred to as the *crisis in cosmology* [5]. Although it remains uncertain whether this crisis reflects a genuine discrepancy or arises from systematic errors in our observations or their analysis (as some recent work suggests [6]), theorists have already armed themselves with tools that can pave a way out of this crisis, often invoking a modified expansion history of our universe with respect to that of the standard cosmological model [7, 8].

Regardless of whether current surveys such as The Dark Energy Spectroscopic Instrument (DESI) [9] and the Euclid mission [10] of the European Space Agency (ESA) will corroborate or falsify some of these models, it has become clear that scalar fields can play a pivotal role in explaining some key properties of the universe. Quintessence or the related k-essence models can provide a natural explanation for a time-dependent dark energy component [11–13], and axionic fields may describe some key features of dark matter very well [14, 15]. Scalar fields may have been involved in phase transitions taking place in the early universe and, if coupled to other fundamental fields, they might cause variations of fundamental constants in space and time [16–18]. Moreover, they are predicted to be the key drivers of inflation, the phase of rapid exponential expansion that is believed to have taken place in the very early stages of the universe [19]. With the discovery of the Higgs boson in 2012 at the Large Hadron Collider (LHC) of the European Organization for Nuclear Research (CERN) [20, 21], scalar fields took the step from a purely theoretical construct towards a real physical entity. It was much earlier, however, that physicists began to realize that, through a process of spontaneous symmetry breaking, topologically stable field configurations known as cosmic defects may have formed in phase transitions, carrying enormous amounts of energy within their cores [22]. Well-known representatives of their kind are the point-like magnetic monopoles [23] that, despite extensive searches, have still evaded detection — a fact that decisively triggered the development of inflationary theory — and the line-like cosmic strings, which were long

thought to seed structure formation, although they have now been shown to be playing at most a subdominant role in the latter [24–28].

The present thesis is devoted to the study of cosmic Domain Walls (DWs), sheet-like defects that separate regions in which a scalar field takes on different vacuum expectation values. Their formation is predicted by a broad range of particle physics models and, if they exist, they could interact with their environment in various ways. Domain walls that are coupled to electromagnetism could, for instance, induce spatial variations of the fine structure constant and, upon passage, alter the flow of time as measured by our atomic clocks [29]. In the case of a non-minimal gravitational coupling to matter, domain walls — although significant interference with the standard evolution of large scale structure is ruled out — have been proposed, for example, as a possible explanation for the *satellite problem* in galactic physics [30]. Earlier expectations of domain wall networks significantly contributing to dark energy have been frustrated [31]. Domain walls, regardless of whether they are still present in the universe or have decayed away in the past, could also have sourced a Stochastic Gravitational Wave Background (SGWB) [32, 33].

Gravitational Waves (GWs) have enabled us, during the last decade, to observe astrophysical processes through a window that supplements the standard channels that optical astronomy and astroparticle physics provide. Recently, several collaborations working with Pulsar Timing Arrays (PTAs) have presented compelling evidence for a SGWB in the nano-hertz regime [34–37] and future planned gravitational wave observatories such as the Laser Interferometer Space Antenna (LISA) and the Einstein Telescope (ET) will help us probe yet another frequency window in the upcoming decades [38, 39]. Eventually, this development could enable us to detect GWs from non-astrophysical sources and allow us to trace back their origin to specific cosmological processes. For this to become a reality, it is vital, however, to dispose of a precise characterization of the spectra that different cosmological sources would produce. In the case of cosmic domain walls, a detailed understanding of the produced spectra can only be reached if their dynamics in different stages of cosmic evolution are well understood.

This thesis aims to contribute to a better understanding of the gravitational radiation produced by domain wall networks twofold: first, by developing new numerical and analytical studies of domain wall dynamics in the universe, analyzing both the behavior of walls as isolated entities, and studying potential interactions with astrophysical objects; second, by complementing the existing simulation-based predictions of gravitational wave production

with a new semi-analytical model. We will show that this model is able to make predictions of the expected spectra over a wide range of parameter space and can then, in the case of a detection of GWs from domain walls, enable us to probe particle physics models with gravitational waves. In the following sections, we will discuss the state-of-the-art of modern cosmology, starting with the standard model of the hot big bang and inflation.

1.1. ΛCDM: The Cosmological Standard Model

Arguably, the most fundamental aspect of our modern paradigm of the universe is formulated in the *cosmological principle*. This principle states that on sufficiently large scales the universe is statistically homogeneous and isotropic. Homogeneity here refers to the universe obeying a translational symmetry, so that there is no preferential location in space, while being isotropic means that its properties do not depend on the direction of observation. This principle is often used to characterize the distribution of matter in the universe, but it also implies that the laws of physics are the same everywhere in our cosmos. Indeed, there is overwhelming observational evidence, most prominently from the Cosmic Microwave Background (CMB) and large-scale galaxy surveys such as the Sloan Digital Sky Survey (SDSS) [40] that, regarding the distribution of matter, the cosmological principle holds true on scales surpassing some hundreds of megaparsecs (while on smaller scales the clustering of matter induces large inhomogeneities)* [43].

1.1.1 Cosmic Distances and the Geometry of Spacetime

The properties of homogeneity and isotropy necessarily require space to have a constant or vanishing curvature (in other words, curvature cannot be a function of the spatial coordinates). Moreover, a realistic mathematical description of our universe should be locally invariant under Lorentz transformations. Combining these properties, the metric named after the scientists Friedmann, Lemaître, Robertson, and Walker (FLRW) is one of the most essential tools for cosmologists [19]. Its line element is given by

$$ds^2 = dt^2 - a(t)^2 d\Sigma^2 \,. \tag{1.1}$$

In this equation, a, which is a function of physical time t, is the so-called scale factor that can model an expansion or contraction of space, and $d\Sigma^2$ is the spatial part of the metric,

*Observational efforts have also been made to probe whether the laws of physics and, in particular, the fundamental couplings of nature are the same everywhere in our observable universe. Current observational evidence is consistent with no variation of these couplings in space or time [17, 41, 42].

which can be written as

$$d\Sigma^2 = \frac{dr^2}{1-kr^2} + r^2 d\Omega^2 \,. \tag{1.2}$$

Here k is the spatial curvature, and $d\Omega^2$ is the metric on the unit 2-sphere (i.e., the solid angle element). In particular, for $k = 0$ and a constant a, (1.1) reduces to the Minkowski spacetime [44]. For practical reasons, in calculations physicists often use the so-called comoving distance d_c, which in flat universes coincides with the coordinate distance r, but needs to be more carefully defined if the universe is positively or negatively curved. The comoving distance is fixed for a pair of distant galaxies (neglecting their peculiar motion), contrary to the proper or physical distance d_p which increases as the universe expands:

$$d_p(t) = a(t) d_c \,. \tag{1.3}$$

Similarly, one can define a conformal time coordinate η, given by

$$\eta(t) = \int_0^t \frac{dt'}{a(t')} \,. \tag{1.4}$$

The conformal time not only is useful in calculations but has also an important physical interpretation: it represents the comoving distance light can travel from the beginning of the universe until a time t. Since no massless and certainly no massive particles can travel faster than the speed of light, this constitutes an upper limit on the distance information can travel, known as the particle horizon.

1.1.2 The Friedmann Equations

Gravity, compared to the known forces of the Standard Model of Particle Physics, is by far the weakest interaction. On cosmological scales, however, it essentially governs the dynamics of the universe*. The simplest framework that describes gravity in the most fundamental way is Einstein's theory of general relativity. The field equations

$$G_{\mu\nu} = 8\pi G T_{\mu\nu} + \Lambda g_{\mu\nu} \tag{1.5}$$

relate the geometry of spacetime to its energy-momentum content [45]. On the left hand side (LHS) of (1.5) stands the Einstein tensor. It is defined via the Ricci tensor $R_{\mu\nu}$ and the scalar curvature R as $G_{\mu\nu} = R_{\mu\nu} - (1/2) g_{\mu\nu} R$, $g_{\mu\nu}$ being the spacetime metric. The Einstein tensor hence represents a geometrical quantity. On the right hand side (RHS) of Eqn. (1.5), $T_{\mu\nu}$ is the energy-momentum tensor and G is Newton's gravitational constant.

*This at least holds true when the universe has cooled down and expanded sufficiently. Note however that in the very early stages, including the Planck epoch, the statement loses its validity.

Einstein also introduced the cosmological constant Λ, which was originally fine-tuned in a way that the field equations describe a static universe [46]. Afterward, it was discovered by Edwin Hubble that the universe, in fact, is not static as depicted by Einstein, but expanding [47], leading to Einstein overthrowing his idea of a cosmological constant and naming it his "biggest blunder". Decades later, the cosmological constant would have its renaissance. When Riess, Schmidt, Perlmutter et al. studied the recession velocities of distant Type Ia supernovae, they found that the expansion of the universe is undergoing a late-time acceleration [48–51]. This late-time acceleration can be explained by a cosmological fluid with a suitable energy density and a negative pressure, which was given the placeholder name *dark energy*, until its nature can be understood. In the simplest models, the density of dark energy is constant, in which case it can be modeled by the Λ-term in Eqn. (1.5).

Although being mathematically complex, the physical interpretation of the Einstein field equations may be summarized by the famous phrase coined by John Wheeler: matter tells spacetime how to curve, and spacetime tells matter how to move. The general mathematical complexity of finding solutions to the field equations can be reduced if one considers some special configurations that exhibit an enhanced symmetry. Historically, a first solution was found by Karl Schwarzschild, who calculated the gravitational field of a spherical central mass [52], a metric that gave rise to modern black hole physics and was later generalized by Kerr, Newman and others for spinning and charged central masses [53, 54]. Likewise, the FLRW spacetime stands as another prominent example of a highly symmetric configuration. Applying the framework of general relativity to it, one can find a simple equation that describes the temporal evolution of the scale factor as a function of the curvature of spacetime and its energy content:

$$H^2 \equiv \left(\frac{\dot{a}}{a}\right)^2 = \frac{8\pi G}{3}\rho - \frac{k}{a^2}\,. \tag{1.6}$$

In this so-called Friedmann equation, H is the Hubble parameter, which quantifies the expansion rate at each time and ρ is the energy density*. Here we absorbed the energy density associated with the cosmological constant, $\rho_\Lambda = \Lambda/(8\pi G)$, into ρ. Equation (1.6) shows that there exists a critical density

$$\rho_{\text{crit}} = \frac{3H^2}{8\pi G}\,, \tag{1.7}$$

*The Friedmann equation can alternatively be derived from Newtonian principles only [43].

for which the spatial curvature vanishes, producing a flat universe. If the energy content of the universe exceeds this density, the overall geometry of the universe is spherical, and the universe is finite. On the other hand, for a lower energy content, the geometry of spacetime is hyperbolic and the universe is open.

The proper energy density ρ can be written as a sum of the energy densities of the cosmic fluids that contribute to it. In general relativity, these are typically described as *perfect fluids* defined by a vanishing viscosity and heat conductivity, so that their stress-energy tensor reduces to

$$T^{\mu\nu} = (\rho + p)u^\mu u^\nu + pg^{\mu\nu}\,, \tag{1.8}$$

u^μ being the 4-velocity of the fluid. These fluids are fully characterized by their Equation Of State (EOS),

$$p = w\rho\,, \tag{1.9}$$

where p is the proper pressure and their effects on cosmic expansion are solely determined by the EOS parameter w. The most obvious contributor to the energy content of our universe is its matter. This includes the visible (baryonic) matter that we can observe with our telescopes, but more importantly a significant contribution of dark matter, which interacts neither with itself nor with baryonic matter other than via gravity (or possibly also through weak interactions). Both types of matter are non-relativistic, essentially pressureless and hence characterized by an EOS parameter close to $w = 0$. Moreover, as the amount of matter in the universe should (in good approximation) be conserved in a comoving volume its energy density must behave as $\rho \propto a^{-3}$. In contrast to that, other ingredients of our universe that are in relativistic motion exert a positive pressure and are characterized by $w = 1/3$. At the present cosmic time this mainly includes photons, but in the past other relativistic species such as light neutrinos constituted a significant contribution. In addition to a dilution or densification in an expanding/contracting space, these species experience a red/blue shift of their wavelength with cosmic expansion/contraction, so that overall their energy density scales as $\rho \propto a^{-4}$. Unlike these components that behave akin to our daily physical experience, the energy density associated with the cosmological constant Λ is different in that it is literally constant in a given physical volume*. It is therefore not a function of the scale factor and the associated pressure is negative with an EOS parameter $w = -1$.

*One seemingly obvious physical source for such a cosmological constant was thought to be found in the quantum fluctuations in vacuum, however, quantum electrodynamical calculations showed a mismatch between the theoretical predictions and the observed value of around 120 orders of magnitude — the infamous *cosmological constant problem* [55].

It is useful to define the fraction of energy density each of the cosmological fluids contributes to the critical density of the universe. This fraction is usually labeled as Ω. Typically, cosmological quantities as measured at the present time are endowed with a subscript "0", such that, for instance, today's value of the Hubble parameter, also known as the Hubble constant, is labeled as H_0. In order to keep notational simplicity, we will omit this subscript when labeling the energy density and the density fractions. Let us define $\rho_\mathrm{c} \equiv \rho_{\mathrm{crit},0} = 3H_0^2/8\pi G$. Furthermore, let us denote with $\Omega_\mathrm{i} \equiv \Omega_{\mathrm{i},0} = \rho_{\mathrm{i},0}/\rho_\mathrm{c}$ for i=r, m, Λ respectively, today's fractional densities associated with radiation, matter, the cosmological constant, and define today's curvature parameter as $\Omega_k \equiv -k/H_0^2$. We may now rewrite the Friedmann equation (1.6) explicitly as a function of the scale factor:

$$H^2 = H_0^2 \left(\Omega_\mathrm{r} a^{-4} + \Omega_\mathrm{m} a^{-3} + \Omega_\mathrm{k} a^{-2} + \Omega_\Lambda \right) . \tag{1.10}$$

Due to the distinct scalings with a, different components in this equation will dominate at different times. In a strictly expanding universe, in particular, there will be an early phase of radiation domination that transitions to a matter dominated universe when the scale factor reaches a value of $a_\mathrm{eq} = \Omega_\mathrm{r}/\Omega_\mathrm{m}$. Deep within the radiation- and matter-dominated eras, Eqn. (1.10) possesses simple solutions in which the scale factor is a power-law function of time, $a(t) \propto t^\lambda$.

1.1.3 State of Observations

The values of the cosmological parameters used in Eqn. (1.10) can be inferred from various astronomical observations. To begin with, a number of modern cosmological surveys agree that the curvature of the universe is very close to — and compatible with — zero [56]. As a consequence, the second to last term in Eqn. (1.10) is usually dropped. The exact value of the Hubble constant has been causing cosmologists some headaches over the last couple of years [57, 58]. Direct measurements of its value in the local (and therefore late-time) universe using supernova observations [59, 60] seem to show a deviation from the (model-dependent) predictions made with CMB data [56]. Although their relative deviation is less than 10 %, this so-called *Hubble tension* might indicate problems with the distance measurements in our universe or hint at deviations from the standard cosmological model itself [61]. Yet, recently the possibility that the cause of the Hubble tension might be hidden deep within data analysis routines moved into focus again, in which case there might be no tension after all [6]. Apart from that, the values of the remaining cosmological parameters appearing in the Friedmann equation are less controversial. They tell

us that the energy budget of today's universe is about 69 % dominated by dark energy, the hypothetical substance that acts approximately as a cosmological constant and causes the observed late-time acceleration of the cosmic expansion [48, 49]. Almost all the rest of the energy density is made up of non-relativistic matter, which is itself dominated by Cold Dark Matter (CDM). With a contribution of around 5 % and 0.01 % respectively, the baryon and radiation densities play only a subdominant role in the present-day evolution of our universe. This gives rise to the name of the ΛCDM model. Throughout the remainder of this thesis, we will use the cosmological parameters that were obtained by the Planck Collaboration by combining their 2018 data release with weak lensing and Baryon Acoustic Oscillations (BAO) data [56]. These are given by $\Omega_{\mathrm{r}} = 9.1476 \cdot 10^{-5}$, $\Omega_{\mathrm{m}} = 0.308$, $\Omega_{\Lambda} = 1 - \Omega_{\mathrm{m}} - \Omega_{\mathrm{r}}$ and the Hubble parameter is $H_0 = 2.13 \cdot h \cdot 10^{-33}\,\mathrm{eV}$, with $h = 0.678$. It should be mentioned that despite ΛCDM, which is regarded as the cosmological standard model by the principle of Occam's razor, there exists a plethora of alternative cosmological models. These include models in which there is an early phase of matter domination [62], models in which dark energy evolves with time [63], models in which the equations of gravity themselves are modified [64], and many more [65]. A common feature of these models is that they usually come with a number of additional free parameters that then allow for a better fit of a chosen set of observational measurements. In this work those shall not be discussed in greater detail.

1.2. Scalar Fields in Cosmology

Above, we highlighted that scalar fields have become indispensable in modern cosmology. Theories invoking scalars can reach arbitrary levels of complexity. For example, in the widely studied scalar-tensor theories, a scalar field with a non-minimal gravitational coupling can lead to modifications of the field equations of gravity. Thereby, despite allowing deeper insights into gravity itself, some of these theories aim to provide a natural explanation for the observed accelerated expansion of the universe or to explain dynamics that would otherwise require the presence of dark matter. Nevertheless, even the simplest case of a minimally coupled scalar field in a homogeneous background can give rise to a variety of phenomena. In the following, we will briefly summarize the important equations governing the dynamics of a single, free (i.e. minimally interacting) scalar field in a FLRW universe. It should be mentioned that this treatment is purely classical since, in general, potential quantum effects may largely be neglected on cosmological scales. The fundamentals discussed in this chapter will lay the foundation to explain concepts such as slow-roll inflation and the formation of topological defects in the early universe.

Scalar fields associate a (typically real or complex) number with each point in space and time. They are commonly denoted as $\phi(x,t)$ and may give rise to a potential energy density $V(\phi)$, typically including a mass term and possibly self-interaction terms. The Lagrangian density of the field is then, as usual, given as the kinetic term minus this potential energy:

$$\mathcal{L} = \frac{1}{2}\partial_\mu\bar{\phi}\partial^\mu\phi - V(\phi)\,. \tag{1.11}$$

Variation of the action

$$S = \int d^4x\sqrt{-g}\mathcal{L} \tag{1.12}$$

With Respect To (WRT) ϕ yields the equation of motion

$$\frac{1}{\sqrt{-g}}\partial_\mu(\sqrt{-g}\partial^\mu\phi) = -\frac{dV}{d\phi}\,, \tag{1.13}$$

which in a FLRW background are of the form

$$\ddot{\phi} + 3H\dot{\phi} - \nabla^2\phi = -\frac{dV}{d\phi}\,. \tag{1.14}$$

Here, the spatial gradients are taken WRT physical coordinates and the term proportional to $\dot{\phi}$ is a damping term that suppresses the motion of the field in an expanding background and vanishes in Minkowski space.

Varying the action (1.12) WRT the metric allows us to find the energy-momentum tensor:

$$T^{\mu\nu} = \frac{-2}{\sqrt{-g}}\frac{\delta S}{\delta g_{\mu\nu}}\,. \tag{1.15}$$

Therefore, we can compute the energy density and pressure associated with the field, respectively, as

$$\rho = T_{00} = \frac{\dot{\phi}^2}{2} + \frac{(\nabla\phi)^2}{2} + V(\phi)\,, \tag{1.16}$$

and

$$p = \frac{1}{3}\sum_{i=1}^{3} T_{ii} = \frac{\dot{\phi}^2}{2} - \frac{(\nabla\phi)^2}{6} - V(\phi)\,. \tag{1.17}$$

The equations derived in this section will play an important role throughout the remainder of this work. However, before picking up on the topic of scalar fields again to discuss how they are associated to topologically stable defects, we will review another cornerstone of modern cosmology: cosmic inflation.

1.3. Cosmic Inflation

Given the right initial conditions, the ΛCDM paradigm described in section 1.1 is consistent with cosmological observations over the lifetime of the universe, with great precision.

Nevertheless, in order to explain the properties of the universe we observe today, these initial conditions require a significant amount of fine-tuning. Theorists therefore started to search for possible mechanisms that would explain these initial conditions beyond the anthropic principle (the notion that we observe the universe as it is because only those conditions that allow for our existence are observable to us).

1.3.1 The Shortcomings of ΛCDM

One of the mysteries of the ΛCDM universe is its lack of intrinsic curvature. The energy density associated with the curvature component in the Friedmann equation (cf. (1.10)) is proportional to a^{-2}. Together with the observational evidence showing that curvature can at most play a very subdominant role at the present time [56], this tells us that the universe must have started from an almost perfectly flat state [66]. More quantitatively speaking, this scaling implies that for a deviation from unity at the present day that is smaller than 1 %, $|\Omega_k - 1| < 0.01$, and a largely radiation-dominated evolution, Ω's deviation from unity following the *Planck epoch* would have to be of order 10^{-62}. This is the so-called *flatness problem* [67].

In another matter, as we will see in section 1.4, the process of spontaneous symmetry breaking can lead to the formation of various topological defects in the early universe. One generic prediction in, e.g. *Grand Unified Theories* (GUTs) [68, 69] — which conjecture a unification of the forces of the Standard Model of Particle Physics at high temperatures — as well as in superstring theories [70] and others, is the copious formation of magnetic monopoles. These are particles that carry a quantized magnetic charge and are generally predicted to be very massive [23]. Moreover, once formed, they would largely survive throughout cosmic history [71]. In theory, these properties make them potentially detectable. Despite intensive searches in particle colliders and various astronomical experiments, none of these particles have yet been discovered [72, 73]. Their lack is known as the *magnetic monopole problem*.

Yet another problem is to explain the uniformity of the CMB solely within the framework of standard cosmology. After subtracting the dipole signal from the CMB, which is thought to be caused by the movement of our galaxy WRT the cosmic rest frame, it is isotropic up to a factor of about 10^{-5}. This uniformity can only be explained if all regions in our observable universe have once been in causal contact. In a decelerating universe, this cannot be the case. The Hubble horizon, or Hubble radius, defined as H^{-1}, measures

the maximum distance of points receding subluminally in an expanding spacetime. In the cosmological standard model, it is of the same order as the particle horizon. Importantly, H^{-1}/a is a growing function of time throughout the radiation- and matter-dominated eras, meaning that new regions of space continuously enter the horizon that — according to this standard model — shouldn't have been in causal contact before. This is known as the *horizon problem* [74].

1.3.2 A Theory to Solve Them All

Historically proposed to dilute monopoles into the realm of non-detectability, the framework of cosmic inflation not only solves the aforementioned problems at once, but it also provides an elegant explanation for the nearly scale-invariant spectrum of density fluctuations observed in the universe [75]. In standard cosmological terminology, an inflationary period is defined by an accelerated expansion of the scale factor, i.e., $\ddot{a} > 0$. According to many models of cosmic inflation, there was an era of quasi-exponential expansion in the very early universe, driven by a nearly constant vacuum energy, akin to what we observe as a cosmological constant in today's universe. This era may have started at around $t \approx 10^{-35}$ s after the big bang and lasted until at most $t \approx 10^{-30}$ s. In the following, we will discuss how this accelerated expansion can help us to solve the problems of the ΛCDM model.

Inflation and the Horizon Problem Akin to the definition of the *particle horizon* (cf. Eqn. (1.4)), one can define a comoving *event horizon*

$$d_{\mathrm{eh}} = \int_t^\infty \frac{dt'}{a(t')} \,. \tag{1.18}$$

This expression indicates the maximum comoving distance that events at time t can ever influence in the future. Conversely, it also represents the farthest distance from which signals can still reach a comoving observer at time t [76]. Pictorially, for $t = 0$, the cosmological event horizon can be interpreted as the maximum extension of the particle horizon.

It can be shown that, in a radiation- or matter-dominated universe — or more generally in any decelerating expansion scenario — the event horizon diverges. In other words, $\lim_{t\to\infty} d_{\mathrm{eh}} = \infty$, implying that no finite event horizon forms under decelerated expansion [77]. The situation is different for an inflationary universe. If we assume inflation is driven by a vacuum energy density $\rho_{\mathrm{vac}} = \Lambda_{\mathrm{inf}}/(8\pi G)$, with Λ_{inf} playing the role of an effective cosmological constant and dominating the energy budget for some time, then the Friedmann

equation (1.6) is solved by an exponentially growing scale factor

$$a(t) = a_i e^{Ht}\,, \tag{1.19}$$

where the Hubble parameter takes a constant value $H = \sqrt{\Lambda_{\rm inf}/3}$ [67]. Inserting this expression into Eqn. (1.18), one finds that in an inflating universe the proper Hubble radius is constant and of the same order as the proper event horizon [78]. The comoving Hubble horizon, on the other hand, shrinks with time. This means that regions in the universe that were once close enough to each other to exchange signals (i.e., regions that have been in causal contact) could have been pushed out of the Hubble horizon by the rapidly expanding space during inflation. After inflation would have come to an end and the expansion of the universe slowed down, more and more of these regions would then successively re-enter the comoving Hubble horizon. Under the standard Big Bang evolution since very early times (starting shortly after inflation, if it occurred), the particle horizon would be about 47 Glyr today. However, the total size of the universe — including regions causally disconnected by inflation — could be vastly larger. Yet, measurements of the CMB show that even in regions with the largest possible separation that we can observe, the background radiation temperature is uniform with a maximum relative deviation of the order 10^{-5} [79]. Assuming that regions entering the horizon at the present time must once have been in causal contact with each other (or in general relativistic terminology: their past light cones must have overlapped) enables us to establish a lower limit on the factor by which the universe must have grown during inflation of around 60 e-folds or a growth factor of around 10^{26} [80]. This enormous growth of the physical volume of the universe, while maintaining a roughly constant Hubble horizon distance, simultaneously solves the monopole problem [71, 81]. If magnetic monopoles were produced before (or even during) cosmic inflation in any reasonable quantity, inflation would dilute their density to less than one per Hubble volume, making them virtually impossible to detect.

Inflation and the Flatness Problem As we have seen, the curvature term in the Friedmann equation (1.10) scales as a^{-2}. Therefore, in the radiation or matter dominated eras, where we can neglect Λ, the relative contribution of the curvature term grows as the universe expands [82]. As a consequence, even a small deviation from a perfectly flat universe gets amplified over time. The lack of spatial curvature in today's universe hence tells us that the radiation- and matter-dominated evolution must have started from a nearly perfectly flat state.

It is easy to see how an inflationary period driven by a constant vacuum energy can create these initial conditions naturally [83] if we rewrite Eqn. (1.6) as

$$(\Omega(a) - 1)H^2a^2 = k\,. \tag{1.20}$$

The RHS of this equation is a constant, but as we discussed, during inflation also the Hubble parameter approaches a nearly constant value. This means, in this case, $\Omega(a) - 1$ will scale reciprocally with the square of the scale factor; in other words, the accelerated expansion drives the energy density to its critical value. Conveniently, a size increase of the universe of the order of 10^{30}, inferred by the requirement of inflation solving the horizon problem, leaves us with just the right amount of flatness after inflation necessary to explain the established present-day limits on the universe's curvature [77].

1.3.3 Slow-Roll Inflation and the Reheating Epoch

As we discussed above, the inflationary paradigm can very successfully solve some of the problems a purely standard cosmological evolution would raise and explain a number of the apparent coincidences observed in our universe. Nevertheless, asserting that the inflationary period in the very early universe indeed took place raises a new question: what was the key driver behind this rapid expansion? A possible explanation is given by scalar field cosmology. Let again ϕ be a scalar field with an associated self-interaction potential given by $V(\phi)$. For now, we will consider a homogeneous field, whose spatial gradients vanish. From (1.16) and (1.17) we can see that ϕ behaves as a perfect fluid with a proper energy density and isotropic pressure respectively given by

$$\rho = \frac{1}{2}\dot{\phi}^2 + V(\phi) \quad \text{and} \quad p = \frac{1}{2}\dot{\phi}^2 - V(\phi)\,. \tag{1.21}$$

Eqn. (1.21) shows that if the field's potential energy dominates over the kinetic term proportional to $\dot{\phi}^2$, it can mimic a cosmological constant with an equation of state $w = -1$ [66, 84].

Taking the time derivative of the Hubble parameter, we may write

$$\frac{\ddot{a}}{a} = \dot{H} + H^2 = H^2\left(1 - \frac{\dot{H}}{H^2}\right) \equiv H^2\left(1 - \epsilon_{\mathrm{H}}\right)\,. \tag{1.22}$$

Here we have defined the Hubble slow-roll parameter ϵ_{H} [85]. Accelerated expansion of the universe requires $\ddot{a}/a > 0$ and hence $\epsilon_{\mathrm{H}} < 1$. Let us consider a light scalar field, for which the derivative of the potential $V' \equiv dV(\phi)/d\phi$ is much smaller than V itself. In this

case, one expects the acceleration of the field (i.e. its second time derivative $\ddot{\phi}$) to be negligible along its trajectory, and it will roll down the potential with a "terminal velocity" that is reached when the gradient of the potential balances the Hubble damping:

$$3H\dot{\phi} = -V' \,. \tag{1.23}$$

If the scalar field dominates the energy budget of the universe, using (1.21) the Friedmann equation (1.6) becomes

$$H^2 = \frac{8\pi G}{3}\left(\frac{\dot{\phi}^2}{2} + V(\phi)\right) \,, \tag{1.24}$$

and we can write the slow-roll parameter as

$$\epsilon_{\mathrm{H}} = \frac{3\dot{\phi}^2}{2V + \dot{\phi}^2} \,. \tag{1.25}$$

For a sufficiently flat potential, it follows from Eqn. (1.23) that the field's velocity will be close to zero, $\dot{\phi} \approx 0$, which in turn implies $\epsilon_{\mathrm{H}} \ll 1$. This is precisely the regime in which, according to (1.22) the universe undergoes accelerated expansion and (1.24) shows that this expansion is dominated by the field's potential. In contrast to earlier theories of inflation [67], where the accelerated expansion was triggered by a first-order phase transition, most modern approaches are based on this so-called slow-roll inflation [86]. In fact, there is a plethora of slow-roll models, for example invoking power-law [87, 88] or exponential [89] shapes of the potential, multiple scalar fields [90, 91], or models in which the Higgs field of the Standard Model of Particle Physics plays the role of the inflaton [92] — that is the scalar particle associated with the field that drives inflation.

During inflation, most of the energy density of the universe is stored in the inflaton field potential. As the scalar field rolls down more and more towards its potential minimum, however, the slow-roll condition can break down (this breakdown can also be triggered by a second scalar field coupled to the inflaton, as e.g., in hybrid inflation models [93]). Then the Hubble friction can become subdominant and the field will start to accelerate. Sufficiently close to its minimum, the potential takes, up to leading order, a quadratic shape $V(\phi) \approx (m^2/2)\phi^2$. In this case, the field's equation of motion resembles a harmonic oscillator with

$$\ddot{\phi} + m^2\phi = 0 \,. \tag{1.26}$$

The oscillation of the field around its minimum transfers the potential energy stored in the field into inflatons. Through interaction terms in the Lagrangian of the form

$$\mathcal{L}_{\text{int}} \subset \lambda_j \phi \Psi_j \bar{\Psi}_j \,, \tag{1.27}$$

with Ψ_j being fermionic fields and λ_j some coupling constant, these inflatons can decay into lighter standard model particles. If this decay rate becomes large enough, essentially all the energy of the inflaton field gets transferred into standard model (and potentially dark sector) particles, which in turn can thermalize via the standard model interactions. This process is called reheating [94, 95].

1.3.4 Implications of Inflation for Structure Formation

Although the large-scale evolution of our universe can be described using classical physics, quantum fluctuations played a crucial role in its early development. Scalar fields, even when in their ground states, are subjected to vacuum fluctuations, which cause them to constantly produce virtual particle pairs [96, 97]. While under normal circumstances they would quickly annihilate, during the inflationary period fluctuations can get pushed out of the horizon, thereby manifesting themselves as physical density fluctuations. It is possible to show that the power spectrum produced by those stretched-out quantum fluctuations is almost scale-invariant [98]. The theory of linear structure formation then describes how these fluctuations act as seeds for dark matter halos to form, which will later themselves trigger the formation of galaxies, galaxy clusters, etc. in a bottom-up fashion [43, 66]. Indeed, measurements of the power spectrum of the CMB and BAOs confirm that the initial conditions leading to the presently observed distribution of matter in our universe must have been almost scale-invariant density perturbations [75, 99]. The inflationary paradigm provides a natural explanation for them. Also, small deviations from scale-invariance can be related to parameters of the inflaton potential and may therefore be used to constrain inflationary models.

1.4. Cosmic Topological Defects

Quantum fluctuations of a scalar field lead to density perturbations in an otherwise perfectly homogeneous background, thereby triggering the formation of the coarse-grained structure that we observe today. Through a mechanism known as spontaneous symmetry breaking, scalar fields can also give rise to topologically stable defects, which introduce inhomogeneities in a purely classical manner [100, 101]. By now, these defects have been ruled out as the main source of structure formation [102], although possibly providing an important contribution on small scales [24, 27, 103–105]. Still, cosmic defects continue to be a topic of active research, since they lie at the interface between cosmology and particle physics. Symmetries that might have been broken in the very early universe and that are far out of reach of state-of-the-art particle colliders would be unbroken in their cores. Let us briefly review the Kibble mechanism that can lead to the formation of topological defects in the early universe.

1.4.1 Defect formation: The Kibble Mechanism

In particle physics, fundamental interactions are described by their underlying symmetry groups. It is known that above a temperature of around 250 GeV, the electromagnetic and weak force combine into an electroweak interaction, which can be described by a SU(2) $\times$ U(1) symmetry [106]. Analogously, there exist several grand unified theories that propose the merger of this electroweak force with the strong force at much higher energies of around $10^{15} - 10^{16}$ GeV [77, 107]. In hot big bang cosmology, therefore, the forces of the Standard Model of Particle Physics would have been unified in the very early universe. As the universe expands and cools, *phase transitions* that have close analogues in thermodynamics would then occur, leading to a spontaneous breaking of symmetry. These phase transitions can be classified into first- and second-order phase transitions. First-order phase transitions occur when there is a sudden transition from a meta-stable state into a true vacuum state of a scalar field ϕ. They are therefore characterized by a discontinuous change in the order parameter (the value of ϕ) and may be triggered, for example, by quantum tunneling processes [100]. First-order phase transitions therefore cause bubbles of true vacuum in space that can then, depending on what is energetically favorable, either re-collapse on themselves or expand until they collide and merge with other true vacuum bubbles [80, 108, 109].

To illustrate the formation of cosmic defects we will, for simplicity, consider second-order phase transitions, which are characterized by a continuously changing order parameter.

A useful toy model to study these transitions in more detail is the Goldstone model, which is described by the Lagrangian from equation (1.11) with a quartic potential (therefore often referred to as ϕ^4-theory) of the form

$$V(\phi) = \frac{\lambda}{4}(\bar{\phi}\phi - \eta^2)^2 \,. \tag{1.28}$$

Here, the self-coupling parameter λ and the symmetry breaking scale η are positive constants. This Higgs or Mexican hat potential is shown in figure 1.1.

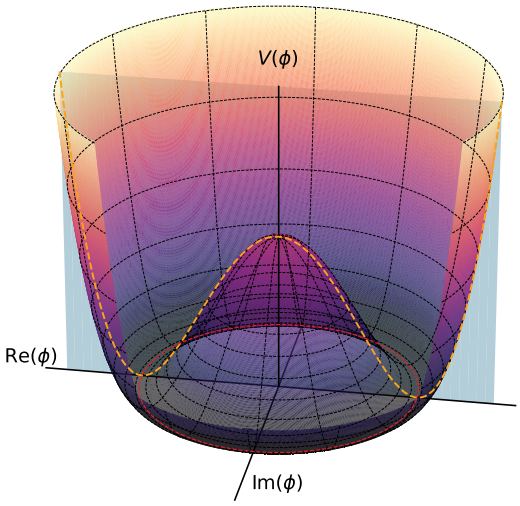

Figure 1.1: The Higgs (Mexican hat) potential $V(\phi)$ for a complex-valued scalar field ϕ. The potential's minima lie along a circle of radius η in the complex plane. The orange curve represents the case of a real-valued scalar field, where there are two discrete vacuum expectation values at $\phi_0 = \pm\eta$.

At non-zero temperature, there is a thermal distribution of particles that are in thermal equilibrium with the field ϕ. This leads to thermal corrections to the potential (1.28). If one defines an effective potential

$$V_{\text{eff}}(\phi, T) = \frac{F(\phi, T)}{\mathcal{V}} \,, \tag{1.29}$$

given by the free energy $F = E - TS$ per volume $\mathcal{V}$, one can show [100] that the high temperature effective potential for the Goldstone model can be written as

$$V_{\text{eff}}(\phi, T) = \frac{1}{2}m^2(T)|\phi|^2 + \frac{\lambda}{4}|\phi|^4 \,, \tag{1.30}$$

where

$$m^2(T) = \frac{\lambda}{12}(T^2 - 6\eta^2)\,. \tag{1.31}$$

Hence, there is a critical temperature $T_c = \sqrt{6}\eta$ at which a phase transition occurs. For $T > T_c$ the field acquires a positive mass, stabilized by the interactions with the thermal bath of particles, leading to a Higgs expectation value of $\langle|\phi|\rangle = 0$. This symmetric state, however, becomes unstable as the temperature approaches T_c. For $T < T_c$ the effective potential (1.30) is minimized by a value of the field

$$|\phi| = \frac{1}{\sqrt{6}}(T_c^2 - T^2)^{\frac{1}{2}}\,. \tag{1.32}$$

In this regime the expectation value of the absolute of ϕ then continuously grows as T decreases further below the critical temperature (thereby fulfilling the defining property of a second-order phase transition) until it approaches an asymptotic value of $\langle|\phi|\rangle = \eta$ at low temperatures [110].

So far we have not specified any details of the field ϕ. In the case of a single real scalar field we have $\bar{\phi}\phi = \phi^2$ and the model (1.28) is invariant under reflections $\phi \to -\phi$. In the low-temperature limit, the Vacuum Expectation Values (VEVs) of the system are then given by $\langle\phi\rangle = \pm\eta$. In the case of a complex-valued field, on the other hand, (1.28) is invariant under U(1) transformations, and the vacua describe a circle in the complex plane that can be parameterized as $\langle\phi\rangle = e^{i\theta}\eta$. Importantly, Kibble argued that the choice of which of these distinct vacuum states will be picked by the field at the moment the phase transition occurs depends on local random thermal fluctuations. Moreover, this choice cannot be correlated over distances greater than the causal horizon at the time of the breaking of the symmetry [22]. Those random VEVs in different causal patches of the universe represent non-trivial boundary conditions that lead to the formation of cosmic defects. To be more specific, the simple Goldstone model presented above may give rise to the formation of global strings in the case of a complex-valued scalar field, and to the formation of domain walls if the field is real-valued. In the next section, we will discuss what the different types of defects are and when they emerge.

1.4.2 Classification of Topological Defects

Cosmic defects may be categorized by the topology of the vacuum manifold defined by the model. More formally speaking, let the group G be a symmetry of the system, so that the Lagrangian of the underlying field theory model is invariant under actions of G. If the system acquires a VEV ϕ_0, then the set of field configurations obtained by applying the group transformations of G to this vacuum state will return all possible states that minimize the Hamiltonian – the vacuum manifold. This vacuum manifold is isomorphic to the coset space $\mathcal{M} \equiv G/H$, where H is the unbroken subgroup of G, whose elements leave the vacuum state ϕ_0 unchanged. If one of the homotopy groups $\pi_n(\mathcal{M})$, i.e., the groups that contain continuously deformable maps from an n-sphere to the coset space $\mathcal{M}$, has non-trivial elements — $\pi_n(\mathcal{M}) \neq \mathbb{1}$ — topological defects form, provided there are non-trivial boundary conditions. Loosely speaking, this happens because in physical space fields must continuously interpolate between configurations in different vacua, but bringing them arbitrarily close together might not be possible if the field is constrained to exclusively take values within the vacuum manifold. We will discuss an example of this more closely in section 2.1.

The type of defect one can expect to form depends only on the order n of the homotopy groups that contain non-trivial elements, as is shown in the table below [111].

$n = 0$	Domain walls (2D)
$n = 1$	Strings (1D)
$n = 2$	Monopoles (point like)
$n = 3$	Textures

The dimensionality of defects in physical space is reciprocal to the order n of the non-trivial homotopy groups. Monopoles are point-like field configurations, while cosmic strings manifest themselves as line-like defects forming a network in space.

Most of these defects are thought to be long-lived and, if formed after or towards the end of inflation, they might still be present within our observable universe. They might then be detectable through different channels. The aforementioned magnetic monopoles are arguably the experimentally most accessible class of defects [23]. Several efforts have been made to detect them using superconducting devices [112], searches in cosmic rays [73], or even attempts to produce them in particle colliders [72]. Cosmic strings, on the other hand, can be superconducting themselves, in which case they can source

primordial magnetic fields [113–115]. Also, they would produce a tell-tale gravitational lensing signal, which astronomers keep looking for in large-scale galaxy surveys [116, 117]. More peculiar effects associated with cosmic strings that have been proposed in the literature include that they might be detectable by causing earthquakes when passing through our planet [118] or be able to spin down black holes they are attached to [119].

Recently, with the detection of gravitational waves from astrophysical sources in ground-based interferometers [120, 121], the confirmed detection of a SGWB from various PTA experiments [34–37] and with complementary frequency windows being probed by other present-day and future observatories [38, 39], efforts to detect defects have increasingly shifted towards GW astronomy [39, 122–137]. Both a successful detection of cosmic defects and the constraining of the parameter space by increasing the sensitivity of experiments can help to verify or falsify specific models of particle physics or even quantum gravity. The remainder of this thesis will be focused on cosmic domain walls. They may arise if there is a discrete set of unconnected minima in the scalar field potential and then, in physical space, form a two-dimensional boundary between regions in different vacuum states.

2. Domain Walls in Cosmology: A Brief Overview of the State-of-the-Art

Domain walls are predicted in various theories of particle physics, such as in GUTs or axion models. In the latter case, they might form hybrid networks, in which they are attached to cosmic strings. Axion domain walls have also been proposed as a contributor to dark matter, either directly via the radiation of dark axions [138, 139] or through the formation of primordial black holes, triggered by the collapse of walls [140, 141]. Domain walls that become frustrated (i.e. frozen in comoving coordinates) would behave as a perfect fluid with $w = -2/3$, making them even a potential contributor to the recent accelerated expansion of the cosmos [142]. These expectations, however, were not fulfilled, as it was shown that the necessary field configurations are artificial and would not arise in realistic networks, even if one assumes non-standard domain wall networks with a number of coupled scalar fields that form junctions [31, 143–145].

Various mechanisms have been proposed to detect domain walls experimentally. Most prominently, these include searches in gravitational wave data, as the recently reported SGWB signals from various PTA collaborations such as NANOGrav, the Parkes Pulsar Timing Array (PPTA), the European Pulsar Timing Array (EPTA), and the Chinese Pulsar Timing Array (CPTA) [34–37]. Yet, other mechanisms have been studied in the literature as well. If domain walls were coupled to photons, ground-based gravitational wave detectors such as LIGO could detect optical effects in their laser interferometer [146]. Moreover, a passage of a domain wall coupled to electromagnetism could cause changes in the fine-structure constant, thus changing the ticking rate of atomic clocks [29, 147] or the frequency of quasar absorption lines [16]. Observational constraints on the mass scale of stable domain walls have also been inferred from the CMB [103, 148]. Stable domain walls violating these constraints would eventually come to dominate the energy budget of the universe (as detailed in sections 2.2 and 2.4). To avoid this so-called *domain wall problem*, it is common to assume that domain wall networks might be rendered unstable, e.g. by a bias in the scalar field potential or the initial population of the vacuum states [149–155].

Cosmic domain walls have been studied in numerous field theory simulations [156–159] with steadily increasing dynamical ranges. Those simulations have been used to study the emission of scalar or gravitational radiation from domain wall networks or to confirm

the stability of domain walls formed from varying initial conditions [160]. In addition, the interaction of domain walls with massive objects has been investigated in field theory simulations [161, 162]. These simulations suggest that the interaction with a domain wall could alter the trajectory of man-made satellites in Earth's orbit [163] or — on a larger scale — explain the clustering of orbits of galactic satellites around the Milky Way [30]. The largest domain wall simulations up to the present day, however, have been performed to accurately calibrate the Velocity-dependent One-Scale (VOS) model [164–166]. This semi-analytical model describes the large-scale dynamics of domain wall networks but has two free parameters that cannot be derived from first principles. Recently, a new model was proposed that can describe the networks' dynamics without free parameters [167]. We will discuss these models in more detail in the sections 2.2 and 2.3, respectively. Before, we will illustrate the formation of domain walls as well as some of their properties in the Goldstone model.

2.1. Domain Walls in the Goldstone Model

The Goldstone model (1.11, 1.28) for a single real-valued scalar field is invariant under reflections $\phi \to -\phi$. In group theoretical terms, this can be phrased as the Lagrangian being invariant under transformations belonging to the cyclic group of order two, $G = \mathbb{Z}_2$. The vacuum states of the model are discrete and point-like: $\langle\phi\rangle = \pm\eta$. Hence, only trivial transformations leave the vacuum states unchanged, from which it follows that the unbroken subgroup H only contains the identity element and therefore $\mathcal{M} = G/H = \mathbb{Z}_2$. Now, since there is no unique mapping from S_0 to $\mathbb{Z}_2$, the zeroth homotopy group $\pi_0(\mathcal{M})$ is non-trivial, and thus this model allows for the formation of domain walls [111]. To discuss some of their basic features, it is useful to break down the problem into 1+1 dimensions (in which case domain walls are also referred to as kinks). Moreover, we will introduce a different parameterization of the Higgs potential (1.28) here, which is commonly used in the literature. It is given as

$$V(\phi) = V_0 \left(\frac{\phi^2}{\phi_0^2} - 1 \right)^2 , \tag{2.1}$$

and one can easily identify $V_0 = \lambda\eta^4/4$ and $\phi_0 = \eta$. For now, we will restrict ourselves to a Minkowski spacetime with the line element $ds^2 = dt^2 - dx^2$. The goal is to find a static (i.e. $\dot{\phi} = 0$) solution to the equation of motion (1.14), which in this case reduces to

$$\frac{d^2\phi}{dx^2} - \frac{dV}{d\phi} = 0 . \tag{2.2}$$

We want this solution to interpolate between the two different vacuum states $\langle\phi\rangle = \pm\phi_0$ at spatial infinity $x = \pm\infty$. Indeed, an analytic solution to this boundary value problem can be found as [100]

$$\phi(x) = \phi_0 \tanh\left(\frac{\sqrt{2V_0}}{\phi_0}x\right) . \tag{2.3}$$

This solution describes a kink centered around $x = 0$ in 1+1 dimensions, but it may be trivially embedded in 3+1 dimensions, where it describes a planar, infinitely extended domain wall in the yz-plane. Domain walls may then be regarded as 2+1 dimensional boundaries between regions where ϕ is in different vacua. In the case of an arbitrary fragmentation of the universe into several domains with different vacua, generated by random quantum fluctuations in the early universe, one speaks of a domain wall network.

Eqn. (2.3) also allows us to define a wall thickness w_0, which roughly corresponds to the region in space that is not in a vacuum state:

$$w_0 = \frac{\pi\phi_0}{\sqrt{2V_0}} . \tag{2.4}$$

The simple solution (2.3) may be used to define the velocity of the domain wall, too. By applying a Lorentz boost in the direction perpendicular to the wall, we can write eq (2.3) as

$$\phi(x,\, t) = \phi_0 \tanh\left(\frac{2\sqrt{V_0}}{\phi_0}\gamma(x - vt)\right) , \tag{2.5}$$

where $\gamma = (1 - v^2)^{-\frac{1}{2}}$ is the Lorentz factor. With the substitution $l = \gamma(x - vt)$ the EOM of the field becomes

$$\frac{d^2\phi}{dl^2} = \frac{dV}{d\phi} \Leftrightarrow \left(\frac{d\phi}{dl}\right)^2 = 2V . \tag{2.6}$$

Together with

$$\frac{d\phi}{dt} = -\gamma v\frac{d\phi}{dl} \quad \text{and} \quad \frac{d\phi}{dx} = \gamma\frac{d\phi}{dl} , \tag{2.7}$$

it follows that

$$\gamma^2 v^2 = \frac{\dot{\phi}^2}{2V} . \tag{2.8}$$

Moreover, we can use Eqn. (1.16) to find the distribution of the energy density within the static solution (2.3). This is given as

$$\rho(x) = \frac{2V_0}{\phi_0^2}\,\mathrm{sech}^4\left(\frac{\sqrt{2V_0}}{\phi_0}x\right) . \tag{2.9}$$

Integrating over Eqn. (2.9) shows that the mass per unit wall area σ is finite:

$$\sigma = \int_{-\infty}^{\infty} \rho(x)\, dx = \frac{\sqrt{32V_0}}{3}\phi_0\,. \tag{2.10}$$

As the energy-momentum tensor can be written (in 3+1 dimensions) as

$$T_{\mu\nu} = \rho(x)\,\mathrm{diag}[1, 0, -1, -1]\,, \tag{2.11}$$

it is also common to refer to σ as the tension of the domain wall.

The properties discussed above were inferred by assuming flat walls in a non-expanding background. Yet, FLRW universes are locally isomorphic to Minkowski space and typically the curvature radii of the walls are much larger than their thickness. Hence, evaluated locally, the expressions derived here also hold for walls in a realistic cosmic defect network. Additionally, it is worth noting that the ϕ^4 domain walls described in this section arise in many theories of particle physics, and the Goldstone model has proven to be a simple and useful toy model to study some generic aspects of domain walls. Nevertheless, there are a multitude of other models that allow for the formation of walls. In axion models, e.g., the potential typically takes the shape

$$V(\theta) = \frac{m^2\eta^2}{N_{\mathrm{DW}}^2}\left(1 - \cos\left(N_{\mathrm{DW}}\theta\right)\right)\,, \tag{2.12}$$

where θ is the axion field, m is its mass, and N_{DW} is the number of distinct vacuum states [168–170]. The details of these models can play an important role when studying certain microscopic aspects of the domain walls, such as the production of scalar radiation or the interaction with other fields. As we will see in the next chapter, however, the macroscopic dynamics of a domain wall network are mostly governed by the interplay between the wall's tension and curvature and are hence to a certain degree model independent.

2.2. Modeling Domain Wall Network Evolution I: The Velocity-Dependent One-Scale Model

In our previous discussions, we have focused on the field-theoretical aspects of cosmic defects arising from symmetry-breaking phase transitions in the early universe. By studying the Goldstone model, we observed that specific particle physics models result in unique configurations of field and energy density distributions in space. While these model-dependent properties need to be taken into account when studying the microscopic behavior and interactions of domain walls, and some of these properties, like the emission of radiation, can also influence the macroscopic behavior of walls, it is not trivial to extrapolate the large-scale behavior of domain wall networks from the equations of motion of the field. Precisely this task of understanding the macroscopic properties of defects, however, is essential in cosmology. The density of cosmic defects, but also their dynamics, will influence the way these defects can contribute to structure formation and leave imprints on the CMB. Moreover, these properties can affect the gravitational wave spectrum expected from defects or — as we will see — have the potential to alter the large-scale evolution of the universe itself.

In this section, we will review the velocity-dependent one-scale model, which aids in understanding these large-scale dynamics. Its equations are independent of underlying field theory models, but it may account for an implicit model dependence through the calibration of its free parameters. This model was first introduced for cosmic strings [171], and later extended to accommodate cosmic domain walls and other topological defects [172–174]. It describes domain walls essentially as featureless 2-branes that are thin in the sense that their thickness is much smaller than their curvature radii. In this case, it is possible to construct an orthonormal set of coordinates ζ^a, $a = 0, 1, 2$, in the vicinity of the walls, and their Lagrangian density is, to leading order, given by the worldsheet volume they sweep in a 3+1 dimensional spacetime, multiplied by their tension. Thus the action can be written as

$$S = -\sigma \int d^3\zeta \sqrt{\gamma}\,, \tag{2.13}$$

where $\gamma = \det(\gamma_{ab})$ and $\gamma_{ab} = x^\mu_{,a} x^\nu_{,b}$ is the metric induced on the worldsheet. Eqn. (2.13) can be seen as the generalization of the action of a massive point particle to higher dimensions and is called Nambu-Goto action, or in the special case of a 2-brane, also referred to as Dirac action. The equations of motion resulting from this action have been derived in [174] but are difficult to solve for domain walls in full generality. However, by assuming energy and momentum conservation of the network in the expanding background,

as well as a homogeneous and isotropic distribution of the domain walls on sufficiently large scales, it is possible to obtain averaged expressions. A posteriori, one can then add heuristic terms that account for possible energy losses of the network.

The VOS model assumes that there is a single characteristic length scale L that can roughly be interpreted as the mean wall separation, which is of the same order as both the correlation length and the average curvature radius of the walls. This length scale is defined through the mean energy density of the domain wall network $\bar{\rho} = V^{-1} \int \rho \, dV$ as

$$L = \frac{\sigma}{\bar{\rho}} \,. \tag{2.14}$$

Moreover, one can define the wall's Root Mean Squared (RMS) velocity as

$$\bar{v}^2 = \frac{\int v^2 \rho \, dV}{\int \rho \, dV} \,, \tag{2.15}$$

and we will assume that $\langle v^4 \rangle = \bar{v}^4$ holds to good approximation. Then in the VOS model the evolution of these quantities is given as a set of coupled first-order differential equations, which can be written as

$$\frac{dL}{dt} = HL + \frac{L}{l_d} \bar{v}^2 + \tilde{c} \bar{v} \tag{2.16}$$

$$\frac{d\bar{v}}{dt} = (1 - \bar{v}^2) \left(\frac{k_w}{L} - \frac{\bar{v}}{l_d} \right) \,. \tag{2.17}$$

These equations contain two free parameters that may be calibrated with simulations. The first of these, k_w, is a dimensionless curvature parameter that, to some extent, describes the average domain wall curvature. The second parameter, $\tilde{c}$, was introduced to quantify the efficiency of the energy loss associated with the collapse of the domain walls. While for cosmic string networks the k_w typically adopts a velocity dependence, for domain wall networks it was shown that choosing both k_w and $\tilde{c}$ as constant for a fixed background cosmology is a good approximation*. Moreover, we introduced the damping length scale $l_d^{-1} = 3H + l_f^{-1}$ in (2.16, 2.17) that includes the cosmological Hubble damping term as well as the friction length scale l_f. This friction length in turn accounts for domain walls scattering off particles in the hot, dense plasma of the early universe. If N_w is the number of particle species scattering off the domain wall, we can write

$$l_f = \frac{\sigma}{N_w T^4} \,. \tag{2.18}$$

*Notice, however, that extensions to the VOS model for cosmic domain walls with a larger number of degrees of freedom have been proposed in literature [159, 175]

Since the hot plasma behaves as radiation and gets diluted by the expanding background, this friction length scale grows as a^4 and quickly approaches infinity. This essentially splits the typical evolution of a domain wall network into two epochs. In its first stages, the dynamics are dominated by the frictional forces the walls experience [176–178]. In the so-called Kibble regime, the network is very dense and at the same time the rate of energy loss is high, leading to a quick growth of the characteristic length scale with $L \propto t^{3/2}$ in the radiation era. At the same time, the frictional forces keep the average wall velocities low. Depending on the correlation length at the time of formation of the network, the Kibble regime might be preceded by a likewise friction-dominated stretching regime in which L grows at the same rate as the scale factor.

Due to its scaling with the temperature of the surrounding plasma, the friction-dominated epochs, however, are not only transient but often also short-lived (although this may not hold true for very light walls). Once frictional forces are negligible, domain wall dynamics are governed by the interplay between their tension, which causes a tendency for domains to collapse, and the Hubble damping due to the expanding background. In this regime, domains of the size of the (growing) Hubble horizon will detach from the network and quickly decay at a rate that depends on the background cosmology. The energy loss the network hence experiences is expressed by the last term in Eqn. (2.16). Setting the friction length to infinity, $l_f = \infty$, and assuming a decelerating power-law expansion of the universe, the VOS equations have an attractor solution usually referred to as the linear scaling regime. In this regime, L grows linearly with cosmic time, such that $L = \xi_\lambda t$, and $\bar{v} = \bar{v}_\lambda$ remains constant, where

$$\xi_\lambda = \sqrt{\frac{k_w(k_w + \tilde{c})}{3\lambda(1-\lambda)}}, \quad \bar{v}_\lambda = \sqrt{\frac{k_w(1-\lambda)}{3\lambda(k_w + \tilde{c})}}, \tag{2.19}$$

λ here being the power-law exponent of the scale factor $a(t) \propto t^\lambda$ as introduced in section 1.1 [166, 179]. The linear scaling regime is particularly useful to calibrate the free parameters of the VOS model, as ξ and $\bar{v}$ can easily be measured from large-scale field theory simulations of frictionless domain wall networks [159, 166] (see chapter 3).

From Eqn. (2.14) it is obvious that $\rho_{\mathrm{dw}} \equiv \bar{\rho} \propto t^{-1}$. On the other hand, in section 1.1, we have seen the energy density of the background in the decelerating epochs of the cosmic

evolution depends on the cosmic time as

$$\rho \propto \begin{cases} a^{-4} \propto (t^{\frac{1}{2}})^{-4} & \text{for } \lambda = 1/2 \\ a^{-3} \propto (t^{\frac{2}{3}})^{-3} & \text{for } \lambda = 2/3 \end{cases} \propto t^{-2}\,, \tag{2.20}$$

implying a linear growth of the energy density in domain walls with time relative to the cosmological background. This leads to the so-called *domain wall problem* in which walls would eventually dominate the energy budget of the universe. We will discuss the domain wall problem in more detail in section 2.4. Before that, we will introduce a more recent model describing the dynamics of domain wall networks: the parameter-free VOS model.

2.3. Modeling Domain Wall Network Evolution II: The Parameter-Free Velocity-Dependent One-Scale Model

The standard VOS model describes the evolution of two thermodynamic quantities which track the large-scale dynamics of the network. Despite its simplicity — it only requires solving first-order differential equations — this model is also versatile in the sense that it can easily model the evolution of domain wall networks throughout their entire lifetime, starting from the early friction-dominated eras. On the downside, however, the standard VOS model cannot predict the evolution of the aforementioned quantities from first principles, but requires the calibration of its free parameters with field theory simulations. These simulations come with their own limitations, which might induce inaccuracies in the predictions of the VOS model in certain regimes (as will be discussed in section 4.3). In addition, despite the VOS equations themselves being derived in a model-independent way, with the calibration of their parameters, they acquire an implicit dependency on the model used in the underlying field theory simulation.

The recently proposed Parameter-Free velocity-dependent one-scale Model (PFM) [167] provides an independent way of estimating L and $\bar{v}$ in the cosmologically most relevant scenarios that does not rely on the results of simulations. The model is built upon the well-motivated assumptions that in standard domain wall networks, collisions between walls occur rarely and that no significant energy loss due to scalar radiation is expected, except in the late stages of collapse [180]. Therefore, the evolution of networks is predominantly determined by nested domains that will successively collapse once they enter the horizon. In the PFM, this behavior is separately modeled for spherical and cylindrical walls with a given initial distribution of radii. The consideration of both spherical and cylindrical configurations makes it possible to evaluate the impact of geometry on the model predictions. At the same time, realistic domains are expected to be enclosed between these

limiting cases. This is because although initially domains can form with more complicated geometries, regions on the wall with higher intrinsic curvature will smooth out before the respective domain fully enters the horizon.

Similarly to the VOS model, the parameter-free model assumes thin domain walls without any internal structure, which are then again described by the Nambu-Goto action (2.13). Although the general equations of motion are nontrivial to solve, in the above-mentioned cases with a simpler geometry, this is easily possible. Here, it is useful to introduce the invariant radius $R = \gamma^{\frac{1}{s}} aq$, where s equals 1 (2) in the cylindrical (spherical) case, and q denotes the radius in comoving coordinates. R^s is proportional to the total energy of the wall (spherical case) or the energy per unit length (cylindrical case), and is a conserved quantity in a Minkowski spacetime:

$$E = 2\pi s \sigma R^s \,. \tag{2.21}$$

Finally, with $v = dq/d\eta$ and introducing the conformal Hubble parameter $\mathcal{H} = a^{-1}(da/d\eta)$ one can obtain equations for the evolution of the velocity and the invariant radius:

$$\frac{dv}{d\eta} = -\gamma^{-2}\left(\frac{s}{q} + 3\mathcal{H}v\right) \quad \text{and} \quad \frac{dR}{d\eta} = \mathcal{H}R\left(1 - \frac{3}{s}v^2\right) \,. \tag{2.22}$$

For spherical or cylindrical walls that are initially at rest, the velocity will only increase very slowly while $q \gg \mathcal{H}^{-1}$. In this regime, the walls are conformally stretched by the expansion, which leads to an increase in their total energy (spherical case) or energy per unit length (cylindrical case). When their radius gets comparable to the Hubble radius, they start to collapse, accelerating to ultra-relativistic velocities in the late stages of collapse. Once a threshold velocity of $v = \sqrt{s/3}$ is reached, instead of further increasing it, the expansion of the universe causes a decrease in energy (per unit length in the cylindrical case).

For a power-law cosmology, equations (2.22) are invariant under a rescaling $q \to \vartheta q$ and $\eta \to \vartheta \eta$ for an $\vartheta > 0$. This allows us to describe the collapse of spherical or cylindrical domains independently of their initial size. Choosing $\vartheta = q_i^{-1}$, where q_i is the initial comoving radius of the domain, we obtain the new variables

$$\tilde{q} = \frac{q}{q_i} \quad \text{and} \quad \tau = \frac{\eta}{q_i} \,. \tag{2.23}$$

Then it follows that there will be a threshold $\tau_\star = \eta/q_{i\star}$, that only depends on λ, such that all domains with an initial radius smaller than $q_{i\star}$ will have collapsed at the corresponding

η, or equivalently, $\tilde{q}(\tau_\star) = 0$. We shall now assume a network of domain walls with a probability distribution of the initial domain radius that is given by

$$P(q_i) = (1+s)\eta_i^{1+s} q_i^{-2-s} \Theta(q_i - \eta_i)\,, \tag{2.24}$$

where Θ is the Heaviside step function and η_i the initial conformal time. The shape of this initial distribution is vital to ensure that the network can eventually enter a linear scaling regime. We can now compute the (average) energy density $\rho_{\rm dw}$ of all domain walls in the network that survived up to a conformal time $\eta \gg \eta_i$ (in other words, of those with an initial radius $q_i > q_{i\star}$):

$$\rho_{\rm dw}(\eta) = \int_{q_{i\star}}^{\infty} n(\eta) E(\eta, q_i) P(q_i) dq_i\,. \tag{2.25}$$

This expression is valid for any $\lambda \in]0,\, 1[$, $n(\eta) = n_i a^{-1-s}$, n_i being the initial number of walls per unit volume/unit area in the spherical/cylindrical case and $E(\eta, q_i)$ can be calculated with Eqn. (2.21). Eqn. (2.25) allows us to calculate the characteristic length L using Eqn. (2.14) and we define $\zeta \equiv L/(a\eta)$. Since the network, in a decelerating power-law cosmology, will quickly approach a linear scaling regime, ζ is expected to be a constant akin to ξ defined in Eqn. (2.19). In fact, one may simply show that in this regime ζ and ξ are related through $\zeta = (1-\lambda)\xi$. In the parameter-free model ζ is then given by

$$\zeta = \left(\beta \int_0^{\tau_\star} \tilde{q}^s(\tau) \gamma(\tau) d\tau \right)^{-1}. \tag{2.26}$$

Here we introduced $\beta = 2\pi s(1+s) n_i \eta_i^{1+s}$, which can be calculated if the initial number density of domain walls is known. Moreover, we can obtain an expression for $\bar{v}^2$ by computing the average of v^2 via

$$\bar{v}^2 = \frac{\int v^2 \rho dV}{\int \rho dV} = \xi\beta \int_0^{\tau_\star} v^2 \tilde{q}^s(\tau) \gamma(\tau) d\tau\,. \tag{2.27}$$

The equations (2.26) and (2.27) may be used to calculate the scaling constants ζ and $\bar{v}$ in a way that is independent of the underlying field theory model and the results of simulations. These values have been calculated in the literature for a range of λs in $]0,\, 1[$, and then compared to results from field theory simulations [167]. We will get back to this in more detail in chapter 4.

2.4. Biased Domain Walls and Their Decay Mechanisms

So far, we have assumed that domain walls are stable and that the networks they form survive until the present day. However, as we have seen in section 2.2, the ratio between the energy density of a scaling domain wall network and that of the background is a growing function of time in both the radiation- and matter-dominated eras. As a result, these walls would generally be expected to leave strong observational signatures in the large-scale structure of the cosmos. Still, the absence of these imprints can have multiple explanations. Domain walls may have never formed or could have formed before or during cosmic inflation, therefore being pushed out of the Hubble horizon. On the other hand, domain walls that formed late in cosmic history could be light enough to evade current observational limits on domain wall tension. These limits were first derived by Zel'Dovich and later improved with more recent CMB data. This has led to strong constraints on the energy scale of the domain-wall-forming phase transition, as walls that form at a scale of $\eta \gtrsim 1\,\mathrm{MeV}$ would, if they survived up to the present epoch, leave detectable imprints on the Cosmic Microwave Background [103, 148].

Yet another solution to the problem has been discussed extensively in the literature: networks of heavy domain walls could have formed early in cosmic history but decayed shortly after. Such a decay can be caused by a bias in the scalar field potential that gives rise to the domain walls, for example, if one of the vacuum states is initially more likely to be populated [181] or if the energy densities of the minima of the potential are slightly different [182]. The first case of the so-called *population bias* is illustrated in figure 2.1 (left).

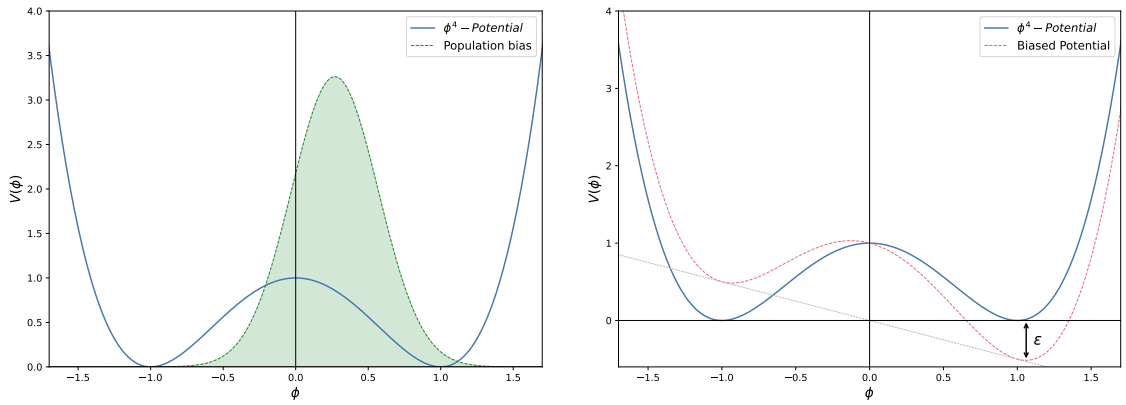

Figure 2.1: **Left:** Illustration of the *population bias*, where both vacuum states of the Higgs potential remain degenerate, but one of the states is initially more populated. **Right:** Illustration of the *potential bias*, where a linear bias term is added to the standard ϕ^4-potential from Eqn. (1.28), making one vacuum energetically favorable.

The second case is the *potential bias*. It is often modeled by adding a term that is linear in the field ϕ, but occasionally also cubic or exponential, to the potential. An example of the standard Higgs potential (1.28) with an additional bias term of the form

$$V_{\text{bias}}(\phi) = -\epsilon \frac{\phi}{\phi_0}\,, \tag{2.28}$$

is depicted in figure 2.1 (right). In this scenario, a volume pressure counteracts the surface tension of the domain walls. As the average size of the domains grows during their evolution, this volume pressure will eventually dominate over the surface tension, causing the domains of the true vacuum to rapidly expand and fill all regions in the universe. As shown in the literature [149, 181, 182], the rapid decay of the false vacuum occurs once the characteristic length L approaches a value of order $2\epsilon/\sigma$, where 2ϵ is the (small) difference in the potential energy of the minima. This type of bias is frequently explored in axion domain wall models, in which the walls would decay into axion-like particles (ALPs) that can potentially contribute to dark matter [183–185]. Importantly, however, for earlier cosmological times, bias has a negligible impact on domain wall network dynamics, and thus their evolution is well described by the VOS model or the PFM up to the time of disappearance of the walls.

3. Simulating Domain Walls

Analytical models such as the VOS model discussed in chapter 2 offer a simple framework to calculate the evolution of averaged quantities describing the large-scale dynamics of the network. While for many applications only this large-scale evolution is of interest, on smaller scales the behavior of domain walls can be complicated and often goes beyond the scope of analytical modeling*. To delve deeper into the complex dynamics of walls, field theory (FT) simulations have proven to be an indispensable tool. Unlike the infinitely thin Nambu-Goto walls that are the basis of most analytical models related to domain walls, walls in lattice simulations are extended objects that possess an internal structure. In this way, simulations allow us to study model-dependent phenomena, such as wall collision events or the creation of scalar particles in a realistic setting. Therefore, field theory simulations also enable us to probe the influence of model parameters and different potential shapes on the dynamics of walls. Moreover, they are useful for studying situations in which the thin-wall approximation breaks down, which can be the case for very light walls or regions of high curvature†. Simulations can also be used to study the interaction of domain walls with astrophysical objects or perturbations of the background metric that result in gravitational waves. Simulations of domain wall networks that feature high dynamic ranges can be used to test the predictions of analytic models such as the linear scaling regime and to calibrate the free parameters of these models. They have hence proven to be a valuable addition to analytical models and essential to get a complete picture of domain wall dynamics. The first to study the evolution of cosmic domain wall networks numerically were Press, Ryden, and Spergel (PRS) [156], who developed an algorithm that keeps walls resolvable in an expanding background. Although the simulations they performed with the limited computational resources available in 1989 are long outdated, the technique developed by them is still used in modern simulations of domain wall networks. In this chapter, we will first briefly review this so-called PRS algorithm, then we will discuss its implementation in Python. We will conclude with some detailed analysis and a comparison of different methods that have been used in the literature to extract the characteristic length scale from simulations.

*There have been attempts, however, to incorporate certain model-dependent small-scale effects into effective actions, thereby obtaining adapted equations of motion for some simple cases [186].

†Although the latter case comes with an additional challenge for lattice simulations due to a potential loss of resolution.

3.1. The PRS Equation

In order to simulate scalar fields in a cosmological background, one first has to pick a suitable coordinate system. Physical coordinates are not well-suited for this task, as the length scales relevant to probe domain wall dynamics would quickly grow beyond the size of the simulation box in this case. A better choice is to consider a comoving grid that follows the expansion of the background and to use conformal time η. This ensures that the comoving particle horizon, which is proportional to the conformal Hubble horizon $\mathcal{H}^{-1}$, scales linearly with the time steps used in the simulations, and that the relevant scales will not be pushed out of the simulation box, even in simulations with large dynamic ranges. Using $\nabla_{\mathrm{c}}^2 = a^{-2}\nabla^2$, we can re-write the equation of motion (1.14) as

$$\frac{\partial^2\phi}{\partial\eta^2} + 2\left(\frac{d\ln a}{d\ln\eta}\right)\frac{1}{\eta}\frac{\partial\phi}{\partial\eta} - \nabla_{\mathrm{c}}^2\phi = -a^2\frac{dV}{d\phi}\,, \tag{3.1}$$

where $d\ln a/d\ln\eta = \lambda/(1-\lambda)$ is a constant for any power-law evolution of the scale factor. Although this choice of coordinates allows us to track the large scale evolution of the network on cosmological time scales, it also introduces another challenge. Domain walls have a constant thickness in physical coordinates, resulting in their width decreasing with a^{-1} when using a comoving coordinate system. It has become apparent that maintaining numerical stability in lattice simulations requires the thickness of domain walls to not fall below around five grid points [156]. This requirement would necessitate huge initial wall thicknesses in the simulation boxes, which are not compatible with studying domain wall networks on larger scales. To circumvent this problem and leverage the advantages of both coordinate systems, Press, Ryden and Spergel used a numerical trick by introducing two parameters μ and ν in the equation of motion, which then becomes

$$\frac{\partial^2\phi}{\partial\eta^2} + \mu\left(\frac{d\ln a}{d\ln\eta}\right)\frac{1}{\eta}\frac{\partial\phi}{\partial\eta} - \nabla_{\mathrm{c}}^2\phi = -a^\nu\frac{dV}{d\phi}\,. \tag{3.2}$$

Although the standard equation of motion (3.1) is recovered by choosing $\mu = \nu = 2$, this parametrization is introduced in an ad-hoc manner, rather than being motivated by any underlying physical model or even derived from a Lagrangian theory. A choice of $\nu = 0$ eliminates the dependence of the right-hand side of the equation on the scale factor, which results in a constant thickness of the walls in comoving coordinates. This modification, however, introduces nonphysical behavior when it comes to the effects of Hubble damping and momentum conservation. The authors realized that this can be compensated for by choosing a modified value of $\mu = 3$. Later this formalism was generalized to universes with

N spatial dimensions. It was shown that the correct domain wall dynamics are recovered if the equation $\mu + \nu/2 = N$ is fulfilled [187]. The modified field theory equation of motion introduced by PRS has since become a standard ingredient for cosmological domain wall simulations.

3.2. Implementing the PRS Algorithm in Python

There are multiple possible numerical approaches to solve the PRS equation on a multidimensional grid, and the choice of the algorithm may influence both the speed and accuracy of the calculations. For our *Python*-based implementation, we used a finite difference scheme reminiscent of the one proposed in [156], i.e., we employed the Crank-Nicholson and staggered leapfrog methods [188] for the numerical integration of the first- and second-order time derivatives, respectively. In case of a grid with two spatial dimensions, the discretization scheme then is given by:

$$\begin{aligned} \delta &= \tfrac{3}{2}\tfrac{\triangle\eta}{\eta}\tfrac{d\ln a}{d\ln\eta} \\ \left(\nabla^2\phi\right)_{ij} &= \phi_{i+1,j} + \phi_{i-1,j} + \phi_{i,j+1} + \phi_{i,j-1} - 4\phi_{i,j} \\ \dot{\phi}_{ij}^{n+\frac{1}{2}} &= \tfrac{(1-\delta)\dot{\phi}_{ij}^{n-\frac{1}{2}} + \triangle\eta\left(\nabla^2\phi_{ij}^{n} - \partial V(\phi)/\partial\phi_{ij}^{n}\right)}{1+\delta} \\ \phi_{ij}^{n+\frac{1}{2}} &= \phi_{ij}^{n} + \triangle\eta\dot{\phi}_{ij}^{n+\frac{1}{2}}\,. \end{aligned} \tag{3.3}$$

Here, a dot denotes a derivative with respect to conformal time η and the parameter δ encodes the step size in time, as well as information about the background cosmology. The generalization of this scheme to a higher-dimensional grid can be trivially achieved by adding more spatial indices and adapting the gradient term (see below a three-dimensional example). The lattice itself obeys periodic boundary conditions, i.e., the outermost grid faces on opposite sides of the simulation box are identified with one another.

3.2.1 Performance Optimizations

To compute the evolution of a single grid point labeled by (i,j,k) (assuming a 3+1–dimensional spacetime) most of the steps of the algorithm described above depend solely on functions of the field (or its time derivative) at the same grid point. These calculations are easy to parallelize within the *NumPy* framework, so that the numerical value of the field can be computed on all grid points simultaneously. An exception to this is the calculation of the Laplacian of the field:

$$(\nabla^2\phi)_{ijk} = \phi_{i+1,j,k} + \phi_{i-1,j,k} + \phi_{i,j+1,k} + \phi_{i,j-1,k} + \phi_{i,j,k+1} + \phi_{i,j,k-1} - 6\phi_{i,j,k}\,. \tag{3.4}$$

Its value at a point (i,j,k) also depends on the values of the neighboring grid points, so that the parallelization of this operation is not obvious. A possible way of computing this gradient is looping over the spatial grid to calculate the value of the Laplacian on each grid point one after another. Unfortunately, the computation time in this case scales with N^D, where N is the number of grid points per dimension and D the number of spatial dimensions, meaning that this operation becomes extremely slow for larger grid sizes. To overcome this issue, we have tested two different methods to perform the calculation of the Laplacian in a parallel way and benchmarked them against one another.

The first method works with initializing an auxiliary matrix Θ_{ij}, $i, j = 0, \ldots, N-1$, which is zero everywhere except for the following entries: $\Theta_{ii} = -2$ and $\Theta_{ai} = \Theta_{bi} = 1$ with $a = (i+1)\%N$, $b = (i-1)\%N$, where the symbol % represents the modulo operation. In the simple case of two spatial dimensions, the Laplacian of the field ϕ can then be represented as a sum of two matrix multiplications.

$$\nabla^2\phi = \Theta\phi + (\Theta\phi^T)^T = \Theta\phi + \phi\Theta\,, \tag{3.5}$$

as $\Theta^T = \Theta$. Note that the way we initialized Θ ensures that periodic boundary conditions for our grid are respected. In the case of three spatial dimensions, we can represent the Laplacian as

$$\left(\nabla^2\phi\right)_{ilm} = \Theta_{ij}\phi_{jlm} + \Theta_{lj}\phi_{ijm} + \Theta_{mj}\phi_{ilj}\,. \tag{3.6}$$

Here, the Einstein summation convention is implicit. The implementation of this algorithm in *Python* can be achieved by using the *matmul* and *einsum* functions of *NumPy* respectively, and allows us to completely eliminate loops over the spatial grid.

The second method we tested is to compute the Laplacian at each grid point directly using the algorithm given in (3.4). Instead of using spatial loops to calculate the value of each grid point successively, however, we used the *roll* function in *NumPy*. This routine permutes the grid indices along one axis in a cyclic way, enabling us to calculate $\nabla^2\phi$ globally in a single step by representing it as a sum of suitably rotated grids.

Both methods outperform spatial loops by orders of magnitude. In a detailed comparison of computation speeds, the second method proved to be quicker than the first by a factor of about five. This might seem surprising at first glance, as the total number of operations is larger for method two, but is most likely explained by a more efficient implementation of the *roll* function compared to the *matmul* function.

Eventually, we managed to further increase the computational speed of our code significantly by making use of the *CuPy* package, which allows us to evolve the equation of motion on a GPU instead of a CPU. With these optimizations applied, we found that the major limiting factor that restricted the grid sizes for our simulations was memory requirement in the VRAM rather than computation speed. In section 3.3 we will review some algorithms that enable us to measure some important large scale quantities such as the characteristic length and the RMS velocity from simulations. These methods are based on similar numerical techniques, and their computational speed would likewise profit from the execution on the GPU. In this case, however, their computation would consume additional memory in the VRAM, therefore effectively decreasing the available resources to evolve the domain wall network. Since the extraction of network parameters only needs to be applied at a comparably low number of snapshots during the evolution, rather than at every time step, the impact of running these algorithms on the CPU instead of the GPU on the total time of the simulation is smaller. For our simulations, we therefore copy the values of the field, as well as its time derivatives, from the VRAM to the RAM of the system at every time step we want to extract network parameters. We then use the *ThreadPoolExecutor* module to parallelize this computation. This enables the GPU to continue to handle the network evolution calculations, while the CPU extracts the desired quantities in the background. These steps allow us to use the capacities of personal computers or cloud computers very efficiently.

Note that the optimizations described in this section were only gradually found within my PhD and also the hardware available to run simulations on changed within this time frame. Therefore, both the grid sizes and dynamical ranges we used in the simulations we ran for scientific purposes exhibit some significant variability.

3.2.2 Selecting Numerical Parameters

With the algorithm properly set up, the only remaining task to run domain wall network simulations is to choose the free numerical parameters and initial conditions adequately. The step sizes in time $\triangle\eta$ and space $\triangle x$ can in principle be arbitrarily chosen as long as they obey the relation $\triangle\eta \lesssim \triangle x/\sqrt{D}$. This is known as the Courant-Friedrichs-Lewy stability condition [189] and ensures the locality of interactions. In practice, a time step that is slightly smaller than the maximum step size allowed by this condition often yields better numerical stability. When performing simulations of the full cosmological evolution of domain wall networks, we mostly set the spatial grid spacing to $\triangle x = 1$ for simplicity. Smaller grid spacings may be used in situations where a higher resolution is required.

Since field theory simulations are invariably model dependent, it is necessary to specify details of the scalar potential. Here, we opt for a generic ϕ^4-potential in the form given by Eqn. (2.1) and set $\phi_0 = 1$. As mentioned previously, numerical stability of the simulation demands domain wall thickness to be at least around five lattice points, and for most of our simulations, we typically used a wall thickness of around 10-20 grid spacings. This can be translated into the condition $w_0 \gtrsim 5\triangle x$, and we then use Eqn. (2.4) to set the parameter V_0 accordingly. The values of the field ϕ were initialized with random values in $[-\phi_0, \phi_0]$, thereby modeling thermal initial conditions. Furthermore, the simulations are started at an initial time $\eta_i = \triangle\eta$ and setting $\dot{\phi}$ identically to zero on the whole grid.

Running the simulations, we observe that the initial random distribution of ϕ relaxes quickly into a state where spatial domains, associated with the two different vacua, form after the Hubble horizon grows larger than w_0. Domains smaller than the growing horizon quickly collapse and disappear, emitting bursts of scalar radiation in the last stages of collapse. This leads to space being partitioned into increasingly larger structures as time evolves. Note that since the memory requirement of simulations is proportional to N^D, grid sizes and dynamical ranges can be chosen orders of magnitudes higher when performing simulations on a 2D instead of a 3D grid, making it often a preferred option. Figure 3.1 shows a comparison of a 2D evolution of networks in the radiation dominated era (left) and the matter dominated era (right) respectively. An illustration of the energy density distribution in a three-dimensional domain wall simulation is shown in figure 3.2.

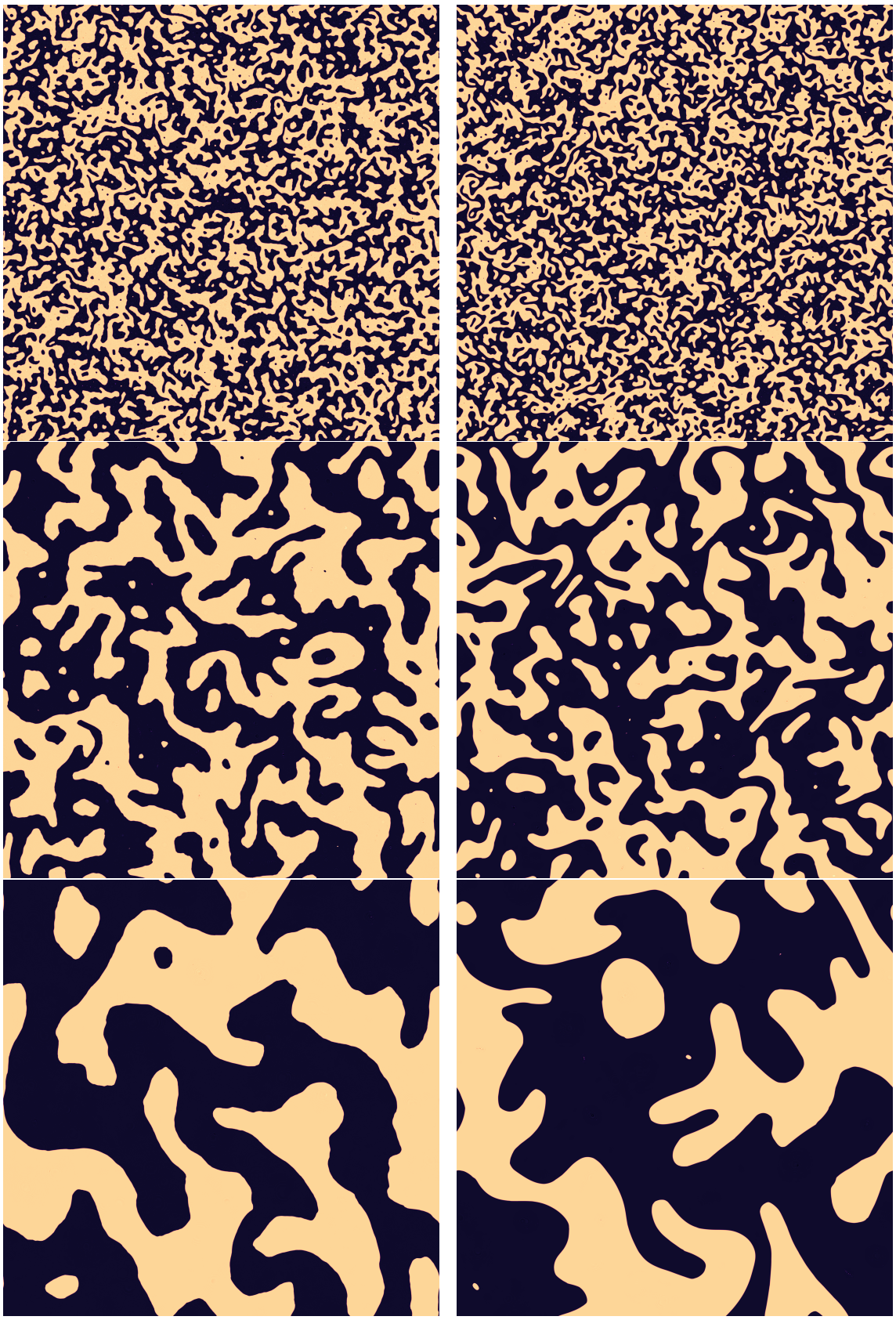

Figure 3.1: Time evolution of a domain wall network in the radiation-dominated era (left column) and in the matter-dominated era (right column) from top to bottom. Different colors represent regions in space that are in the two distinct vacuum states of the Higgs potential. The simulations were performed on a 2D grid with 24000^2 lattice points and snapshots in the same row were taken at equal conformal times. While the evolution is very similar for both background cosmologies, the edges of domains evolving in the matter era tend to be a bit smoother and scalar radiation is damped more effectively due to the faster expansion rate.

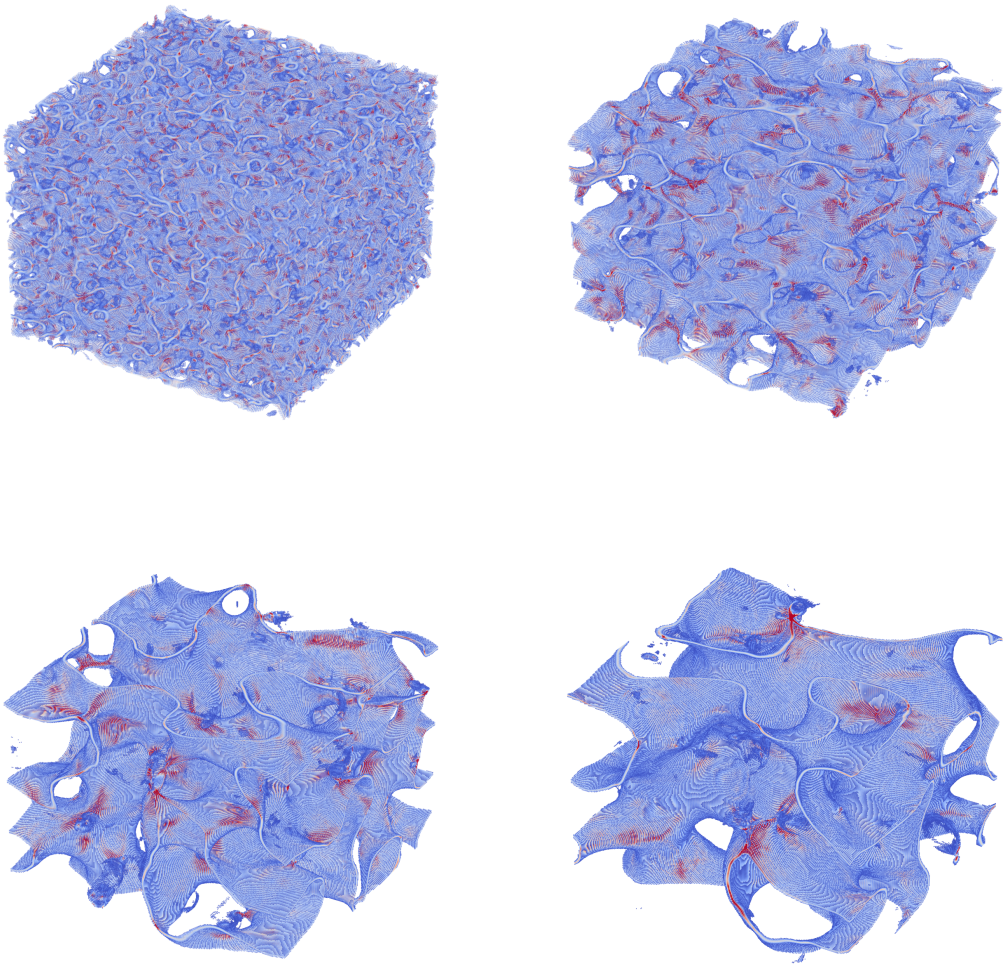

Figure 3.2: Time evolution of a domain wall network in the radiation-dominated era in three spatial dimensions. The walls were plotted by extracting the energy density distribution from a lattice with a gridsize of 820^3. Redder colors represent regions of higher energy density, corresponding to faster moving domain walls.

3.3. Measuring the Characteristic Length from Simulations

While the purely visual inspection of snapshots taken from domain wall simulations alone can often contribute to a better understanding of wall dynamics, in many situations a more quantitative analysis of the evolution of walls is desired. In this section, we will first summarize the two most commonly used methods to extract the comoving characteristic length from domain wall network simulations. Additionally, we will introduce a simplified method, which relies on counting the number of grid points that lie inside a wall. We will then perform a detailed analysis on the effects of discretization on the quantities measured by the different methods. Moreover, we will show that the quantities measured with different methods only coincide in the non-relativistic regime. For relativistic wall velocities, we can compute corrections that allow us to transform between the quantities extracted with different methods. We will show that these corrections can also be used as an independent method to measure the wall velocities, which do not rely on computing time derivatives of the field ϕ.

The first approach to extract the characteristic length was introduced by PRS in their pioneering work [156] on domain wall simulations and it does so in a purely geometrical way. The method works by scanning for links in the grid on which the field ϕ changes sign. By summing all corresponding grid faces (weighted by a correction factor that accounts for the orientation of the wall with respect to the grid), PRS were able to determine the total comoving area of domain walls within their simulation box:

$$A^{(\mathrm{PRS})} = \Delta x^2 \sum_{\mathrm{links}} \frac{|\nabla\phi|}{\sum_i |\phi_{,i}|} \delta_-^+ \,. \tag{3.7}$$

Here Δx^2 is the area of one grid face*, δ_-^+ is one for links with a sign change of ϕ and zero otherwise, $i = \{x, y\}$ in 2D and $i = \{x, y, z\}$ in 3D and $_{,i}$ denotes a partial derivative WRT this component. The comoving characteristic length can now be obtained by considering the ratio of the total volume of the simulation box and the domain wall surface area:

$$L^{(\mathrm{PRS})} = \frac{V_{\mathrm{box}}}{A^{(\mathrm{PRS})}} \,. \tag{3.8}$$

In the following, we will refer to this method to extract the characteristic length from simulations as the “PRS method”. Due to its geometrical nature, the characteristic length as defined here is closest to the interpretation of a mean distance of walls or mean curvature radius of walls in a network. However, as we have seen in section 2.2, in the context of

*As mentioned, we will assume a grid spacing of $\Delta x = 1$ if not explicitly stated differently. Still, our results can be generalized to arbitrary grid spacings in a straightforward manner.

the VOS model, the characteristic length of a network is defined in a slightly different way. Analogous to equation (2.14), the comoving characteristic length can also be measured as the ratio of the wall's rest mass per unit area and the comoving energy density [158, 176]:

$$L^{(\rho)} = \frac{\sigma_0}{\langle \rho \rangle_\epsilon} \tag{3.9}$$

In the above expression, we introduced the subscript ϵ, which indicates that in simulations the energy density is only evaluated at grid points that are defined to lie within a wall. This is done to prevent collecting contributions to the energy density from scalar radiation which would artificially decrease the measured characteristic length [159]. A grid point is counted as lying within a wall if the value of the field fulfills the "ϵ-criterion"

$$|\phi| < \epsilon \phi_0 \,, \tag{3.10}$$

with the parameter ϵ usually being chosen to lie within the range of 0.25 - 0.75. When referring to characteristic lengths extracted from simulations via Eqn. (3.9) we will from now on use the term "energy density method".

If we rewrite the static solution (2.3) for a wall moving with a constant velocity $v = \sqrt{1-\gamma^{-2}}$, the domain wall is (at $t = 0$) described by a field configuration given by

$$\phi(x, \gamma) = \phi_0 \tanh \frac{\gamma \pi}{w_0}(x - a) \,. \tag{3.11}$$

In this expression, we allow the center of the wall to be shifted by an amount a, and the reason for this will become apparent in the next section. The spatial extension to which a wall satisfies the ϵ-criterion is $\pm\kappa/2$ from the center of the wall, where κ is given by

$$\kappa = \frac{2w_0}{\pi\gamma} \operatorname{arctanh}(\epsilon) \equiv \frac{\kappa_0}{\gamma} \,. \tag{3.12}$$

Note that κ_0 is a constant for each domain wall simulation, as the parameters w_0 and ϵ are fixed in advance. For now, we will restrict ourselves to considering walls at rest ($\gamma = 1$). The case of a non-zero velocity shall be discussed in section 3.3.2.

As shown in section 2.1, the tension of a wall at rest is defined through the parameters of the potential and, for the Goldstone model, given by $\sigma_0 = \sqrt{32 V_0}\phi_0/3$. However, if we use this expression to measure the characteristic length as given in (3.9), we are introducing an error, as σ_0 contains contributions from the boundaries of the wall that extend to spatial infinity, while the energy density in the network is only measured within tighter boundaries. We can hence do better by calculating the rest mass of the wall (per unit area) within the

same boundaries in which we measure the energy density (i.e., in the region that satisfies the ϵ-criterion):

$$\sigma_0 = \int_{-\kappa_0/2}^{\kappa_0/2} \frac{2V_0}{\phi_0^2} \operatorname{sech}^4\left(\frac{\sqrt{2V_0}}{\phi_0} x\right) dx\,. \tag{3.13}$$

The integrand in this expression corresponds to the spatial distribution of the energy density derived from a static wall solution (cf. Eqn. (2.9)) and the result can be evaluated numerically.

The considerations above allow us to measure the characteristic length of walls in another, simplified and computationally cheap way. This works by counting the number of points that belong to a wall (according to the ϵ-criterion), and calculating the surface area of walls in the grid by dividing the measured volume by the wall's thickness at rest (as defined by κ_0).

$$A^{(\mathrm{count})} = \sum_{\left\{ij \,|\, \left|\phi_{ij}\right| < \epsilon\phi_0\right\}} \kappa_0^{-1}\,. \tag{3.14}$$

As before, this surface area can now be converted to a characteristic length by considering its fractional contribution to the total simulation volume:

$$L^{(\mathrm{count})} = \frac{V_{\mathrm{box}}}{A^{(\mathrm{count})}}\,. \tag{3.15}$$

This we shall refer to as the "counting method" in the following.

3.3.1 Influence of Spatial Discretization

So far, we have defined quantities like the energy density in a continuous background spacetime. In lattice simulations, however, observables can only be extracted from simulations at discrete points in space. In the following, we will discuss how this discretization of space can influence our measurements.

The Aligned Case To begin with, we will examine the case in which the planar wall from Eqn. (3.11) is parallel to the grid lines in any of the spatial dimensions of the grid. For example, this could be a planar wall that is infinitely extended in the y- and z-direction. As explained above, to measure quantities such as the energy density, we make use of the ϵ-criterion, i.e., we only consider points within a range of $\pm\kappa/2$ from the center of the wall. In Eqn. (3.11), we allowed for this center to be shifted by an amount $a \in [0, \Delta x)$ towards $x = 0$ (a shift larger than the grid spacing would lead to exactly the same situation as the

same shift modulo the grid spacing, by a re-labeling of grid points). This is illustrated in figure 3.3.

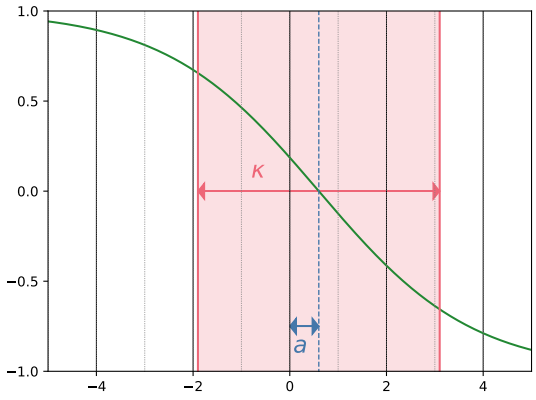

Figure 3.3: The static wall solution as given in Eqn. (3.11) for an exemplary shift of $a = 0.6$. Additionally, we marked the region that fulfills the ϵ-criterion.

Let us start by considering $a = 0$ and therefore that the wall is centered around the grid point located at $x = 0$. The solution for ϕ is an anti-symmetric function, and hence we will count as many points left of the center satisfying the ϵ-criterion as we do on the right side. Additionally, the center grid point itself will be counted, therefore in total yielding an odd integer number of grid points satisfying Eqn. (3.10)*. So far we haven't made any assumptions on the value of κ. In principle, $\kappa \leq \kappa_0$ can adopt an arbitrary positive value. To serve its purpose, however, κ_0 is usually smaller than the thickness of the wall w_0 (this is the case for all $\epsilon < \tanh(\pi/2) \approx 0.92$).

Let us now consider a shift in the position of the center of the wall. Assume a shift to the right ($a > 0$), such that the point $\lfloor \kappa/2 \rfloor + 1$ now just fulfills the ϵ-criterion. Here and in the following, $\lfloor x \rfloor$ represents the floor function, defined as the largest integer not exceeding $x \in \mathbb{R}$. If a shift that leads to a new grid point being counted on the right side of the center of the wall doesn't lead to the leftmost point dropping out, we now count an additional grid point, and therefore an even number in total. One can show that this situation can occur if

$$\left| \frac{\kappa}{2} + \lfloor -\frac{\kappa}{2} \rfloor - \lfloor \frac{\kappa}{2} \rfloor \right| - \frac{\kappa}{2} < 0 \,. \tag{3.16}$$

Solutions to (3.16) are given by $\kappa \in (2n-1, 2n)$, $n \in \mathbb{Z}$, in other words, for κ lying between an odd and the next larger even integer number. In an analogous fashion, we can again shift the center of the wall to the right, this time by an amount such that the leftmost point

*With $\Delta x = 1$, the number of measured points orthogonal to the wall (roughly) corresponds to $\kappa + 1$.

that was still counted as lying in a wall (corresponding to $\lfloor -\kappa/2 \rfloor$+1) just drops out of the interval we measure. If this shift is not sufficient to count an additional grid point on the right side, it means that we have actually dropped one point in our counting. This situation occurs if

$$\lfloor \frac{\kappa}{2} \rfloor - \lfloor -\frac{\kappa}{2} \rfloor - \kappa \geq 0\,, \tag{3.17}$$

or $\kappa \in [2n, 2n+1]$, $n \in \mathbb{Z}$. This particularly includes also the special cases $\kappa = 2n$, where an even number of grid points is counted (except for $a = 0$, in which case we count one grid point less). For $\kappa = 2n+1$ we are counting an odd number of grid points, with the exception of $a = 0.5$.

The preceding discussion demonstrates that — even in the simplest scenario of a planar wall traveling along the grid — it is impossible to select parameters in a way that allows for a continuous extraction of quantities from the simulation. Instead, there will inevitably be discontinuities in the number of points we are evaluating, thereby producing discontinuities in the measured quantities themselves.

We proceed with this analysis by evaluating the domain wall mass per unit area on a discrete grid. Recall that in the continuous case one can write the domain wall mass per unit area as an integral over the energy density, carried out perpendicular to the wall (Eqn. (3.13)). In the discrete case, the integral transforms into a sum over the energy densities measured at the grid points that contribute to the wall's tension according to the ϵ-criterion, multiplied by the lattice spacing:

$$\sigma_\Delta = \sum_{\{x_i \,|\, x_i \in \mathbb{Z} \,\wedge\, a-\kappa/2 < x_i < a+\kappa/2\}} \rho(x_i - a)\Delta x\,. \tag{3.18}$$

We can now compare the wall mass per unit area measured in the discrete case with the prediction from the continuous case as given in Eqn. (3.13). In figure 3.4 (top panel) we plotted the relative error $(\sigma_0 - \sigma_\Delta)/\sigma_0$ of σ_Δ for all possible shifts a. Note that when measuring the characteristic length in a domain wall network simulation with the energy density method (according to Eqn. (3.9)) one implicitly assumes that the energy density of a static wall integrated over a unit volume adds up to σ_0. Therefore, the relative error of σ_Δ compared to σ_0 propagates one-to-one into an error in local length measurements.

It can be seen in figure 3.4 that depending on the value of κ, the relative error can become significant. For $\kappa_0 = 3.5$, for example — a value that corresponds (via Eqn. (3.12)) to the commonly chosen parameters $w_0 = 10$, $\epsilon = 0.5$ — the relative error can get as large as $\sim \pm 10$ %. The latter is true for a wall at rest, but the mentioned value of κ_0 corresponds

to an upper limit of the measured wall extension. From Eqn. (3.12) it is manifest that with increasing wall velocity, the measured interval shrinks with increasing γ. Once κ falls under a threshold value of $\kappa = 1$ due to Lorentz contraction, a situation can occur in which the wall cannot be resolved anymore. In this case, the inferred error, however, is particularly large, as the wall moves at ultra-relativistic velocities and hence carries a lot of energy. Therefore, κ_0 can also be interpreted as an estimate of the maximum γ-factor to which walls can be resolved by the ϵ-criterion. Choosing larger values of κ_0 will reduce the amplitude of the relative error gathered on specific points on the walls, but also allow us to resolve faster moving walls.

The situation discussed above is artificial by construction, and in simulations of full domain wall networks, strictly planar walls do not naturally arise. Nevertheless, a significant portion of the walls in those networks can be aligned approximately parallel to the grid lines in either of the spatial principal directions (x,y,z), creating errors in measurement very similar to the ones described above. To obtain a more complete picture, we will briefly discuss the opposite boundary case in which the wall is not aligned with any of the grid directions.

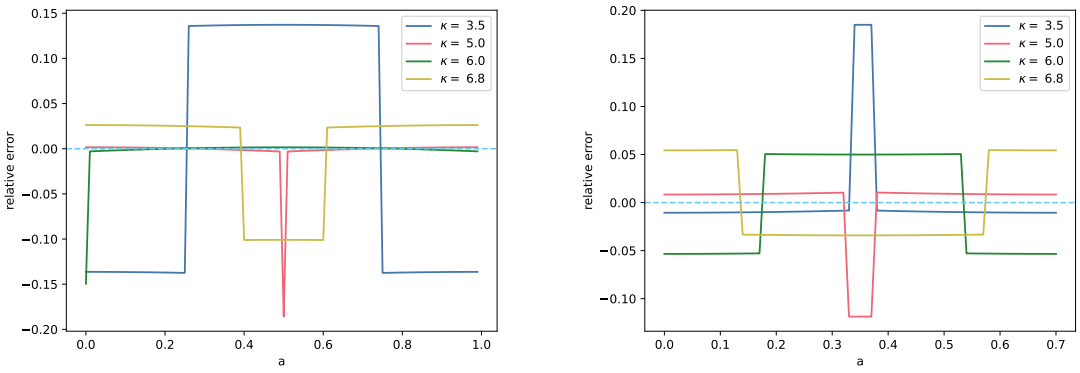

Figure 3.4: The relative error $(\sigma_0 - \sigma_\Delta)/\sigma_0$ for different positions a of the wall relative to the grid. The left plot shows the results for the case in which the wall and the grid is aligned and the right plot represents the case in which the wall is oriented diagonally with respect to the grid.

The Diagonal Case Let us assume a planar wall, tilted by an angle of 45° with respect to the grid lines, as depicted in figure 3.5 (left). We can now rotate our frame of reference so that the wall will once again be aligned with the grid lines in the y' direction in our new coordinate system (x', y') (figure 3.5, right).

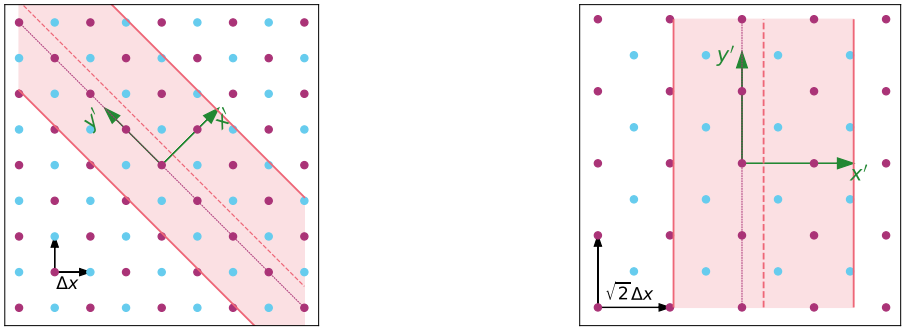

Figure 3.5: Setup for our analysis of a wall that lies diagonal in a grid. In the left plot the wall (represented by the red dashed line that marks the center as well the shaded region that marks the boundaries of the region fulfilling the ϵ-criterion) is tilted by 45° WRT the grid layers. The right plot depicts the same situation in a rotated frame of reference (x', y').

In this new frame of reference, there are alternating layers of grid points (depicted as purple and light-blue dots respectively), shifted relative to each other. The spacing of each of these layers is $\sqrt{2}\Delta x$. Unlike the aligned case, though, not all grid points that previously contributed via Eqn. (3.18) to the tension of the wall lie on a single line. However, the value of the field and its energy density are invariant under translations along y': $\rho(x' = c, y' = \sqrt{2}/2) = \rho(x' = c, y' = 0)$. This allows us to "pull down" the light-blue grid points (which are shifted towards the purple grid points by multiples of $\sqrt{2}/2$ in y' direction) onto the x'-axis. As sketched in figure 3.6, we can hence reduce the setup to an effectively one-dimensional problem similar to the one in the aligned case.

This shows in particular that all of the arguments regarding the number of grid points that are counted while shifting the wall's center (particularly Eqns. (3.16) and (3.17)) hold true for a rescaling $\kappa \to \kappa/\sqrt{2}$.

To find the tension of the wall, now all points that are integer and half-integer multiples of $\sqrt{2}$ have to be considered in (3.18). Furthermore, we have to account for the modified spacing by setting Δx to $\sqrt{2}/2$. This at first glance seems problematic, as in domain wall network simulations the algorithm does not distinguish between diagonal and aligned walls — all energy densities are equally weighted. Therefore, the measured tension appears to be too large by a factor of $\sqrt{2}$. This error is compensated though, as the distance

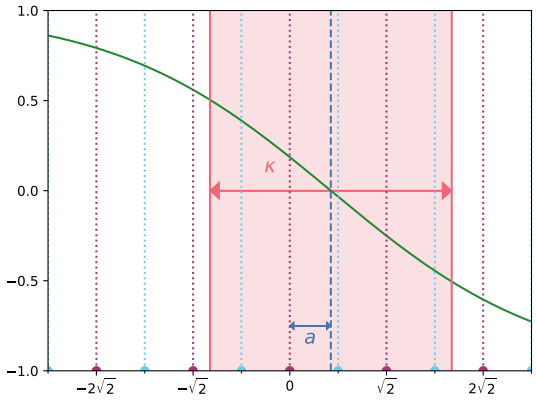

Figure 3.6: As in the coordinates (x',y') the field and its energy density are invariant under translations along y', we can pull down the intermediate layer of light-blue grid points in figure 3.5 and treat the problem as effectively one-dimensional.

of the grid layers in y' direction is stretched by the same factor, so that we end up measuring the correct mass of the wall in a given volume element. In figure 3.4 (right panel), we plotted the relative error of the (discretized) tension σ_Δ in the diagonal case (corrected by the mentioned factor of $\sqrt{2}$). Here, the relative error is a periodic function of a with a periodicity of $\sqrt{2}/2$. One can see that qualitatively the results resemble the aligned case, i.e., for certain values of a one can have large deviations from the predicted tension.

In simulations of full domain wall networks, there typically exists a large number of walls. We then expect these walls to have a random distribution of shifts a of their centers towards the grid planes. Note that even if this would not be fulfilled initially, while walls move with different velocities across the lattice, with evolving time, these shifts would eventually become randomly distributed. Hence, we can estimate the relative error Δ_{rel} in counting the energy density in a network simulation by integrating the curves plotted in figure 3.4 over all possible shifts $a \in [0, a_{\text{per}}]$, where a_{per} is the periodicity of a, which is equal to one in the aligned case and equal to $\sqrt{2}/2$ in the diagonal case. We have performed this integration numerically for a large number of different κ in the range 3 - 15. We consistently found

$$\Delta_{\text{rel}} \equiv \frac{1}{a_{\text{per}}} \int_0^{a_{\text{per}}} \left(\frac{\sigma_0 - \sigma_\Delta}{\sigma_0} \right) \left[a' \right] da' < 10^{-8} \,, \tag{3.19}$$

which is compatible with zero within numerical inaccuracies. This shows that despite collecting possibly large errors for specific points on walls in a network simulation, averaged over all shifts, those errors cancel out. In other words, as long as there is a large number of walls within the simulation box or this box is at least large enough such that the contained walls intersect with a sufficiently large number of grid layers, the errors pointed out in this

section will not propagate into the overall measurement of characteristic lengths. Although this seems to render the previous discussion largely irrelevant and academic, in the end, this result represents good news: Quantities extracted from large lattice simulations of domain wall networks do not suffer from errors induced by the effects of finite spatial resolution. An exception to this conclusion is the loss of resolution for ultra-relativistic walls that can occur when $\gamma \gtrsim \kappa_0$ that, as we discussed, may lead to an underestimation of the total energy contained in the network, yielding an overestimation of the characteristic length.

Unlike the discretization effects mentioned here, which generally do not influence the measurement of quantities in large network simulations, other factors stemming from the partially relativistic motion of walls can have a considerable impact. We will elaborate on this in the following.

3.3.2 Dependence of Measured Lengths on Wall Velocities

The spatial extension to which a wall fulfills the ϵ-criterion not only depends on the thickness of the wall and our choice of ϵ itself, but also on the wall's velocity. Let us begin by examining how this velocity dependence affects the counting method, $L^{(\mathrm{count})}$. In this case, one extracts the surface area of the domain walls by dividing the ϵ-volume of all walls by their rest-frame thickness. Consider a wall in three spatial dimensions that is locally approximately planar. In this case, we can define a set of coordinates (x, y_1, y_2), where x is perpendicular to the wall and (y_1, y_2) are coordinates on the surface S of the wall. Rewriting the measurement process in the continuum limit one gets

$$\begin{aligned} A^{(\mathrm{count})} &= \kappa_0^{-1} \int_{V_\epsilon} dx dS \\ &= \int_S \gamma(y_1, y_2)^{-1} dS\,, \end{aligned} \tag{3.20}$$

where we have used that $\kappa_0 = \gamma\kappa$. This shows that the counting method implicitly assigns a weight of γ^{-1} to each point on the wall's surface. Since domain walls only move in a direction perpendicular to their surface, this can also be interpreted as weighting each grid point in a lattice simulation individually by γ^{-1}.

Similar considerations apply to the length measurements using the energy density. The energy density in walls increases by a factor of γ as a consequence of relativistic mass increase and by an additional factor of γ as the energy in the wall is "compressed" due to Lorentz contraction in the direction perpendicular to the wall's movement. However, the latter effect cancels out when measuring the energy density in simulations, because the

ϵ-volume decreases with γ^{-1} akin to what we discussed for the counting method. We can write this in a more formal way. Let $d\mathcal{X} = \gamma dx$ such that $\rho(x) = \gamma^2 \rho_0(\mathcal{X})$, where ρ and ρ_0 are respectively the energy density profiles of a relativistic wall and a wall at rest. The volume average of the energy density is then

$$\begin{aligned} \langle \rho \rangle_\epsilon &= V_{\text{box}}^{-1} \int_{V_\epsilon} \gamma^2(y_1, y_2) \rho_0(\mathcal{X}) \gamma^{-1}(y_1, y_2) d\mathcal{X} dS \\ &= \frac{\sigma_0}{V_{\text{box}}} \int_S \gamma(y_1, y_2) dS \,. \end{aligned} \tag{3.21}$$

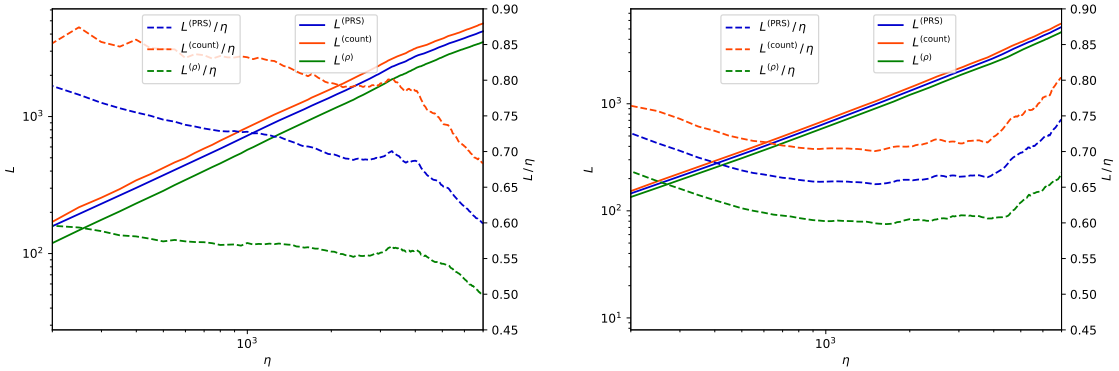

Figure 3.7: Comparison of the different methods to extract the characteristic length from a 2D network simulation on a 24000^2 grid for a slowly expanding universe with $\lambda = 0.25$ (left) and a matter-dominated evolution (right).

Note that in contrast to the examples given above, the PRS method shows no dependence on the wall's velocity, as it only counts links in which the field changes its sign. Since $\gamma \geq 1$ and the characteristic lengths measured by the counting method and energy density method are inversely proportional to $A^{(\text{count})}$ and $\langle \rho \rangle_\epsilon$, respectively, Eqns. (3.20, 3.21) suggest that $L^{(\text{count})}$ and $L^{(\rho)}$ will result in slightly higher/lower measurements than the PRS method. This is indeed what we observe, as can be seen in figure 3.7. The deviations between the different methods are most obvious in the regime of low cosmic expansion rates, in which the Hubble damping becomes small, allowing more walls to accelerate to relativistic velocities. For larger expansion rates, Hubble damping becomes more efficient, rendering the average wall velocities non-relativistic. Figure 3.8 shows the parameter $\zeta = \langle L^{(\text{i})}/\eta \rangle$ ($\langle\rangle$ here representing an average over the conformal time range where the network has entered its scaling regime) as measured with the different methods over a range of expansion rates $\lambda \in [0, 1]$.

In order to compare the different methods, we need to project them, such that they measure the same quantity. Fortunately, as demonstrated in the beginning of this section, we understand how the dependence on γ affects each of the presented methods. Hence, if

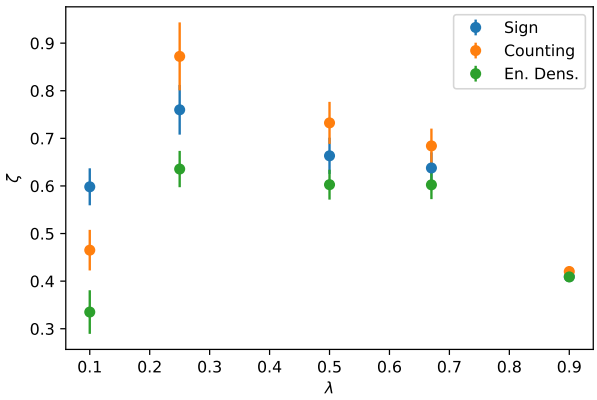

Figure 3.8: Length measured in simulations with the different methods for different values of the expansion rate λ.

we can eliminate this dependence, we would be left with a purely geometrical measure of the characteristic length, making the counting method and energy density method comparable to the results from the PRS method. To do so, we only need to measure the velocity of the domain wall at each point via Eqn. (2.8) and rewrite it in terms of γ:

$$\gamma = \sqrt{1 + \frac{\dot{\phi}^2}{2V(\phi)}} \tag{3.22}$$

Equation (3.20) shows that each grid point counted within the ϵ-volume is implicitly weighted by a factor of γ^{-1}. In order to compensate for this, instead of simply adding a contribution of κ^{-1} to the walls' surface area for each counted grid point, we have to scale the weight of this grid point by the corresponding γ-factor:

$$\begin{aligned} A_{\text{cor}}^{(\text{count})} &= \int_{V_\epsilon} \kappa_0^{-1} \gamma(y_1, y_2) dV \\ &= \kappa_0^{-1} V_\epsilon \langle \gamma \rangle_\epsilon \,. \end{aligned} \tag{3.23}$$

Hence, the correction factor for the counting method is simply a volume-average of the γ-factor of the walls:

$$L_{\text{cor}}^{(\text{count})} = \frac{L^{(\text{count})}}{\langle \gamma \rangle_\epsilon} \,. \tag{3.24}$$

In the case of $L^{(\rho)}$, on the other hand, each grid point is weighted by a different factor (corresponding to the energy density at this point). Accordingly, we cannot separate the velocity dependence in the integral when computing the volume average of ρ in simulations. To make the measurement of $\langle \rho \rangle_\epsilon$ independent of γ, we instead have to divide the energy density we measure by the corresponding Lorentz factor at each point and average over the resulting quantity. The corrected version of the length measured using

the energy density method hence reads:

$$L_{\mathrm{cor}}^{(\rho)} = \frac{\sigma_0}{\langle \rho / \gamma \rangle_\epsilon} \,. \tag{3.25}$$

Figure 3.9 displays the corrected versions of the characteristic lengths, extracted from the same network simulation as in figure 3.7. This confirms that indeed, using the new definitions, all three methods to extract the characteristic length agree well and represent a purely geometrical distance between walls. From this figure, it can be seen that in the

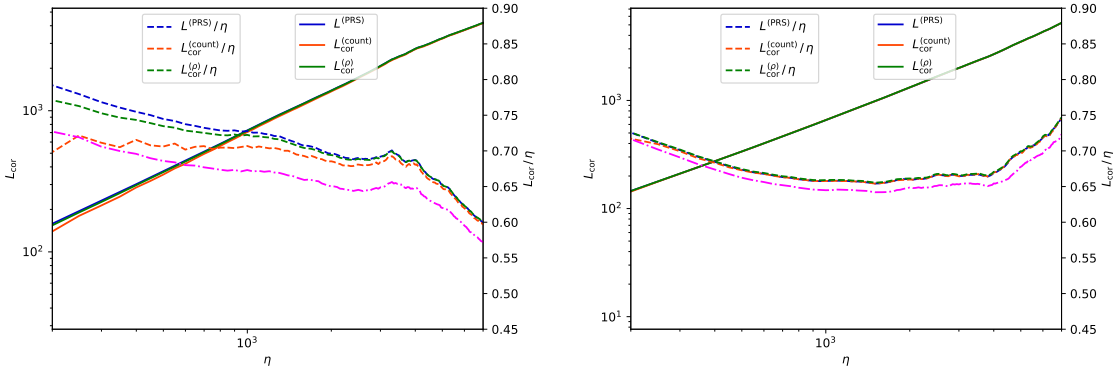

Figure 3.9: The characteristic lengths for the same domain wall network simulations as in figure 3.7, however, this time corrected for the γ-dependence of the different methods. Additionally, the dash-dotted magenta line line shows the approximated correction of the energy density method as given in Eqn. (3.27).

case of a matter dominated evolution, the measurements of the characteristic length using the corrected versions of the different methods are basically indistinguishable from each other. Also, in the case of a slow expansion rate of $\lambda = 0.25$ the corrections for the γ-dependency lead to consistent measurements of the characteristic length. However, in this case, the agreement between the methods, especially in the early stages of the evolution, is not perfect. In fact, here the PRS method measures the largest characteristic length, while the counting and the energy density method result in slightly lower values. Towards later stages of the simulation, the results then converge. This can likely be explained by large amounts of scalar radiation, which is hardly dampened for universes with small expansion rates and predominantly present in the earlier stages of evolution, during which the number of domains undergoing their final stages of collapse is higher. While the PRS method is largely unaffected by this scalar radiation, both the counting and the energy density method can falsely pick up contributions from this radiation. This assumption is corroborated by the fact that, as further tests showed, the difference measured between the methods seems to decrease when picking smaller values of ϵ.

At last, we want to emphasize that none of the methods introduced within this section measures a wrong value of the characteristic length. Instead, they are simply defined in a different way. While the PRS method might be the go-to method if one is interested in a purely geometrical quantity, the energy density method measures the characteristic length analogue to its definition in the VOS model, and is therefore particularly useful to calibrate the free parameters of the latter. Nevertheless, in the literature this distinction is often not made and particularly the PRS and the energy density method are used synonymously for measuring L. To our knowledge, the relation between those methods has not been studied in detail before.

3.3.3 Velocity From Lengths

In the previous section, we have shown that — corrected for the corresponding dependency on γ — all presented methods measure a truly geometrical quantity, as the PRS method does "out of the box". We now want to show that we can use this property to obtain a novel measurement for the average velocity of walls (in terms of γ) in a network simulation, without explicitly measuring their velocity. This can be done by imposing that the geometrical lengths we measure with the different methods agree in all cases:

$$L^{(\mathrm{PRS})} \stackrel{!}{=} L^{(\rho)}_{\mathrm{cor}} \stackrel{!}{=} L^{(\mathrm{count})}_{\mathrm{cor}} \,. \tag{3.26}$$

As we discussed, the γ-dependence of the energy density method cannot strictly be separated when computing the volume average of ρ. Depending on the velocity dispersion of the walls in the network, pulling γ out of the integral will still be a good approximation. This allows us to write

$$L^{(\rho)}_{\mathrm{cor}} \approx \langle \gamma \rangle_{\epsilon} L^{(\rho)} \tag{3.27}$$

Taking together equations (3.22), (3.24), (3.26) and (3.27) we obtain

$$< \gamma >_{\epsilon} = \left\langle \sqrt{1 + \frac{\dot{\phi}^2}{2V(\phi)}} \right\rangle_{\epsilon} = \frac{L^{(\mathrm{count})}}{L^{(\mathrm{PRS})}} \approx \frac{L^{(\mathrm{PRS})}}{L^{(\rho)}} \,. \tag{3.28}$$

Note that the "standard" measurement of velocity (corresponding to the first equality), despite using the ϵ-criterion, is not affected by the discretization effects discussed in 3.3.1. This is due to the fact that, in contrast to the length measurements, no initial assumptions on the walls' thicknesses or tensions have to be made. Particularly interesting in Eqn. (3.28) is the second equality, which allows us to extract an averaged domain wall velocity only by comparing the PRS method with the result from the counting method.

Both quantities solely require knowledge of the values of the field ϕ itself, but not of its time derivatives $\dot{\phi}$. Thus, we can use this method, for example, to reconstruct the walls' average velocity from simulations where no time derivatives of the field have been stored. In simulations where a local measurement of the walls' velocities is not required, this can potentially save disk space and memory. An example for the extraction of the averaged from a network simulation using all three methods introduced in Eqn. (3.28) is plotted in figure 3.10. Again for a matter-dominated background evolution, the standard method and

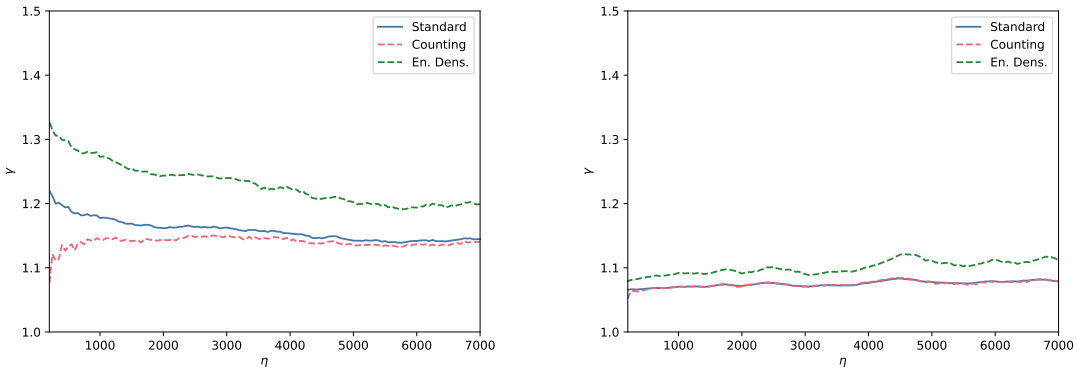

Figure 3.10: The γ-factor of walls (averaged over the volume defined by the ϵ-criterion) as measured from the same simulations used in the figures 3.7 and 3.9 using the different methods introduced in Eqn. (3.28) for $\lambda = 0.25$ (left) and $\lambda = 2/3$ (right). The standard method and the counting method, which measures $L^{(\mathrm{count})}/L^{(\mathrm{PRS})}$ agree very well, particularly in the case of a matter-dominated background, while there are significant deviations for the energy density method, due to (3.27) being a rough approximation.

the counting method, which measures $L^{(\mathrm{count})}/L^{(\mathrm{PRS})}$ agree to astonishing precision while for smaller expansion rates there are some discrepancies, likely explained by scalar radiation. On the other hand, the results provided by the energy density method are not that accurate, which can be explained by the fact that Eqn. (3.27) is only an approximation.

4. Exploring the Parameter-Free Model

This chapter will be dedicated to numerical and analytical investigations of the parameter-free model, which we reviewed in section 2.3. This model can be used to estimate the values of the scaling parameters ζ and $\bar{v}$ of domain wall networks from first principles. Note that within this chapter we will also refer to $\bar{v}$ as σ_v. Both notations represent the RMS velocity of walls within a network. Here, to allow for a better integration into analytical models, which, for instance, can be used to predict observational signatures of domain wall networks, we will derive simple analytical approximations to the PFM. We will moreover point out some interesting parallels between the PFM and the parametric VOS model in the non-relativistic limit in section 4.2. In section 4.3, we will then probe the PFM with simulations in order to gain a better understanding of the discrepancies between the two models in the relativistic regime.

4.1. An Analytical Approximation to the Parameter-Free Model

The present, as well as the following section, summarize the analytical work we have done building upon the parameter-free model, which has largely been published in [2]. Here, we shall derive analytical approximations for ζ and σ_v in two limiting cases: $\lambda \to 1^-$ and $\lambda = 0$, where as before λ represents the power-law exponent of the cosmic expansion rate. For λ sufficiently close to unity, the domain walls are almost always non-relativistic, making it possible to perform an analytical estimation of both parameters. On the other hand, the absence of Hubble damping in the $\lambda = 0$ case also allows for an analytical determination of both ζ and σ_v.

4.1.1 The $\lambda \to 1^-$ Case

Consider the evolution of domain walls in the non-relativistic regime. We want to derive an approximate solution of Eqn. (2.22), valid for $v \ll 1$. First we rewrite the EOMs for a power-law evolution of the scale factor and in terms of the reduced comoving radius $\tilde{q} = q/q_i$. We obtain:

$$\frac{d\tilde{q}}{d\tau} = -v \quad \text{and} \quad \frac{dv}{d\tau} + \gamma^{-2}\left[\frac{3\lambda}{1-\lambda}\frac{v}{\tau} - \frac{s}{\tilde{q}}\right] = 0\,. \tag{4.1}$$

Let us choose an ansatz for $\tilde{q}$ of the form

$$\tilde{q} = \sqrt{1 - \left(\frac{\tau}{\tau_\star}\right)^2}, \tag{4.2}$$

which satisfies $\tilde{q}(0) = 1$ and $\tilde{q}(\tau_\star) = 0$ for a finite collapse time $\tau_\star$. The derivative WRT τ yields an equation for v:

$$\gamma^{\frac{1}{s}} v = \frac{1}{\tau_\star^2} \frac{\tau}{\tilde{q}}\,. \tag{4.3}$$

Notice that $v \in [0,1)$ while the RHS of Eqn. (4.3) diverges for $\tau \to \tau_\star$. Despite the factor of $\gamma^{1/s}$ being very close to unity in the non-relativistic regime, we included it here to guarantee Eqn. 4.3 is well defined (even outside the strictly non-relativistic limit). The exponent $1/s$ moreover ensures that $E \propto \tilde{q}^s \gamma$ tends to a non-vanishing constant in the $\tau \to \tau_\star$ limit. By calculating the derivative of the first Eqn. in (4.1) WRT τ we obtain a second order differential equation for $\tilde{q}$. Inserting the ansatz (4.2) and evaluating the resulting equation in the beginning of the collapse (such that $\tau \to 0$, $\tilde{q} \to 1$, $\gamma \to 1$) allows us to find an explicit expression for $\tau_\star$:

$$\tau_\star = \sqrt{\frac{2\lambda + 1}{s(1-\lambda)}}\,. \tag{4.4}$$

This value of $\tau_\star$ is strongly dependent on λ: $\tau_\star \propto (1-\lambda)^{-1/2}$ for $\lambda \sim 1$, becoming infinite in the $\lambda \to 1^-$ limit. It also shows some dependence on whether the domain walls are assumed to be cylindrical or spherical, being smaller by a factor of $\sqrt{2}$ in the latter case.

Let us define τ_+ as the value of τ for which $v\gamma^{1/s} = 1$. One can show that, according to our approximation,

$$\frac{\Delta\tau}{\tau_\star} = \frac{\tau_\star - \tau_+}{\tau_\star} \sim \frac{1}{1+\tau_\star^2}\,. \tag{4.5}$$

This essentially means that, for λ sufficiently close to unity, the fraction of the conformal lifetime of the domain walls in which they are relativistic can be made arbitrarily close to zero ($\Delta\tau \sim \tau_\star^{-1} \propto \sqrt{1-\lambda}$ for λ close to unity). This enables us to roughly estimate the contribution to the integrals given in Eqns. (2.26) and (2.27) coming from the relativistic regime. In the late stages of collapse $v \sim 1$, which implies, according to Eqn. (4.3), that both $\tilde{q}^s\gamma$ and $v^2\tilde{q}^s\gamma$ are approximately equal to $\tau^s\tau_\star^{-2s} \sim \tau_\star^{-s}$ in this regime for λ sufficiently close to unity. Evaluating the aforementioned integrals in the last stages of collapse (i.e., between τ_+ and $\tau_\star$), we find that the relativistic contribution is of order $\Delta\tau\,\tau_\star^{-s} \sim \tau_\star^{-1-s} \propto (1-\lambda)^{(1+s)/2}$ and is thus expected to become negligible in the $\lambda \to 1^-$ limit. Hence, in our first approximation (which we shall refer to as A1) we shall simply neglect the factors of γ in the computation of both ζ and σ_v.

Neglecting such factors, the parameter ζ may now be estimated from Eqn. (2.26):

$$\zeta = \frac{1}{\beta\tau_\star f_1(s)} = \frac{C(s)}{\beta}\sqrt{\frac{1-\lambda}{2\lambda+1}}\,, \tag{4.6}$$

where

$$f_1(s) = \frac{\sqrt{\pi}\Gamma(\frac{s}{2}+1)}{2\Gamma(\frac{s+3}{2})}\,. \tag{4.7}$$

and

$$C(1) = \frac{4}{\pi}\,, \qquad C(2) = \frac{3}{\sqrt{2}}\,, \tag{4.8}$$

for cylindrical and spherical domain walls, respectively. The value of β, corresponding to a fixed ζ, is different for cylindrical and spherical domain walls. In fact

$$\frac{\beta_{\rm spherical}}{\beta_{\rm cylindrical}} = \frac{C(2)}{C(1)} = \frac{3\pi\sqrt{2}}{8} \sim 1.67 \tag{4.9}$$

The root mean squared velocity of the domain walls, computed using Eqns. (2.27), (4.3), (4.2) and (4.4) and neglecting the factors of γ, is equal to

$$\sigma_v^2 = \frac{1}{\tau_\star^2}\frac{f_2(s)}{f_1(s)} = \frac{1}{\tau_\star^2}\frac{\Gamma(\frac{s}{2})}{2\Gamma(\frac{s}{2}+1)} = \frac{1}{s\tau_\star^2} = \frac{(1-\lambda)}{2\lambda+1}\,, \tag{4.10}$$

with

$$f_2(s) = \int_0^1 x^2(1-x^2)^{s/2-1}dx = \frac{\sqrt{\pi}\Gamma(\frac{s}{2})}{4\Gamma(\frac{s+3}{2})}\,. \tag{4.11}$$

It is also possible to compute ζ and σ_v using Eqns. (2.26) and (2.27) considering a second approximation where the factors of γ are no longer neglected (including the factor of $\gamma^{1/s}$ in Eqn. (4.3)). Although there are no simple analytical expressions for ζ and σ_v in this case, the main difference is that the degeneracy between the results obtained considering cylindrical ($s = 1$) and spherical ($s = 2$) domain walls is broken. Since this is an important feature of the parameter-free VOS model, we shall come back to this approximation — which we shall refer to as A2 — in the following section.

It is interesting to note that in the non-relativistic regime the evolution is dominated by curvature. Therefore, for λ sufficiently close to unity, the first term in the velocity evolution equation (given in Eqn. (4.1)) may be neglected in the non-relativistic regime. Hence, for $s = 1$

$$v = \frac{\eta}{q}\frac{1-\lambda}{3\lambda}\,, \tag{4.12}$$

to an excellent approximation, throughout almost the whole evolution of the domain walls. Although Eqn. (4.12) describes the two-dimensional dynamics of the circular transversal cross section of a cylindrical domain wall, it may be easily generalized to account for a

transversal cross section with an arbitrary shape:

$$v = \kappa\eta\frac{1-\lambda}{3\lambda}\,. \tag{4.13}$$

Here, κ represents the corresponding comoving curvature at each point. The evolution of the cross-sectional transverse comoving area $\mathcal{A}$ of each domain wall with the conformal time η is then given by

$$\dot{\mathcal{A}} = -\oint v dl = -\frac{1-\lambda}{3\lambda}\eta\int \kappa dl = -2\pi\frac{1-\lambda}{3\lambda}\eta\,, \tag{4.14}$$

independently of the shape of the cross-sectional transverse area. Here, dl is a comoving infinitesimal arc length. Equation (4.14) represents the particular case of von Neumann's law* [190–192] where the number of domain edges is equal to zero. The solution of Eqn. (4.14) may be written as

$$\mathcal{A} = \mathcal{A}_{\rm i} - \pi\frac{1-\lambda}{3\lambda}\eta^2\,, \tag{4.15}$$

where $\mathcal{A}_{\rm i}$ is the initial cross-sectional transverse comoving area $\mathcal{A}$ of the domain wall. This result implies that, for λ sufficiently close to unity, the evolution of the area enclosed by a two-dimensional domain is essentially independent of its shape.

If, as happens in the $s = 2$ case, both the principal curvatures of the domain walls are nonzero, the evolution of the comoving volume V enclosed by each domain wall with the conformal time η is given by [193]

$$\dot{V} = -\oint v dA = -\eta\frac{1-\lambda}{3\lambda}\int \mathcal{K} dA = -2\pi\mathcal{L}\,, \tag{4.16}$$

where dA and $\mathcal{K}$ are respectively an infinitesimal surface element and the mean comoving curvature of the domain wall at each point, and $\mathcal{L}$ is the comoving mean width of the comoving volume enclosed by the domain wall. For a fixed initial comoving volume $V_{\rm i}$, $\mathcal{L}$ generally depends on the domain wall shape, which implies that the evolution of V is in general not the same for domain walls with the same $V_{\rm i}$ but different shapes.

*Von Neumann's law was originally formulated to describe the evolution of cellular structures —– such as soap froths — and relates the rate of change of a cell's area A to its number of edges n. It can be written as $\dot{A} = k(n-6)$, where k is a constant.

4.1.2 The $\lambda = 0$ Case

In the $\lambda = 0$ case, the scale factor a is constant and non-vanishing — we shall take $a = 1$, so that the physical and conformal times coincide. Also, equation (4.1) now implies that $\tilde{q}^s\gamma = 1$ or, equivalently, that

$$\tilde{q} = (1 - v^2)^{1/(2s)} \,. \tag{4.17}$$

For cylindrical domain walls ($s = 1$) one has

$$\tilde{q} = (1 - v^2)^{1/2} \,. \tag{4.18}$$

Substituting this into Eqn. (2.26) one finds that

$$\zeta = \frac{1}{\beta\tau_\star} \,. \tag{4.19}$$

Therefore, the solution of Eqn. (4.1) is given by

$$\tilde{q} = \cos\tau \,, \qquad v = \sin\tau \,, \tag{4.20}$$

where we have assumed that $\tau = 0$ when $\tilde{q} = 1$ and $v = 0$. The collapse then occurs for

$$\tau = \tau_\star = \frac{\pi}{2} \sim 1.57 \,, \tag{4.21}$$

when $\tilde{q} = 0, v = 1$ and $\gamma = \infty$. It is then possible to show, using Eqns. (2.26), (2.27), (4.19), (4.20) and (4.21), that

$$\zeta = \frac{2}{\pi\beta} \,, \qquad \sigma_v = \frac{\sqrt{2}}{2} \sim 0.71 \,. \tag{4.22}$$

For spherical domain walls ($s = 2$), the solution of Eqn. (4.1) is given by

$$\tilde{q} = (1 - v^2)^{\frac{1}{4}} \,, \qquad v = \sin\Big(2\,\mathrm{am}\,(\tau\,|\,2)\Big) \,, \tag{4.23}$$

where $\mathrm{am}\,(x\,|\,m)$ is the Jacobi amplitude function, and we have again assumed that $\tau = 0$ when $\tilde{q} = 1$ and $v = 0$. In this case, the collapse occurs for

$$\tau = \tau_\star = F\left(\frac{\pi}{4}\,\middle|\,2\right) \sim 1.31 \,, \tag{4.24}$$

again when $\tilde{q} = 0$, $v = 1$ and $\gamma = \infty$. Here $F(x\,|\,m)$ is the elliptic integral of the first kind. Then, using Eqns. (2.26), (2.27), (4.23) and (4.24), one can show that

$$\zeta = \frac{1}{\beta F(\pi/4\,|\,2)} \,, \qquad \sigma_v = \sqrt{\frac{2}{3}} \sim 0.82 \,. \tag{4.25}$$

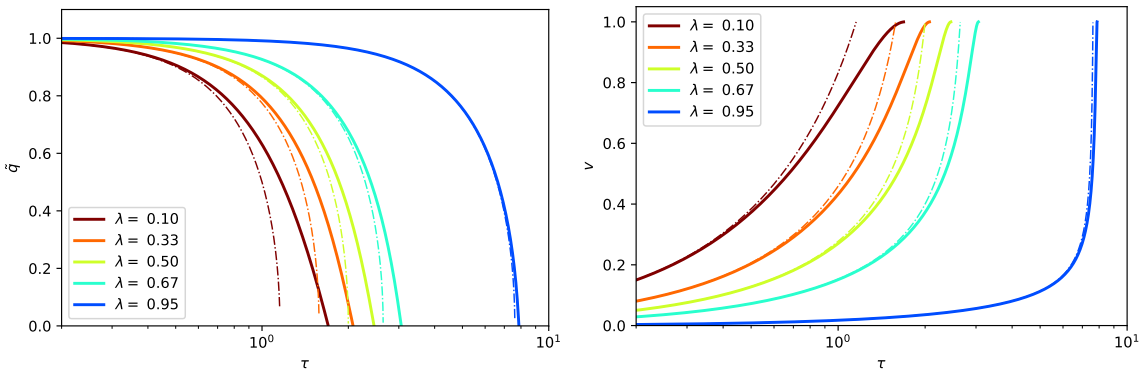

Figure 4.1: Collapse of cylindrical domain walls shown in terms of their reduced radius $\tilde{q}$ (left panel) and velocity v (right panel) in universes with different expansion rates (parameterized by λ). The solid lines correspond to the numerical solution of the Nambu-Goto equations of motion while the dash-dotted lines represent the approximation given in Eqns. (4.3), (4.2) and (4.4). Notice the excellent agreement between the analytical and numerical results, especially for λ close to unity or low values of τ.

4.1.3 Fitting the Scaling Predictions of the Parameter-Free VOS Model

In figure 4.1 we show the evolution of the reduced radius $\tilde{q}$ (left panel) and velocity v (right panel) of cylindrical domain walls in universes with different expansion rates, parameterized by λ. The solid line represents the numerical solution obtained using the Nambu-Goto equations of motion while the dash-dotted line represents the approximation given in Eqns. (4.3), (4.2) and (4.4). Figure 4.1 shows that, independently of the value of λ, the agreement between this approximation and the numerical solution is always excellent for sufficiently low values of τ, in a regime where the domain walls are still non-relativistic. Also, for values of λ close to unity, this excellent agreement spans almost the full conformal lifetime of the domain walls, since, as shown in the previous section, in this limit they only become relativistic extremely close to $\tau = \tau_\star$. We have verified that qualitatively similar results are obtained in the case of spherical domain walls. In figure 4.2 we compare the value of the domain wall lifetime, parameterized by $\tau_\star$, calculated by solving numerically the Nambu-Goto equations of motion (solid lines) with the prediction of the analytical approximation given in (4.4) (dashed lines). The blue and orange lines display the results obtained for cylindrical and spherical domain walls, respectively, while the blue and orange circles represent the corresponding exact solutions for $\lambda = 0$. Figure 4.2 shows that there is an excellent agreement between the analytical approximation and the numerical solution for $\lambda \gtrsim 0.9$. On the other hand, for smaller values of λ the approximation slightly underestimates the value of $\tau_\star$.

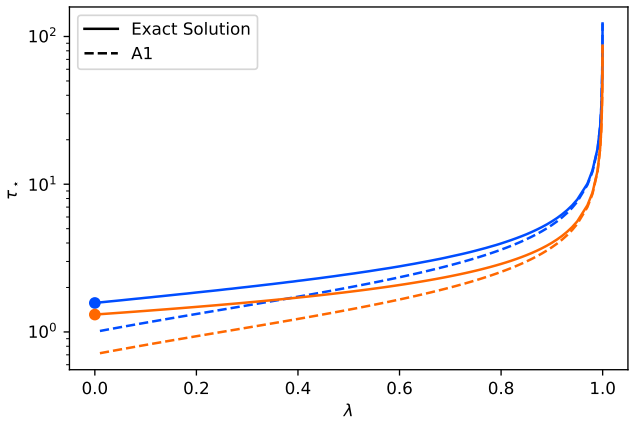

Figure 4.2: Comparison between the domain wall conformal lifetime, $\tau_\star$, obtained by solving numerically the Nambu-Goto equations of motion (solid lines) and the analytic approximation given in (4.4) (dashed lines). The blue and orange lines represent the results obtained considering cylindrical and spherical domain walls, respectively. Additionally, the exact solution in the $\lambda = 0$ case is represented by the blue and orange circles. Notice the excellent agreement between the analytical and numerical results for $\lambda \gtrsim 0.9$.

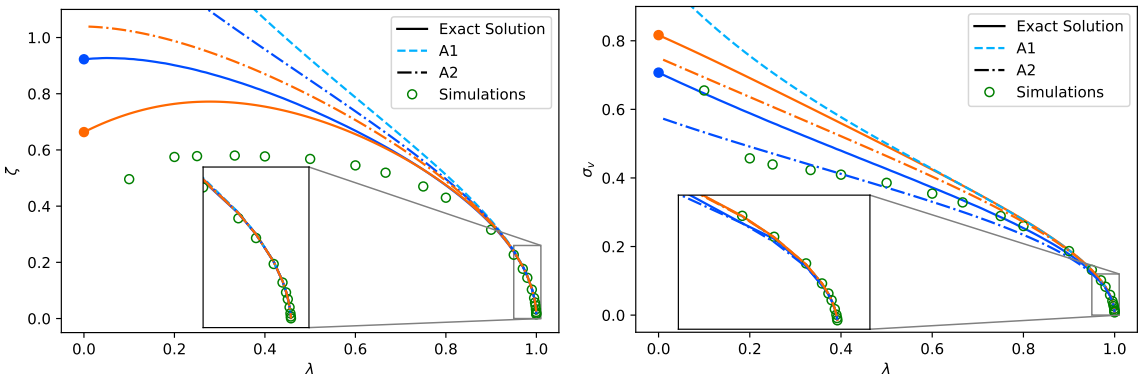

Figure 4.3: Summary of the different results obtained for ζ (left panel) and σ_v (right panel). The solid lines represent the prediction of the parameter-free VOS model, which has an exact analytic solution for $\lambda = 0$ (represented by the filled dots). The dashed and dash-dotted lines represent approximations A1 and A2, respectively. The unfilled dots show the results of field-theory simulations [159]. Notice the excellent agreement for $\lambda \gtrsim 0.9$ and that the geometrical degeneracy of the approximation A1 (blue dashed line) is broken in the approximation A2 (dashed blue and orange lines, respectively, for cylindrical and spherical domain walls).

Figure 4.3 summarizes the different results obtained for ζ (left panel) and σ_v (right panel). The solid lines show the (numerically evaluated) prediction of the parameter-free VOS model for cylindrical and spherical domain walls (in blue and orange, respectively), which has an exact analytic solution for $\lambda = 0$ (represented by the blue and orange circles). The dashed and dash-dotted lines represent, respectively, the approximations A1 and A2 discussed in the previous section. Here, we have taken $C/\beta = 1.85$, thus requiring the model to reproduce the value of ζ obtained using field theory simulations for $\lambda = 0.9998$ [175].

Figure 4.3 shows that both approximations do an excellent job for $\lambda \gtrsim 0.8$, but deviate more significantly from the model prediction for smaller values of λ. Also notice that, while approximation A1 predicts the same values of ζ and σ_v for both cylindrical and spherical domain wall configurations, the degeneracy between these two different geometries is broken by approximation A2. This is indeed a property shared by the exact solutions, thus showing that the geometry of the domain walls plays a crucial role for small values of λ in which the relativistic regime of the domain wall evolution lasts longer.

The unfilled circles in figure 4.3 represent the values of ζ and σ_v measured in field-theory numerical simulations [159]. Notice the excellent agreement for $\lambda \gtrsim 0.9$ between the predictions of the PFM and the simulation results (see also Table 4.1). For smaller values of λ there is still good qualitative agreement, but significant discrepancies occur, which we aim to investigate closer in section 4.3.

The analytical results obtained in the present paper can be used to construct an accurate fit to the scaling predictions of the parameter-free VOS model for ζ and σ_v over the whole range of λ ($\lambda \in [0,1[$) for which a linear scaling solution with cosmic time is possible in an expanding homogeneous and isotropic FLRW universe. We shall consider a fit of the form

$$\mathcal{K}(\lambda, s) = (1-\lambda)^n \mathcal{K}_{\lambda=0}(s) + \lambda^m \mathcal{K}_{\mathrm{A1}}(s)\,, \tag{4.26}$$

where $\mathcal{K}$ represents either ζ or σ_v, $\mathcal{K}_{\lambda=0}(s)$ is the exact solution for $\mathcal{K}$ in the $\lambda = 0$ case, $\mathcal{K}_{\mathrm{A1}}(s)$ is the first analytical approximation $A1$ for $\mathcal{K}$ as given in Eqns. (4.6) and (4.10), $s = 1, 2$, and n, m are the fit parameters given in Table 4.2. We have verified that the maximum relative error of the fits for both ζ and σ_v is of the order of 1%, allowing us to provide a closed formula to the scaling values of ζ and σ_v predicted by the parameter-free VOS model.

λ	ζ		σ_v	
	A1	Simulations	A1	Simulations
0.97	0.186	0.177	0.101	0.102
0.98	0.152	0.145	0.082	0.083
0.99	0.107	0.103	0.058	0.059
0.995	0.075	0.073	0.041	0.041
0.997	0.058	0.057	0.032	0.032
0.998	0.048	0.046	0.026	0.026
0.999	0.034	0.033	0.018	0.018
0.9995	0.024	0.023	0.013	0.013
0.9997	0.018	0.018	0.010	0.010
0.9998	0.015	0.015	0.008	0.008

Table 4.1: The values of ζ and σ_v obtained using approximation A1 (which follow very closely the results of the parameter-free VOS model for $s = 1$ and $s = 2$) and the results of field theory numerical simulations for discrete values of λ between 0.97 and 0.9998. Notice the exceptional agreement between approximation A1 (and consequently the predictions of the parameter-free VOS model) and the results of field theory numerical simulations in the $\lambda \to 1^-$ limit.

$(n,\, m)$	cylindrical	spherical
ζ	(1.6371, 1.0413)	(1.4044, 0.9975)
σ_v	(1.7947, 1.1686)	(1.6179, 1.1346)

Table 4.2: Parameters (n, m) of the fits for ζ and σ_v for $s = 1$ (cylindrical domain walls) and $s = 2$ (spherical domain walls).

4.2. Comparison to the VOS Model

In this section, we will consider the non-relativistic limit of the original (parametric) VOS model, which we reviewed in section 2.2, for the cosmological evolution of domain wall networks. This model provides a quantitative thermodynamical description of their cosmological evolution by following the evolution of L and σ_v as given in Eqns. (2.16, 2.17)[172, 174, 191]. In what follows, we shall neglect the effects of friction in the evolution of the network (i.e., we set $l_f = +\infty$).

The VOS model quantifies the efficiency of the energy loss associated with the collapse of domain walls through the parameter $\tilde{c}$. This energy loss results in a contribution to the evolution of the average domain wall energy density (through the last term in Eqn. (2.16)) which, analogously to the cosmic strings' case [194], is usually assumed to be of the form

$$\left.\frac{d\rho_{\rm dw}}{dt}\right|_{\rm loss} = \tilde{c}\,\sigma_v \frac{\rho_{\rm dw}}{L}\,. \tag{4.27}$$

Conservatively, we may expect the rate of variation of energy not associated to the expansion of the cosmological background to be such that

$$\left.\frac{d\rho_{\rm dw}}{dt}\right|_{\rm loss} = \tilde{c}\sigma_v\frac{\rho_{\rm dw}}{L} \lesssim \frac{\rho_{\rm dw}}{\Delta t}\,, \tag{4.28}$$

where Δt is the physical time required for a domain wall to travel across a comoving distance of L/a. We should then have that

$$\tilde{c} \lesssim \frac{L}{\sigma_v \Delta t}\,. \tag{4.29}$$

We may see from Eqns. (2.19) that in the non-relativistic regime, with $\lambda \to 1^-$, this model then predicts that $\xi \to \infty$ and $\sigma_v \to 0$. This necessarily means that the energy loss term in Eqn. (4.27) is, given its dependence on L and σ_v, irrelevant in this limit. In what follows, we will further show that we necessarily have that $\tilde{c} \to 0$ in the non-relativistic limit and that, as a result, the importance of this energy loss term decays significantly faster than Eqn. (4.27) seems to indicate as $\lambda \to 1^-$. Notice that

$$\zeta = \frac{L}{a\eta} = (1-\lambda)\xi = \sqrt{\frac{k_w(k_w+\tilde{c})(1-\lambda)}{3\lambda}} \to 0 \tag{4.30}$$

in the same limit (here we have taken into account that $\eta = t/[(1-\lambda)a]$).

The time Δt a domain wall takes to transverse a comoving distance of L/a may be estimated as

$$\sigma_v \int_t^{t+\Delta t} \frac{dt}{a} = \frac{L}{a} = \frac{\xi t}{a}\,, \tag{4.31}$$

and hence it is given approximately by

$$\Delta t = \left(\left[\frac{\xi}{\sigma_v}(1-\lambda)+1\right]^{1/(1-\lambda)} - 1\right) t\,. \tag{4.32}$$

For $\lambda = 0$, Eqn. (4.32) yields

$$\Delta t_{\lambda=0} = \frac{\xi t}{\sigma_v} = \frac{L}{\sigma_v}\,, \tag{4.33}$$

and, thus, Eqn. (4.29) implies that we should have $\tilde{c} \leq 1$. This shows that, in the relativistic limit, Eqns. (4.29) and (4.32) still leave some freedom as to the choice of $\tilde{c}$. However, in the non-relativistic limit this is not the case. Taking into account that Eqns. (2.19) imply that

$$\frac{\xi}{\sigma_v}(1-\lambda) = |k_w + \tilde{c}| > 0\,, \tag{4.34}$$

one finds that, in the $\lambda \to 1^-$ limit, Δt should be infinitely larger than L/σ_v. It then follows from Eqn. (4.29) that $\tilde{c}$ must necessarily vanish in this limit.

This conclusion can likewise be reached by utilizing the analytical approximations derived in the previous section. Let us consider the collapse of spherical ($s = 2$) domains. Equation (2.21) together with the definitions in section 2.3 shows that the energy of these domain walls just before collapse to a point is given by

$$\begin{aligned} E(\eta, q_{i\star}) &= 4\pi\sigma(a\eta)^2\tau_\star^{-2}(\tilde{q}^2\gamma)_\star \\ &= 4\pi\sigma(a\eta)^2\tau_\star^{-4}\,, \end{aligned} \tag{4.35}$$

where, $(\tilde{q}^2\gamma)_\star$ is the asymptotic value of $\tilde{q}^2\gamma$, which according to the analytical solutions (4.3, 4.2) is in the non-relativistic limit given by

$$(\tilde{q}^2\gamma)_\star = \tau_\star^{-2}\,. \tag{4.36}$$

In this case the energy density lost by domain walls in the conformal time interval $[\eta, \eta + d\eta]$ is given by

$$\begin{aligned} d\rho_{\rm loss} &= \int_{q_{i\star}(\eta)}^{q_{i\star}(\eta+d\eta)} nE(\eta, q_{\rm i})\mathcal{P}(q_{\rm i})dq_{\rm i} \\ &= 3n_{\rm i}\eta_{\rm i}^3 a_i^3 a^{-3}E(\eta, q_{\rm i\star})q_{\rm i\star}^{-4}dq_{\rm i\star} \\ &= \frac{\beta\sigma}{\tau_\star}a^{-1}\eta^{-2}d\eta\,, \end{aligned} \tag{4.37}$$

where the probability distribution $\mathcal{P}$ is defined as in (2.24). Using $d\rho_{\rm loss}/dt = a^{-1}d\rho_{\rm loss}/d\eta$ and that $(1-\lambda)a\eta = t$ for a power-law evolution of the scale factor, we obtain

$$\left.\frac{d\rho}{dt}\right|_{\rm loss} = \frac{(1-\lambda)^2\beta\sigma}{\tau_\star}t^{-2}\,. \tag{4.38}$$

This result is consistent with the scaling of the energy loss term in the parametric VOS model, given in Eqn. (4.27). The energy loss is enhanced in the standard VOS model compared to Eqn. (4.38), however, by a factor of around 1.46 in the radiation era and 1.33 in the matter era. If we identify the pre-factors

$$\frac{(1-\lambda)^2\beta}{\tau_\star} = \frac{\tilde{c}\bar{v}}{\xi^2}\,, \tag{4.39}$$

and use

$$\bar{v} = \sqrt{\frac{1-\lambda}{2\lambda+1}}\,, \tag{4.40}$$

as well as equations (4.4) and (4.6), we can derive an analytical expression for the energy loss parameter $\tilde{c}$ valid in the $\lambda \to 1$ limit:

$$\tilde{c} = \frac{9(1-\lambda)}{2\beta\sqrt{(\lambda+1)(2\lambda+1)}}\,. \tag{4.41}$$

This corroborates our previous statement that $\tilde{c}$ is non-constant and vanishes for $\lambda \to 1$.

As a consequence, in the non-relativistic limit, the parametric VOS model must reduce to the parameter-free model as it effectively includes no additional source of energy loss (beyond expansion). In fact, in this limit, we should have

$$\sigma_v = \sqrt{\frac{1-\lambda}{3\lambda}} \quad \text{and} \quad \zeta = k_w \sqrt{\frac{1-\lambda}{3\lambda}}\,, \tag{4.42}$$

which has the same asymptotic behavior as the approximation derived in section 4.1.1 using the parameter-free model*. Notice that k_w in Eqn. (4.42) and C/β in Eqn. (4.6) are equivalent in the $\lambda \to 1^-$ limit.

This coincidence between both models in the $\lambda \to 1^-$ limit is in agreement with the conclusions of [195], where the parametric and parameter-free models were compared in detail. Therein they found that the parametric model overestimates the strength of the Hubble damping term — as it does not account for the dispersion of σ_v — and that the impact of wall decay on σ_v is not included. In the non-relativistic limit, however, these two effects are expected to be negligible and thus the two models should be equivalent for $\lambda \to 1^-$. Furthermore, the results of [195] indicate that $\tilde{c} \to 0$ in the $\lambda \to 1^-$ limit, in agreement with our previous discussion.

The fact that we necessarily have that $\tilde{c} \to 0$ in the $\lambda \to 1^-$ limit further implies that, if one uses different numerical simulations with a wide range of expansion rates to calibrate the parameters of the original VOS model, one will necessarily find that no unique calibration exists. This is precisely what was found in [159]: although in the relativistic limit simulations are well described by a $\tilde{c}$ close to unity, for fast expansion rates simulations are compatible with $\tilde{c} = 0$. Given these results, the authors proposed an extension of the VOS model, involving four additional free parameters, that provides a good fit to the results of their simulations. This multi-parameter VOS model drops the assumption that k is a constant — assuming that $k(\sigma_v)$ instead — and includes another energy loss term — a "radiation" term that depends on $k(\sigma_v)$ — while keeping the term in Eqn. (4.27) with a constant $\tilde{c}$. This multi-parameter model, however, reduces to the original VOS model in the non-relativistic limit (since the additional energy loss term becomes irrelevant in this limit and k becomes approximately constant) and, as a result, calibration with simulations, unsurprisingly, yielded the $\tilde{c} = 0$.

*The approximation in Sec. 4.1.1 was derived by taking into account the dominant term in the domain wall acceleration. A simpler approximation can be derived by neglecting the acceleration of the walls in this limit. In this case, domain wall evolution would still be described by Eqns. (4.3)-(4.2), but with $\tau_*^2 = 3\lambda/(1-\lambda)$. This leads to an approximation similar to Eqns. (4.6) and (4.10), but with the substitution $2\lambda + 1 \to 3\lambda$.

4.3. Testing the Parameter-Free Model With Collapsing Domains

In this section, we shall test whether the aforementioned deviations from the predictions of the parameter-free model and the results from field theory simulations in the relativistic regime can be attributed to systematic effects intrinsic to those simulations. This, as we have seen, is precisely the regime where domain wall evolution becomes harder to predict, as energy loss channels like scalar radiation become significant, and field theory simulations hit their limitations due to relativistic wall velocities and — going along with them — resolution problems due to the associated Lorentz contraction of walls. In the PFM, domain wall networks are modeled as nested domains that are either cylindrical or spherical and possess a particular distribution of initial radii. A simple way to check if the deviations from numerical simulations appear due to systematics in FT simulations or are rather an emergent effect due to the more complex dynamics in realistic networks that may not be adequately captured by the PFM, is to simulate the collapse of these cylindrical and spherical domains using the same techniques used in the numerical simulations of domain wall networks. This allows us to investigate whether we find significant deviations from the predictions of the Nambu-Goto approximation.

4.3.1 Simulating Collapsing Spherical and Cylindrical Domains

The analysis of spherical or cylindrical domains allows us to perform simulations in just one spatial dimension, as the only relevant quantities now become the radius of these domains and its change with time (similar simulations have been performed in [196]). This offers an advantage in terms of computational resources and allows us to go to much larger grid sizes compared to the ones we typically use in 2D or 3D network simulations. In order to solve the equation of motion in one spatial dimension, we have to re-write the Laplacian in (3.2) in spherical / cylindrical coordinates. In its discretized form, it becomes

$$(\nabla^2\phi)_i = \left(1+\frac{s}{2i}\right)\phi_{i+1} + \left(1-\frac{s}{2i}\right)\phi_{i-1} - 2\phi_i\,, \tag{4.43}$$

where we again use $s = 2$ / 1 to refer to the spherical / cylindrical case. With this modification, we can use the algorithm introduced in Eqn. (3.3) to obtain numerical results for the evolution of ϕ. For the simulations referred to within this section, we varied the initial wall thickness between $w_0 = 10 - 100$. The initial conformal time η_i was set to a value $w_0 < \eta_i \ll \eta_{\rm max}$, such that the Hubble radius at the beginning of the evolution is larger than the initial wall thickness. Moreover, as initial conditions, we assume that the radial

component of the field is described by the static solution of a wall at rest (2.3), centered around an initial comoving radius q_i.

Figure 4.4 depicts the evolution of a spherical domain wall with $\tau = \eta/q_i$ obtained from a typical simulation in one spatial dimension. One can observe the accelerated collapse towards the coordinate origin (behold the time steps, which are getting smaller towards the end of the collapse). In the late stages of collapse, the wall has accelerated to ultra-relativistic velocities and its thickness gets contracted up to a point where the wall cannot be resolved anymore by the lattice spacing.

We now would like to quantify the evolution of the collapse of spherical and cylindrical domain walls. To extract the domain wall velocity during collapse, we are using the method introduced in Eqn. (2.8). The comoving radius q can be extracted in different ways. For now, we simply determined the index of the maximum value of $1 - |\phi|$ in the grid, which is equal to the radius in comoving coordinates, since we use a grid spacing equal to one. For reference, we will call this the “max method” and compare it with a method related to the previously introduced energy density method later on. We then estimated the dynamical wall thickness w during the evolution by counting the points in the wall that fulfill the ϵ-criterion introduced in chapter 3. In the case of one-dimensional simulations, the renormalization with κ_0 gives us a relative thickness, which is initially equal to one. We will then observe a contraction of this thickness as the wall gains velocity that we will compare to the predicted Lorentz contraction using the relation

$$\gamma = \sqrt{1 + \gamma^2 v^2}\,. \tag{4.44}$$

To compare q and v to the evolution that is predicted in the thin wall approximation, we solved the Nambu-Goto equations of motion (2.22) numerically. Figure 4.5 shows a comparison of the values obtained from simulations and from the NG EOMs. From these plots, it becomes apparent that there is an almost perfect match between the prediction of $\tilde{q}$ and $\gamma^2 v^2$ from the thin wall approximation and the results from simulations. It is only in the very last stages of collapse that both start to deviate. The moment this deviation happens coincides with the point where the wall gets too thin to be accurately resolved in the grid. In these stages, we consistently observe that the velocity of the simulated walls cannot follow the increasing acceleration predicted by the Nambu-Goto model. Consequently, the measured radius will be larger than the predicted one. This can especially be seen in panel (b). Panels (e) and (f) illustrate the Lorentz contraction of the walls as they accelerate. In (f) the initial wall thickness $w_0 = 10$ was already quite small, which explains

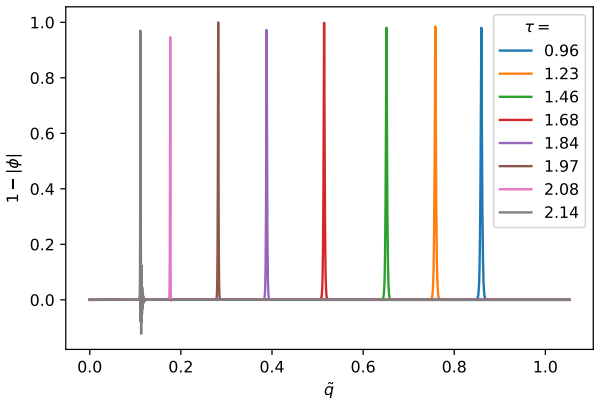

Figure 4.4: Collapse of a spherical domain wall, represented as $1 - |\phi|$, in the matter dominated era. With advancing τ the wall accelerates towards the origin while its thickness decreases due to Lorentz contraction. In the late stages of collapse resolution is lost and unphysical features appear.

the larger fluctuation in counting the points that belong to the wall. Besides that, there is a close correspondence between the wall thickness and the measured Lorentz factor. The results presented here hint that the crucial parameter that determines at which point the results from the simulations are no longer trustworthy is the initial thickness of the walls w_0. If this initial wall thickness is larger, we can trace the walls to higher velocities, i.e., to later stages of collapse.

To corroborate this hypothesis, we performed several identical simulations of the collapse of a spherical domain with a fixed initial radius, varying w_0. At the point where the discrepancy between the results for $\gamma^2 v^2$ of the simulation and the Nambu-Goto prediction exceeded 10 %, we stopped the simulation (at this point the discrepancy in $\tilde{q}$ was always well below 10 %). Let now $\tilde{q}_{\mathrm{bd}}$, ${\gamma^2 v^2}_{\mathrm{bd}}$ and w_{bd} be the last results that we extracted from the simulation before it breaks down. Hence, we can consider $\tilde{q}_{\mathrm{bd}}$ as minimal radius and ${\gamma^2 v^2}_{\mathrm{bd}}$ as maximal velocity, for which $\delta q_{\mathrm{bd}} < \delta(\gamma^2 v^2_{\mathrm{bd}}) < 0.1$ still holds, δ being the relative error between simulation and Nambu-Goto results. Figure 4.6 shows how these quantities change as a function of the initial wall thickness w_0. As expected, the reduced radius $\tilde{q}$ at the time the simulations break down decreases significantly with increasing w_0. Noteworthily, for a relatively small initial wall thickness of $w_0 = 10$, a typical wall thickness used in domain wall network simulations, this breakdown happens as soon as approximately half-way through the collapse. Furthermore, it is interesting to note that $\gamma^2 v^2_{\mathrm{bd}}$ shows an approximately linear increase with w_0.

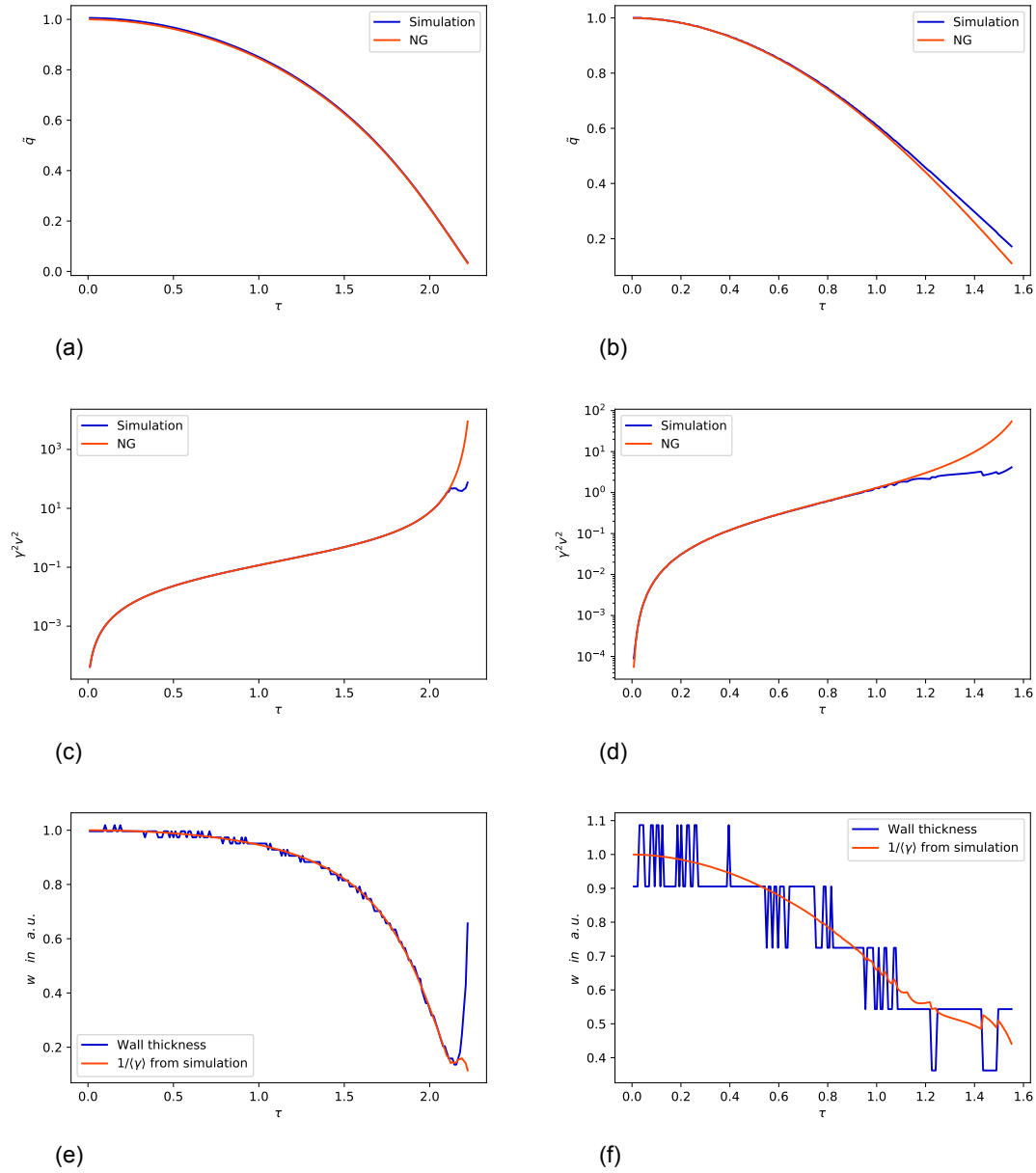

Figure 4.5: Panels (a), (b), (c) and (d) display the radius $\tilde{q} = q/q_i$ as well as $\gamma^2 v^2$ extracted from 1D simulations, alongside the numerical solution obtained from the Nambu-Goto equations of motion. Panels (e) and (f) show the dynamical thickness of the wall compared to the value of $\langle\gamma\rangle^{-1}$, both extracted from the simulation. The plots on the left correspond to the collapse of a spherical domain with initial radius $q_i = 8550$ and initial wall thickness $w_0 = 80$ in matter-domination. The plots on the right describe the evolution of a cylindrical domain with $q_i = 477$ and $w_0 = 10$ in a slowly expanding universe with $\lambda = 0.1$.

4.3.2 Numerical Tests of the PFM

The objective of this section is to use the values that we measured from the simulation of collapsing spherical and cylindrical domains to compute predictions for ζ and σ_v of domain wall networks, based on the underlying assumptions of the PFM. In order to obtain a meaningful comparison to the simulations used to calibrate the free parameters of the

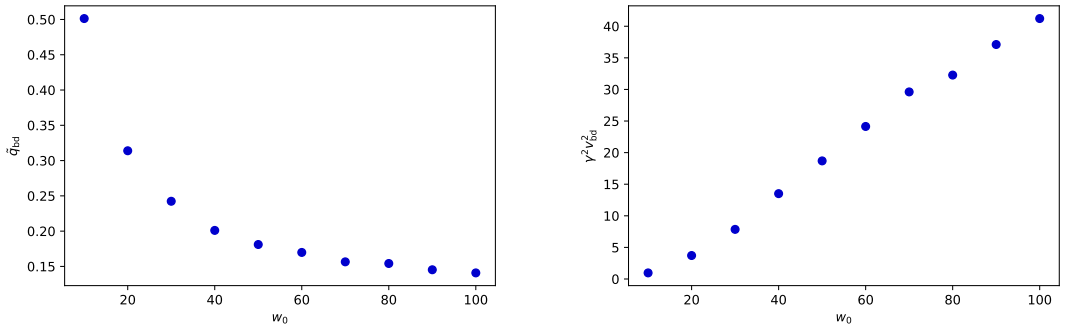

(a) (b)

Figure 4.6: The values $\tilde{q}_{\mathrm{bd}}$ (panel (a)), $\gamma^2 v^2{}_{\mathrm{bd}}$ (panel (b)) of the minimum radius and maximum velocity for which we can consider the results of simulations accurate. Here, the dependence of these quantities on the initial wall thickness w_0 is shown.

standard VOS model [159, 175] it is vital to extract the relevant quantities in the same manner. For this reason, we complement the previously used max method to measure the comoving radius by a method that is closely related to the energy density method introduced in chapter 3. This can be done by solving Eqn. (2.21) for q:

$$q(\tau) = \left(\frac{\sum \rho(\tau)}{\sigma_0 2\pi s \gamma(\tau)} \right)^{\frac{1}{s}} . \tag{4.45}$$

Here we used the fact that the volume of each of the grid cells equals unity and that the sum over the energy densities yields the total wall energy. To ensure we only count contributions from the wall and not from scalar radiation, we use the ϵ-criterion to decide which points to consider in the sum. We then calculate the wall tension at rest via Eqn. (3.13) and infer γ once again using (2.8) and (4.44). We will refer to the estimation of q via Eqn. (4.45) as the "energy method". Initial simulations showed, however, that for 1D lattices the number of grid points within the wall is insufficient to extract the radius with the energy method reliably. Therefore, we decided to run the simulations in a higher dimensional lattice again. This comes with the benefit of making our results even more comparable to the mentioned field theory simulations, as it ensures we do not miss potential higher-dimensional effects. In the case of the collapse of cylindrical domains in the xy-plane, there is no gradient of the field along the z-direction, and therefore the situation can fully be modeled within 2D simulations. To simulate the collapse of spherical domains, on the other hand, we used cubic lattices. In both cases, a small adaptation in the extraction of the radius using the max method was required (as for 2D and 3D simulations it is no longer possible to let the center of domains coincide with the coordinate origin of the grid), which we now simply calculated as the Euclidean distance between the index

for which the maximum of $1 - |\phi|$ appears and the center of the simulation box.

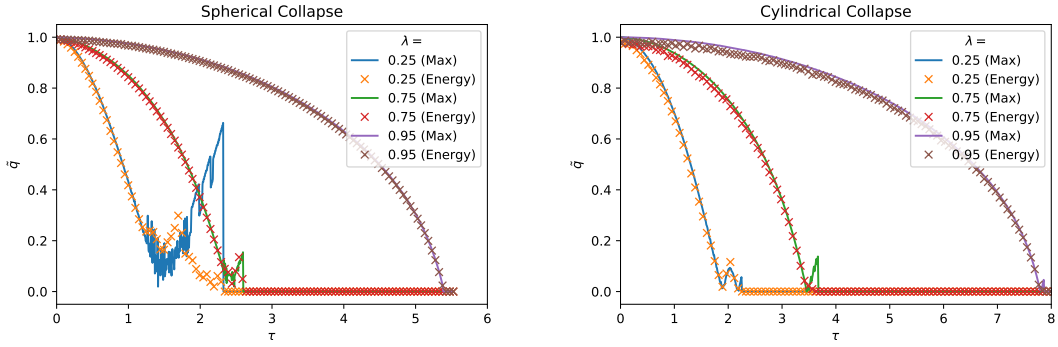

(a) (b)

Figure 4.7: Comparison of the max method and the energy method for the measurement of the rescaled comoving radius $\tilde{q}$ of domains during their collapse. The plot on the left represents spherical domains simulated in 3D while the right plot shows cylindrical domains in a 2D grid. The solid lines correspond to the max method at different expansion rates λ. Superimposed are the corresponding measurements obtained using the energy method, indicated by the x-markers.

Figure 4.7 shows a comparison between the rescaled radii $\tilde{q}$ measured with the max method and the calculation with the energy method for both 2D and 3D simulations. We observe that both methods yield consistent results. While the energy method slightly underestimates the radius q compared to the max method, this difference is below 2 % except for the very last stages of collapse, where larger deviations show up.

A last step to take in order to make predictions comparable to the model is to find $\tau_\star$ for all λ. Simulations fail to resolve walls properly once they reach ultra-relativistic velocities, so that it is impossible to infer the exact time of collapse. Moreover, in these last collapse stages, walls will lose a significant amount of energy due to particle radiation. Nevertheless, it is possible to define $\tau_\star$ in a suitable way by applying the criterion that the measured energy density has to vanish, or equivalently that there are no longer points in the grid that fulfill the ϵ-criterion. As the energy loss to scalar radiation increases, this criterion will inevitably be fulfilled at the end of collapse, and it is precisely then that the collapsed domain wall ceases to contribute to the characteristic length and RMS velocity in a network simulation.

The values of $\tau_\star$ measured in this way are plotted in figure 4.8 for different λ, alongside the collapse times predicted by the Nambu-Goto model. We observe that the collapse time quickly diverges for λ close to unity, which can be explained by the fact that the fast cosmic expansion withstands the collapse of domains in this regime. Here, the Nambu-Goto model predictions and the results obtained from our simulations coincide very well,

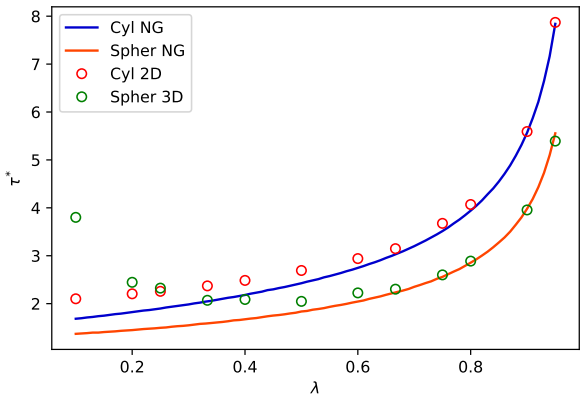

Figure 4.8: Values of $\tau_\star$ measured in 2D and 3D simulations (plotted as red and green dots respectively), obtained by requiring a vanishing energy density in walls for various expansion rates λ. For comparison, the corresponding predicted collapse times of the Nambu-Goto model are plotted as solid lines.

and are also in agreement with the analytical approximation (4.4) we obtained in this limit. For smaller values of λ, domains will collapse quicker, reaching higher average velocities. In this regime, the presence of scalar radiation and potentially also self-interaction of this radiation with the wall prevents the energy density from vanishing quickly, thus artificially increasing the wall's lifetime [197, 198].

The measurements of $\tilde{q}(\tau)$ with the energy method as well as $\gamma(\tau)$ and the numerical value of $\tau_\star$ enable us to compute ζ and σ_v using the formalism of the PFM, i.e., via evaluating the integrals (2.26) and (2.27). For comparison, we also recomputed these integrals using the evolution of $q(\tau)$ and $\gamma(\tau)$ as given by the Nambu-Goto EOMs. The results of these calculations, together with the values obtained from the network simulations [159, 175] are shown in figure 4.9. It is eye-catching that the results obtained from our simulations reproduce the prediction of the model obtained from the Nambu-Goto equations well, both in shape and magnitude. A possible source for the minor deviations in this case is the box size used in our simulation (and hence also the initial domain radius, which we chose to scale linearly with the box size). In some sense, this again makes our simulations even more comparable to the network simulations, as typical domain sizes in a network simulation are not better or may even be worse in terms of resolution. To investigate this relationship, we ran further simulations with different box sizes. Generally, an increase in grid size indeed seems to lead to a better agreement of the simulations and the model. A decrease in grid size, on the other hand, does not necessarily lead to a better agreement with the network simulations, but rather to a larger statistical spread of the measured quantities.

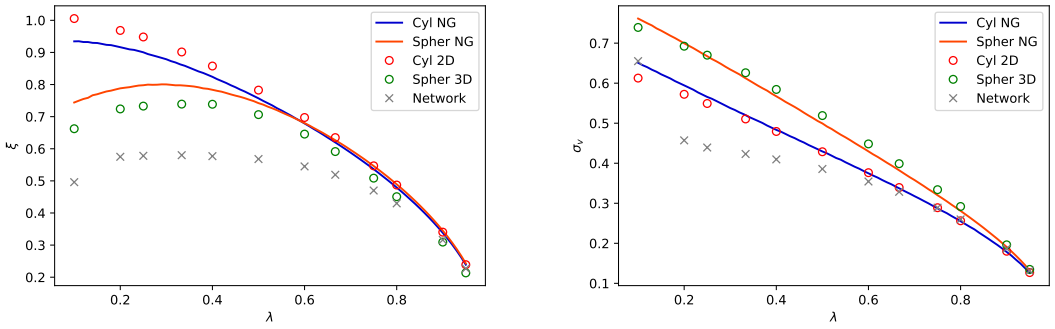

(a) (b)

Figure 4.9: Results of the simulations of collapsing cylindrical (2D) and spherical (3D) domains for a range of different expansion rates λ (shown as red and green dots respectively). The plot on the left corresponds to the value of ζ while the right plot shows the RMS velocity σ_v. The solid lines correspond to the predictions of the parameter-free model based on the Nambu-Goto equations of motion for these domains. The gray markers in contrast show the values extracted from simulations of domain wall networks [159, 175].

Despite the longer collapse time $\tau_\star$ that we measure for small λ (as compared to the NG prediction), which should generally lead to a decrease in the measured characteristic length, the values of ζ in the spherical case are not sufficiently suppressed to explain the deviation of the model and network simulations, and even exceed the model predictions in the case of cylindrical domains. To understand why this is the case, we can look at figure 4.10, which displays the value of $\tilde{q}\gamma$ for the case of a collapsing cylindrical wall. This plot illustrates that the value of $\tilde{q}\gamma$, which directly enters the integrals (2.26, 2.27)

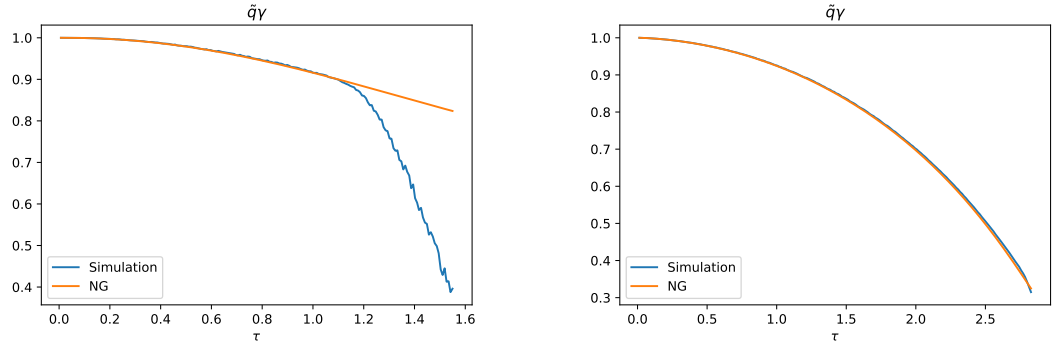

Figure 4.10: A comparison of the value of $\tilde{q}\gamma(\tau)$ traced over the collapse of a cylindrical wall obtained from simulations and the NG EOMs. The left plot diplays the $\lambda = 0.1$ case and the right plot represents the evolution in a matter-dominated background.

used to calculate ζ and σ_v, shows some significant deviation from the NG prediction at the end stages of collapse and quickly approaches zero in the $\lambda = 0.1$ case. Further tests have shown that this behavior is more universal: the value of $\tilde{q}^s\gamma$ always becomes small towards the end of the simulation, rendering the exact value of $\tau_\star$ largely irrelevant

for the estimation of ζ and σ_v. This is opposed to the expectation we have from the NG model, in which $\tilde{q}^s\gamma$ approaches a constant for $\lambda \to 0$. To some extent, this explains the somehow surprisingly good correspondence of the simulated quantities and the model in another manner: From the analysis of collapsing domains in 1D simulations in the last chapter, we saw that the values of q were overestimated and those for γ underestimated in the late stages of collapse. In order to give a good match with the values of ζ and σ_v that are predicted by the model, both effects somehow have to cancel each other. That is especially unlikely given the different powers in which q enters the integral in the spherical and cylindrical case. Again, that can well be explained if one considers that walls have little energy in their final stages, so that the contribution to the integrals (2.26, 2.27) is negligible here.

The good match between our current results and the model prediction suggests that the way quantities are extracted from field theory simulations cannot solely explain the deviation of the model and the parameters found from network simulations. Thus, it becomes more likely that other effects, which are only relevant in the case of realistic walls appearing in networks, as opposed to idealized symmetric domain walls, add a non-negligible contribution to the energy budget. These can, for example, be small-scale perturbations traveling along the walls that contribute to their kinetic energy, or some not yet understood mechanism that slows down the energy loss in networks.

5. Non-Standard Domain Wall Scenarios

In a vast majority of studies in the literature, domain walls are typically minimally coupled to gravity in a homogeneous background, although there exists a number of noteworthy exceptions [199, 200]. These are often associated with so-called symmetron models of scalar fields, which mediate long-range forces while naturally evading local tests of gravity through an environment–dependent screening mechanism [30, 161, 162, 201]. In fact, coupling domain walls non-minimally to matter overdensities can change their dynamics on small and large scales. Here, we study the influence of such interactions by considering a toy model. Based on this model, we develop a simple analytical framework in section 5.1 to determine which regions of the parameter space allow walls to transit compact objects. We then test the predictions of this framework with field theory simulations. Furthermore, we observe that the interaction between compact objects and domain walls can excite internal modes in the domain wall solution that manifest as small-scale structure on the wall. We investigate this in more detail in section 5.1.2.

In section 5.2, we explore domain walls in a modified ϕ^6-like potential. Due to its third vacuum state, the ϕ^6-potential allows for the formation of different types of domain walls (see, for example, [202, 203] for studies of ϕ^6-kinks in the literature). By adding a bias term to the potential, we observe that the collapse of domain walls can trigger an initially unpopulated true vacuum to become populated. Thereby, as our preliminary simulations show, this can induce a cosmological phase transition. In the course of section 5.2 we develop an analytical model to describe under which circumstances such a phase transition can occur and discuss its predictions.

5.1. Domain Wall Interactions with Compact Objects

In this section, we will consider domain walls that can interact with spatial distributions of matter overdensities. We will model this interaction with a coupling term of the form

$$\mathcal{L}_{\text{int}} = \varrho_0 \exp\left[\Theta V(\phi)\right], \tag{5.1}$$

which is added to the Lagrangian of the standard Goldstone model (1.11, 2.1). Here ϱ_0 is the background density of the matter field (which we choose to be homogeneous inside the object for simplicity) and Θ the coupling constant. This definition ensures that there is no interaction in regions where the field is in one of its vacuum states. Further, we

demand the coupling to be weak, i.e. $\Theta V(\phi) \leq \Theta V_0 \ll 1$. In this limit, we can define an effective coupling strength given by

$$I_e \approx \varrho_0 \Theta \,. \tag{5.2}$$

As the interactions we are investigating are local, it is sufficient to consider a Minkowski spacetime and neglect the expansion of the cosmological background. Variation of the action then leads to the equation of motion

$$\frac{\partial^2 \phi}{\partial t^2} - \nabla^2 \phi - \frac{\partial V(\phi)}{\partial \phi}(1 + \delta(x)\Theta \mathcal{L}_{\text{int}}) = 0 \,. \tag{5.3}$$

We heuristically added the $\delta(x)$ term to this EOM, which we will set to one for regions lying within a compact object and to zero otherwise (note that if $\delta(x) = 0$, the EOM reduces to that of the standard Goldstone model). The implicit dependence of the coupling term on ϕ is weak, and the $\partial V(\phi)/\partial\phi$ term in Eqn. (5.3) is — to first order — multiplied by a constant term $(1 + I_e)$ inside an astrophysical object. It follows that a domain wall that lies at rest within such an object is well described by the static solution of a free domain wall (as given in (2.3)), with a modified thickness $w_1 = w_0/\sqrt{1 + I_e}$ (because this last term in the EOM is proportional to w^{-2}). Consequently, the wall's rest mass within the object, which is inversely proportional to its thickness, is

$$\sigma_1 = \sigma_0 \sqrt{1 + I_e} \,. \tag{5.4}$$

Preliminary field theory simulations we carried out indicated the emergence of interesting physics, such as perturbations that travel along the walls (which we will discuss in more detail in section 5.1.2) and potentially a freezing of domain wall networks induced by an underlying matter distribution. However, studying these interactions within a domain wall network complicates a more fundamental, quantitative analysis of those processes. We therefore decided to take a step back and investigate the interaction in a simplified setup, which allows us to identify the key physical parameters. This setup consists of a planar wall moving with a constant velocity (corresponding to a Lorentz factor γ_0) along the x-axis in Minkowski space, where it eventually collides with a flat, infinitely extended object. Besides the fact that this setup limits the number of possible outcomes of the interaction (to basically passage or reflection), it also allows us to perform the corresponding field theory simulations in 1D, therefore enabling us to probe a larger parameter space thanks to the reduced memory requirements.

Note that a careful choice of the initial conditions is vital for the simulations performed within this section, as it will not only guarantee a well-defined initial energy of the wall, but also prevent possible energy losses before the collision takes place due to relaxation processes. Here, we initialized the field ϕ with the Lorentz contracted static solution at $x = x_0$ as given in Eqn. (3.11) and its time derivative with

$$\dot{\phi}_{\text{init}} = 2\sqrt{V_0}\sqrt{\gamma_0^2 - 1}\left(\tanh^2\left[(\pi\gamma_0/w_0)\left(x - x_0 + \sqrt{1-\gamma_0^{-2}}\triangle t/2\right)\right] - 1\right) \tag{5.5}$$

The last term in the hyperbolic tangent accounts for the fact that the discrete solving scheme evaluates ϕ at integer time steps of size $\triangle t$, while its time derivatives are evaluated at half-integer steps.

5.1.1 Estimating the Critical Coupling Strength

We now investigate two limiting cases: the wall being much thinner than the astrophysical object, as well as the opposite case. Our goal is to forecast the set of parameters for which the wall will either pass through or be reflected by the object, based on its initial velocity.

The Thin Wall Case We will start by discussing the simpler thin wall scenario. In this case, the increase in mass the wall exhibits when inside the object is proportional to the rest mass per unit area σ_0 of the free wall. We can write an equation for the energy balance of the wall before (LHS) and after colliding with the wall (RHS):

$$\gamma_0\sigma_0 = (1+\varepsilon)\gamma_1\sigma_1\,. \tag{5.6}$$

Here we introduced the parameter ε to model potential inelasticities of the collision process. For a fully elastic collision, energy is conserved and therefore $\varepsilon = 0$. Using equation (5.4), this allows us to predict a critical value $I_{e,c}$ of the effective coupling, above which we expect reflection of the wall instead of the wall simply passing through the object (note that for simplicity we neglected potential momentum transfers to the compact object and kept its position in our simulations fixed). Assuming an elastic collision, this value is given by

$$I_{e,c} = \gamma_0^2 - 1\,. \tag{5.7}$$

Simulations show that these collisions are indeed approximately elastic. However, there is an increase in inelasticity for higher domain wall velocities that can likely be attributed to

an enhanced emission of scalar radiation or the excitation of internal modes. We therefore allow for a non-zero ε that can increase with γ_0: $\varepsilon = c_f(\gamma_0 - 1)$, c_f being a free parameter. By performing field theory simulations of the collisions, varying the effective coupling constant in small steps, we can find its critical value, above which a reflection of the wall is observed. Figure 5.1 shows a comparison of the values of $\varrho_{0,c} = I_{e,c}/\Theta$ found in simulations with the theoretical prediction from Eqn. (5.7). This shows that in the case

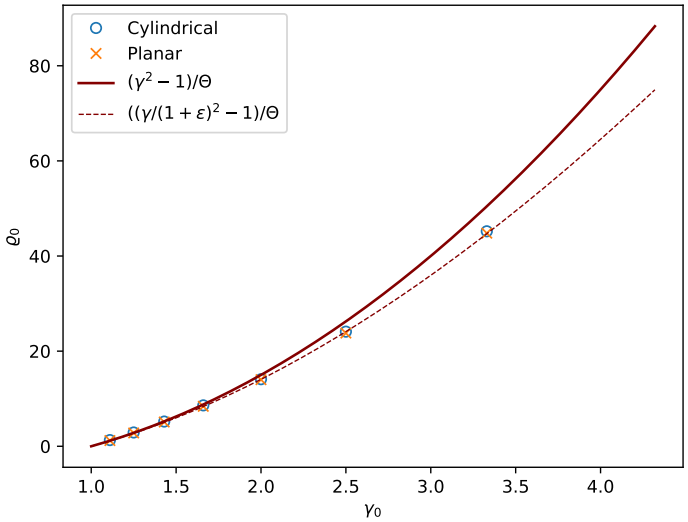

Figure 5.1: The critical density $\varrho_{0,c} = I_{e,c}/\Theta$ as a function of the initial Lorentz factor γ_0 for thin walls. The solid line represents the prediction for elastic collisions, the symbols represent measurements from simulations and the dashed line is a fit obtained by allowing for a non-zero energy loss parameter ε.

of a thin wall and sufficiently low γ_0, we can almost perfectly predict the critical coupling from first principles and assuming an elastic collision. Allowing for a non-zero ε and fitting the parameter $c_f = d\varepsilon/d\gamma_0$ to our simulation results, we observe a mild increase in inelasticity of the order of 2 % per unit increase in γ_0.

Additionally to the mentioned 1D simulations of collisions of a planar wall with the object, we performed simulations in 2D of a cylindrical wall, which collapses under its own tension onto a likewise cylindrical compact object with a smaller radius. The results of these simulations are symbolized by the small circles in figure 5.1. They show that a prediction of whether the wall will transit an object is possible solely with the knowledge of the underlying field theoretical parameters. In fact, the simple model we constructed here is largely independent of the geometry underlying the collision.

The Thick Wall Case In the case where the wall thickness exceeds the object radius, an analytic static solution describing the wall profile is more difficult to obtain. However, we know that the wall is compressed in the part that lies inside the object and approximately follows the free wall solution in the outer part. Let us consider a wall that is centered around the object. We can then obtain an expression for the tension of the wall in an empirical way, by considering two separate contributions from inside and outside of the object:

$$\sigma_1 \equiv \sigma_1^{(i)} + \sigma_1^{(o)} \,. \tag{5.8}$$

Re-writing the energy density profile of the static solution (2.9) for a wall with arbitrary thickness w_k yields

$$\rho(w_k, x) \equiv \frac{\pi^2}{2w_k^2} \mathrm{sech}^4 \left[\frac{\pi}{\sqrt{2} w_k} x \right] . \tag{5.9}$$

In the same way, let $\phi(w_k, x)$ be the static solution of a wall with thickness w_k. In a realistic scenario, the field ϕ will interpolate between the two boundary solutions (corresponding to walls with a thickness w_0 and w_1, respectively) and have a slightly flatter gradient inside the object as the solution described by $\phi(w_1, x)$. Therefore, the contribution to the rest mass from inside the object (which coincides with the center region of the wall, where most of its energy is concentrated) will be overestimated. Likewise, the wall profile will be slightly steeper than the free wall profile in the outer regions of the object; however, the energy density of the wall is much smaller in these outer regions, and therefore this will not induce a significant error in the calculation of the rest mass. Moreover, the field should of course be continuous at the boundary of the object but $\phi(w_0, r_e) \equiv \phi(w_1, r_0) \neq \phi(w_0, r_0)$. Here we defined an effective object radius $r_e = r_0\sqrt{1 + I_e}$.

These considerations suggest defining the inner and outer contributions to σ_1 in Eqn. (5.8) in the following way:

$$\begin{aligned} \sigma_1^{(i)} &= 2 \textstyle\int_0^{r_0} \rho(w_1, x) dx \\ \sigma_1^{(o)} &= 2 \textstyle\int_{r_e}^{w_0/2} \rho(w_0, x) dx \,. \end{aligned} \tag{5.10}$$

By setting the lower boundary of the second integral in (5.10) to r_e, we restrict the integration to a domain in which ϕ is indeed continuous and at the same time compensate for the overestimated contribution to σ_1 from the inner integral. Therefore, r_e can in some sense be interpreted as the radius in which the object exerts influence on the domain wall. This is illustrated in figure 5.2, which displays the energy densities $\rho(w_0, x)$, $\rho(w_1, x)$ together with the corresponding static solutions for the field ϕ.

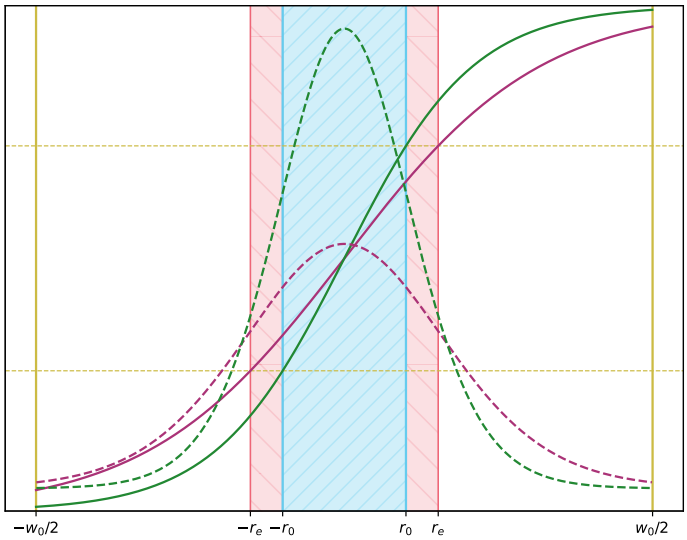

Figure 5.2: Energy densities $\rho(w_0, x)$ (purple) and $\rho(w_1, x)$ (green) as dashed lines as well as the corresponding static wall solutions as solid lines. The vertical lines represent the radii $\pm r_0$, $\pm r_e$ and $\pm w_0/2$ (from the origin to outside). The horizontal lines represent $\phi(w_1, \pm r_0) = \phi(w_0, \pm r_e)$.

Note that if the object radius r_0 exceeds a value of $w_0/(2\sqrt{1+I_e})$, $\sigma_1^{(i)}$ would predict a larger surface mass than the total surface mass in the thin wall case. To avoid this rather unphysical behavior, we set $r_0 = w_0/(2\sqrt{1+I_e})$ and $\sigma_1^o = 0$ in this case. This choice not only guarantees that the thick wall solutions converge to the thin wall solution for growing object radii, but also allows us to refine the definition of a thin wall: A wall can be considered thin in relation to the object if $w_0/(2r_0) \lesssim \sqrt{1+I_e}$ and vice versa. The effective model introduced here is invariant under a rescaling of the wall thickness w_0 and the object radius r_0 with some constant. The physical behavior is solely determined by the ratio between those two scales.

The energy conservation equation (5.6), as a result of the complex definition of σ_1, takes a more complicated form but can still be solved numerically for the critical value of the coupling $I_{e,c}$. The results predicted by this model are summarized in figure 5.3 assuming a fully elastic collision (left panel) and allowing for a non-zero ε (right panel). As intended, for increasingly larger object sizes, the predictions will asymptotically merge with the prediction of the thin wall case. For the simulations shown here, we kept the wall width at a fixed value of 2000 grid points and varied the object radius r_0 in a broad range between 50 - 500 grid points. In the case of a thick wall, the results we obtained are very preliminary and more simulations need to be performed in order to be able to make more quantitative predictions. So far, the best fit of the model to the data points is obtained for an inelasticity of the order of 7 % per unit increase in γ_0, in agreement with our observation of a larger

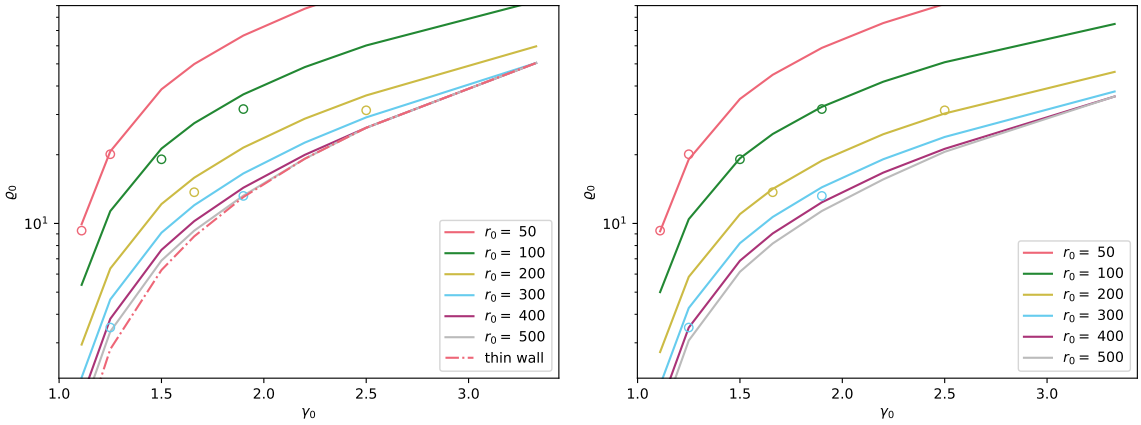

Figure 5.3: The critical density $\varrho_{0,c} = I_{e,c}/\Theta$ as a function of the initial Lorentz factor γ_0 for thick walls. The symbols represent measurements from simulations with a fixed wall width ($w_0 = 2000$) and varying the width of the object r_0. In the left panel the solid lines represent the prediction from the model described in the text, assuming an elastic collision. For comparison, we also plotted the curve representing the thin wall case. In the right panel we allowed for a non-zero energy loss parameter ε.

energy loss to radiation in the thick wall case. In the next section, we will analyze the aftermath of collisions between domain walls and compact objects.

5.1.2 Collision-Induced Small-Scale Structure

In the following, we will consider the case of a thin wall, carrying sufficient energy to pass through a compact object. Due to the coupling, the portion of the domain wall that penetrates the compact object acquires additional mass by trading off some of its initial kinetic energy. In other words, the Lorentz factor of the wall inside the object will be smaller than the initial one: $\gamma_1 < \gamma_0$. As we discussed above, the interaction is, especially in the thin wall case, an elastic process to a good approximation. We can then calculate the value of γ_1 using the energy conservation equation (5.6), neglecting a possibly non-zero ε for now. As a consequence of the negligible energy loss, the wall will, after having passed the object, again be accelerated to a velocity close to its original value: $\gamma_2 \lesssim \gamma_0$. This is demonstrated in figure 5.4. Due to the wall propagating inside the object with a lower velocity than in the vacuum, its thickness gets compressed the moment it makes contact with the object. Likewise, it expands the moment it leaves the object and propagates in vacuum again. Simulations show that this causes oscillations in both the wall's velocity and thickness (as displayed in figure 5.4). Such behavior can be interpreted as a continuous exchange between kinetic and potential energy: As the wall width becomes smaller, its mass (which is inversely proportional to its width) increases, and the wall decelerates. This phase is then followed by a stretching of the wall width, along with an increase in kinetic energy. Figure 5.4 also shows that the frequency and amplitude of the oscillation

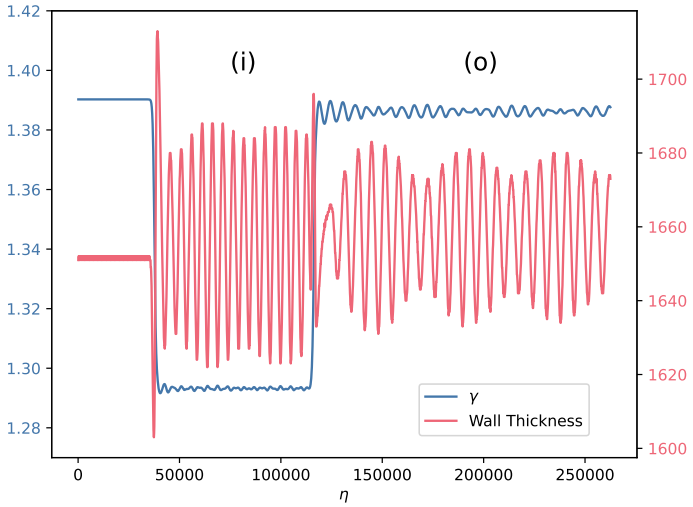

Figure 5.4: Lorentz factor and thickness of a wall colliding with an object, propagating through it (region (i)) and leaving the object again (region (o)). The x-axis represents conformal time. The moment the collision occurs is characterized by a drop in velocity and the onset of oscillations in both curves. After having passed the object the Lorentz factor increases again to a value close to its initial one and frequency and amplitude of the oscillations change.

differ depending on whether the wall is still inside the object or has passed through it. To quantify this observation, we performed separate Fourier analyses of the time curves that represent the wall thickness for the inner and outer regions, varying the parameters of the coupling, as well as the initial wall velocity. From the spectra we obtained, we extracted the dominant frequency of oscillation*.

Let us define an effective wall thickness by

$$\begin{aligned} w_{\text{eff}}^{(i)} &= \frac{w_0\gamma_1}{\sqrt{1+I_e}} \\ w_{\text{eff}}^{(o)} &= w_0\gamma_2 \end{aligned} \tag{5.11}$$

where the superscripts (i)/(o) refer to the regions inside/outside the object. Figure 5.5 shows that the frequency of the observed oscillation is in good approximation proportional to the inverse of this effective thickness of the wall. This result may have important implications. While commonly walls are described as featureless, the simulations we performed show that, provided there is a coupling with the standard model or dark sector, walls can develop perturbations of their thickness. Similar excitations have been studied in [204], where they have been shown to be long-lived when considering scalar radiation as a primary decay channel. However, this is not true in regions of high curvature, where the presence of small-scale structure leads to an increase in radiation. In this case, the

*Having a closer look at the time curve in figure 5.4, it becomes apparent that there is a beat in the oscillation, indicating the presence of a secondary frequency, possibly associated with a second relevant scale. Here, however, this will not be the subject of further analysis.

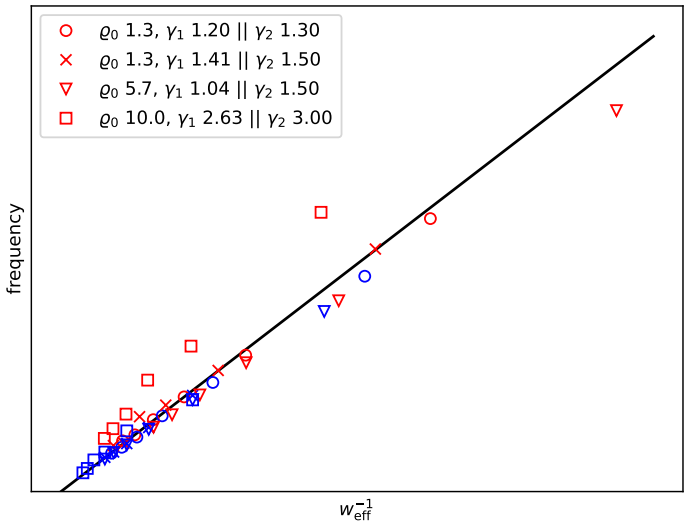

Figure 5.5: Frequencies of oscillation of the wall thickness as a function of the inverse of the effective wall thickness defined in (5.11). The black line represents $f = w_{\mathrm{eff}}^{-1}$. Red symbols correspond to frequencies in region (i) (inside the object) and blue symbols to frequencies in (o) (outside the object) respectively.

dynamics of domain walls can deviate from the Nambu-Goto description. The authors claim that these shape modes will not be relevant in late-time cosmology due to the lack of a mechanism generating them. Our simulations show that a coupling to a matter field might provide such a mechanism.

5.2. Late Time Phase Transitions Triggered By Collapsing Domain Walls

In this section, we will investigate the possibility of a late-time cosmological phase transition, triggered by the collapse of domain walls. As mentioned earlier, the work on this topic has been performed in collaboration with other researchers. In the following, I will focus on my contribution to this work. To begin with, we will consider a modified ϕ^6-potential as a toy model, which is given by

$$V(\phi) = V_0 \left[\phi^2 \left(\phi^2 - 1 \right)^2 + A \left[\tanh\left(\frac{\phi + 1}{\triangle} \right) - 1 \right] \right] . \tag{5.12}$$

This potential is plotted in figure 5.6 for an arbitrary set of parameters. The last term in (5.12) acts as a bias term that, for sufficiently small Δ, only affects the -1 vacuum state. The latter thereby becomes the true vacuum, while the 0 and 1 vacua are false vacuum states*. Carrying out 2D simulations of the evolution of cylindrical domain walls, inter-

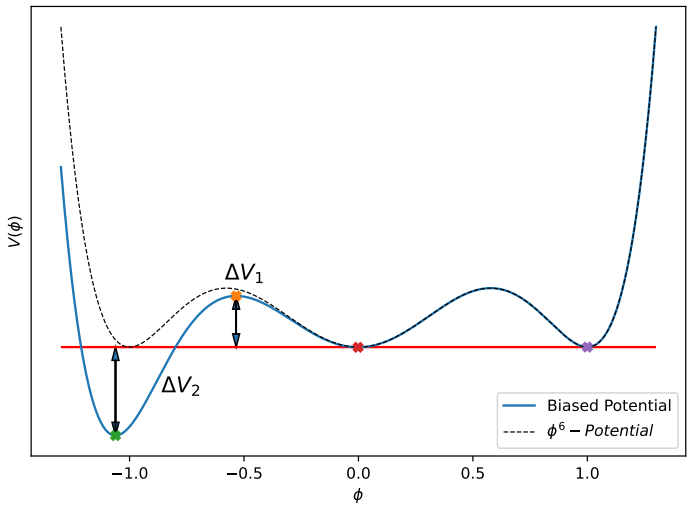

Figure 5.6: Potential given in (5.12) with $V_0 = 0.006$, $A = 0.2$ and $\triangle = 0.3$ (blue line). For comparison the unbiased ϕ^6-potential is plotted as a black dashed line.

polating between the two unbiased vacua (0 and 1), we observed that their collapse can induce a change of the topological sector, i.e., a local transition of the field into the -1 vacuum. As a consequence, a bubble of the true vacuum will be created and — provided it is sufficiently big — it will expand in space due to the volume pressure caused by the difference in energy density. This is illustrated in figure 5.7. Assuming a cosmological setting, in which the true vacuum is initially not populated or didn't exist before, a domain wall interpolating between the two false vacua will eventually collapse under its own tension once it enters the horizon, and the field may transition into its true vacuum state. This new

*Although the bias term slightly shifts the position of the vacua, we will refer to them as -1, 0 and 1 vacua.

state may expand rapidly in space until the whole universe is in the true vacuum state. This process can hence be regarded as a late-time phase transition, that is purely classical in nature and not triggered by a tunneling of the field. The aforementioned change

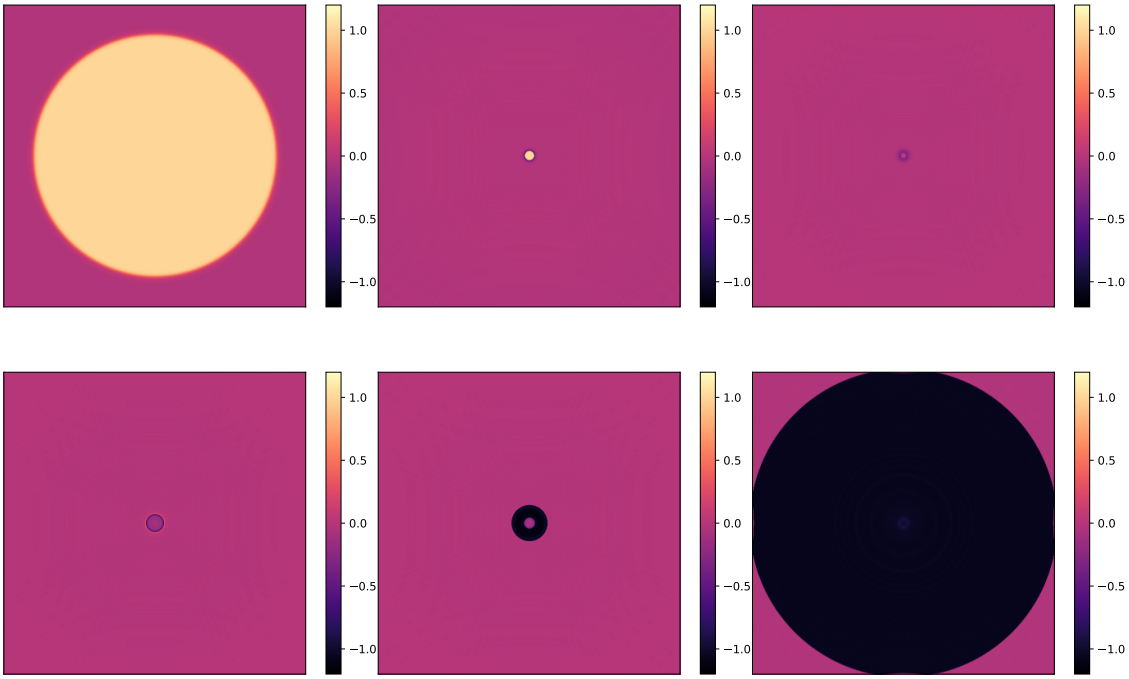

Figure 5.7: Snapshots from a 2D simulation of a collapsing cylindrical domain wall between the false vacuum states of the potential given in Eqn. (5.12). Upon collapse, a phase transition into the true vacuum state is induced. The snapshots show the time evolution from top left (initial conditions with a wall at rest) to bottom right (final state, where the true vacuum fills out almost all regions of the grid). The timesteps in between are not equally spaced, to feature particularly the moments around the time of collapse.

in the topological sector can only be induced by walls that have sufficient kinetic energy in their last stages of collapse. For background cosmologies in which Hubble damping does not dominate the curvature-based evolution of domain walls, this condition is equivalent to domains having a sufficiently large initial radius before their collapse. If a domain wall network is in a linear scaling regime, the radius of domains is roughly proportional to cosmic time. Therefore, understanding the minimum domain size required for a change in the topological sector enables us to anticipate the timing of such phase transitions in cosmic history. In the following, we will discuss a simple model to predict this minimal radius in terms of the parameters of the potential.

For the sake of simplification, let us again consider a cylindrical domain wall in Minkowski spacetime. We will first explore the condition for which a bubble in the true vacuum state will energetically prefer to expand instead of re-collapsing on itself. It is well known that there is a minimal, threshold radius r_t for which this is the case, which is given by [80, 108, 109]

$$\mathcal{V}(r_t)\Delta V_2 = \sigma_{\mathrm{tf}}\mathcal{A}(r_t)\,. \tag{5.13}$$

Here $\mathcal{V}(r_t)$ is the bubble volume, $\mathcal{A}(r_t)$ its surface area, ΔV_2 is the gain in potential energy as indicated in figure 5.6, σ_{tf} is the tension of the wall between the true and the false vacuum state. Since we are considering cylindrical domains, we simply have $\mathcal{V}(r_t) = r_t^2\pi$ and $\mathcal{A}(r_t) = 2\pi r_t$, from which follows that

$$r_t = \frac{2\sigma_{\mathrm{tf}}}{\Delta V_2}\,. \tag{5.14}$$

To produce a bubble in the true vacuum state that is large enough to expand, we hence need to lift a volume of $\mathcal{V}(r_t)$ from the false vacuum state over the potential barrier ΔV_1. The minimal energy required to do that should roughly be $E_{\mathrm{min}} \approx \mathcal{V}(r_t)\Delta V_1$. The source of energy for inducing this transition will eventually be the field's kinetic energy in the last stages of collapse of the false vacuum domain. In Minkowski space, the energy in the domain wall is conserved during the collapse and hence equals the energy of the initial domain at rest*. This energy is simply given by (cf. Eqn. (2.21)) $E_{\mathrm{rest}}(q) = 2\pi\sigma_{\mathrm{ff}}q_i$. q_i is the initial domain radius (note that in Minkowski space physical and comoving radius coincide) of the false vacuum domain and σ_{ff} is its tension. By demanding that the energy $E_{\mathrm{rest}}(q_{\mathrm{min}})$ for an initial radius q_{min} is larger (or equal) than the energy E_{min} required to lift a sufficient volume to the true vacuum state, we obtain the condition

$$q_{\mathrm{min}} \gtrsim \frac{2\sigma_{\mathrm{tf}}^2\Delta V_1}{\Delta V_2^2\sigma_{\mathrm{ff}}}\,. \tag{5.15}$$

A similar expression can be derived for spherical domains in three spatial dimensions. During the derivation of Eqn. (5.15) we implicitly assumed that all of the energy of the false vacuum bubble in the moment of its collapse is used to lift a sufficiently large volume of the field into the true vacuum. In reality, this will not be the case, as energy losses, e.g., into scalar radiation will occur. Therefore, the value given here should be regarded as a lower threshold.

*While in an expanding background a fraction of this energy is lost due to the Hubble damping. Here we will neglect this.

The quantities on the right-hand side of (5.15) are functions of the parameters of the potential. Obviously, ΔV_1 and ΔV_2 can be directly inferred from (5.12). We will get back to the calculation of σ_{ff} and σ_{tf} in a bit. First, it is useful from a simulations point of view to study the static solution of the domain wall interpolating between the two false vacua. This will help in finding appropriate initial conditions so that energy losses, associated with the relaxation of the field into the correct wall profile, can be avoided. For a large enough radius q_i of the initial domain, the radius of curvature may be neglected and we can find the static solution for a planar wall by (numerically) solving the EOM in one spatial dimension

$$\frac{d^2\phi}{dx^2} = \frac{dV}{d\phi}\,, \tag{5.16}$$

with the boundary conditions $\phi(-\infty) = \phi_0$ and $\phi(\infty) = \phi_1$, where ϕ_0 and ϕ_1 are respectively the exact VEVs of the 0 and 1 vacuum. This solution is plotted in figure 5.8, and in fact closely resembles the usual hyperbolic tangent solution of the ϕ^4-potential with a slightly modified thickness. Strictly speaking, a planar wall interpolating between the true

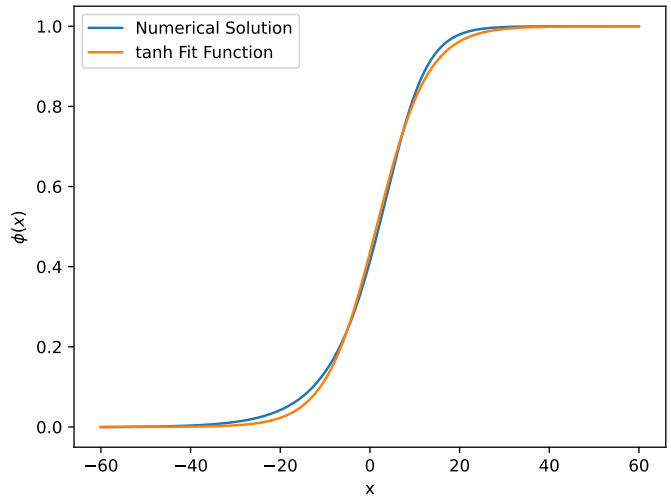

Figure 5.8: Numerically obtained static solution for the wall interpolating the (0,1) vacua of Eqn. (5.12). The orange line represents a hyperbolic tangent fitting function.

and the false vacuum doesn't possess a static solution — the wall will always accelerate towards the false vacuum in this case. On the other hand, the threshold radius r_t of a cylindrical wall represents a meta-stable point, at which volume pressure and tension cancel each other and where consequently such a wall may be static. If we consider the case of a small bias and a thin wall (i.e. one with a large curvature radius compared to its thickness), Eqn. (5.16) will hold true for such a wall to a good approximation.

The surface tension is defined as

$$\sigma = \int_{-\infty}^{\infty} \left[\frac{1}{2} \left(\frac{d\phi}{dx} \right)^2 + V(\phi) - V(\phi_i) \right] dx \,. \tag{5.17}$$

Here $V(\phi_i)$ for $i = -1, 0, 1$ shifts the zero point of the potential according to the lowest VEV we consider. If we calculate the tension between the (0-1) wall, σ_{ff}, this term may be neglected, since the energies of both vacuum expectation values $V(\phi_0) \approx V(\phi_1) \approx 0$ vanish approximately. In order to calculate σ_{tf} on the other hand, we have to shift the zero point of the potential energy by the amount $V(\phi_{-1}) = -\Delta V_2$. Calculating the wall profile $\phi(x)$ for the wall between the true and the false vacuum proved to be numerically challenging in some regions of the parameter space. However, we can circumvent this issue. Integrating Eqn. (5.16) one has

$$\frac{1}{2} \left(\frac{d\phi}{dx} \right)^2 = V(\phi) - V(\phi_i) \,, \tag{5.18}$$

so that the integrand in Eqn. (5.17) becomes $2(V(\phi) - V(\phi_i))$. Changing the integration variable from x to ϕ using $dx = [2(V(\phi) - V(\phi_i))]^{-1/2} d\phi$ we can therefore write (5.17) as

$$\sigma = \int_{\phi_i}^{\phi_j} \sqrt{2 \left(V(\phi) - V(\phi_j) \right)} d\phi \,, \tag{5.19}$$

with $(i, j) = (1, 0)$ if we want to calculate σ_{ff} and $(i, j) = (0, -1)$ for the calculation of σ_{tf} respectively. This integral can easily be evaluated for all regions in the $(V_0, A, \triangle)$ parameter space, without encountering numerical issues. Therefore, we can now calculate the minimal radius q_{min} of a domain required to induce a phase transition using Eqn. (5.15).

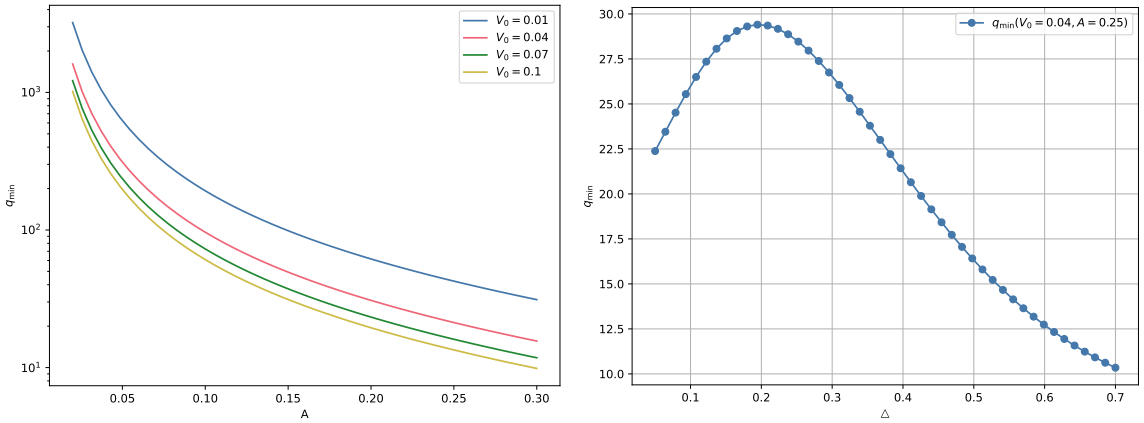

Figure 5.9: The minimal initial radius q_{min}, required for a collapsing cylindrical wall to induce a cosmological phase transition. The left plot shows this radius for a fixed $\triangle = 0.4$ as a function of A for four different values of V_0. In the right plot we fixed A and V_0 and plotted q_{min} as a function of $\triangle$.

The results are displayed in figure 5.9. In particular, the plot on the left hand side shows that the most crucial parameter determining $q_{\min}$ is A. This is unsurprising, as A is the parameter that controls the depth of the true vacuum state, and therefore the difference in potential energy between the true and the false vacua. In agreement with what would naively be expected, $q_{\min}$ decreases for increasing A while it diverges for $A \to 0$. The dependence on V_0, on the other hand, is less obvious, since all of the quantities on the RHS of Eqn. (5.15) implicitly depend on V_0. It turns out that according to our model, larger values of V_0 reduce the required size of domains in order to be able to induce a phase transition. Larger values of V_0 are associated with thinner walls, which therefore have a higher tension. The plot on the right hand side of figure 5.9 shows that there is also a mild dependency of $q_{\min}$ on $\triangle$. However, the value of $\triangle$ itself is also constrained by the requirement that the potential (5.12) must have a more or less smooth shape, and that the vacua at 0 and 1 should only be minimally affected by the bias term. Values of $\triangle$ below $\triangle \lesssim 0.1$ violate the first condition, as in this case the potential around the false vacuum state becomes very narrow, while values $\triangle \gtrsim 0.5$ violate the second condition because the 0 vacuum then experiences an increasing shift towards negative energies. Consequently, for the simulations we performed, we typically selected a $\triangle$ value close to the peak in figure 5.9 (right).

The work presented within this section is still preliminary. The predictions made by Eqn. (5.15) need to be tested with further simulations, which will allow us to verify or falsify this simple analytic model. It will also allow us to test which fraction of the energy in the collapsing domain is transferred into generating the true vacuum bubble and to which extent energy losses in scalar radiation need to be considered (which could be accounted for by introducing a term akin to the ε introduced in the previous section). If the general predictions by this model hold true, it can eventually be generalized for 3D domains that are affected by Hubble damping in an expanding background.

6. Gravitational Waves from Domain Wall Networks

The discovery of gravitational waves using the ground-based LIGO and Virgo observatories [205, 206] has opened a new window into the cosmos. Gravitational radiation allows us to probe the dynamics of extreme astrophysical events, such as binary black hole mergers and neutron star collisions. In addition to these resolved sources, however, there is a stochastic gravitational wave background that arises from the cumulative effect of numerous unresolved and independent sources distributed across the universe. Pulsar Timing Arrays, operating in the nanohertz frequency band, have recently announced its detection for the very first time [34–36] and upcoming observatories, such as the Einstein telescope and the space-borne LISA constellation of satellites, will enable us to probe this background at higher frequencies.

Various astrophysical and cosmological phenomena — such as supermassive black holes, inflation, cosmic strings, phase transitions (see e.g [207, 208]) — are predicted to generate stochastic gravitational wave backgrounds. These signals carry information about the sources that originated them and may then enable us to unveil the fundamental processes that shaped the early universe. The observed background is likely to have been generated by several of these sources and understanding each of these contributions is therefore essential in order to use the observational data to its full potential as a probe of the underlying physics.

In the first part of this chapter, we develop a semi-analytical framework to describe the power spectrum of the Stochastic Gravitational Wave Background produced by standard and biased domain wall networks, using the Velocity-dependent One-Scale model to compute the cosmological evolution of their characteristic scale and root-mean-squared velocity. This work is based on our publication [4]. In section 6.2 (which is based on our article [3] that is currently undergoing peer review), we apply this framework we developed to study the compatibility of biased domain wall scenarios with current gravitational wave data.

6.1. A New Framework to Calculate the SGWB by Domain Walls

Current studies [32, 131, 134, 135, 209–211] of the Stochastic Gravitational Wave Background (SGWB) generated by domain wall networks are based on a model inferred from the field theory simulations of [32]. Therein, the total energy density in Gravitational Waves (GWs) and their spectrum is measured in lattice simulations and, under certain assumptions (that we will later discuss in more detail) a model for the full spectrum is built. As we discussed, lattice simulations, however, have limitations: their dynamical range and resolution are severely limited. Moreover, since the thickness of moving walls is Lorentz contracted, the resolution of the walls is also lost in the relativistic limit, which leads to an artificial decrease of their velocity through the emission of scalar radiation [197, 198]. This is precisely the limit in which significant GW emission is expected to occur, and so this loss of resolution suggests that the measurement of GWs in these simulations may produce inaccurate results.

Here, we will follow a different approach and develop a semi-analytical framework to study the SGWB produced by frictionless domain walls. Semi-analytical models have been highly successful in predicting the SGWB generated by cosmic strings [127–129, 194, 212–214] and in reproducing, after calibration, the results of numerical simulations [39, 215]. Moreover, these semi-analytical frameworks have the advantage of being very versatile, enabling, for instance, the study of non-standard cosmological and defect scenarios [123, 125, 216].

To model the scaling behavior of networks, we will use the standard VOS model (cf. section 2.2). In particular, we will estimate the rate of energy lost by the network at each time via Eqn. (4.27). To quantify our results, we will work with the unique calibration $\tilde{c} = 0.5$ and $k_w = 1.1$ as given in [158], which provides an overall fit for the radiation-, matter- and dark-energy-dominated eras. Note that, although numerical simulations [159] and our results obtained in chapter 4, as well as other semi-analytical studies [2, 167, 195] indicate that the calibration of these parameters is not unique and should, in fact, depend on the expansion rate, this single calibration actually provides accurate results since we will only consider a radiation + ΛCDM background. We will mostly focus on the cosmologically most relevant cases of radiation and matter domination (corresponding to a value of λ of $1/2$ and $2/3$ respectively). We will use a subscript ‘r’ or ‘m’ to refer to the values of the corresponding variables in the radiation and matter eras respectively, and we define $\mathcal{A}_\lambda \equiv \tilde{c}\bar{v}_\lambda/\xi_\lambda^2$. Furthermore, we will write the time evolution of the scale factor

as $a(t)/a_0 = \mathcal{C}_\lambda t^\lambda$ where $\mathcal{C}_\mathrm{r} \equiv \mathcal{C}_{1/2} = [4H_0^2\Omega_\mathrm{r}]^{1/4}$, $\mathcal{C}_\mathrm{m} \equiv \mathcal{C}_{2/3} = [(9/4)H_0^2\Omega_\mathrm{m}]^{1/3}$ and a_0 is the value of the scale factor at present time.

Note that during the transition between the radiation- and matter-dominated eras the network temporarily leaves the scaling regime. The matter era, however, does not last long enough for scaling to be fully re-established before the onset of dark energy. Nevertheless, our results will show that assuming a matter-era scaling regime until the present time provides an excellent approximation for our purposes.

6.1.1 Basic Assumptions on the Emission of Gravitational Waves

Domain wall networks have been extensively studied using field theory numerical simulations [156–159, 165, 217, 218] and these show that collisions and intersections between walls associated to different domains are quite rare. This means that such collisions cannot be expected to give rise to a significant contribution to the SGWB. In fact, the evolution of the network is mainly determined by the collapse of increasingly large sub-horizon sized domains under the effect of their tension. As these walls collapse, they evaporate and no longer contribute to the energy budget of the network. In the last stages of collapse, however, walls accelerate to ultra-relativistic velocities and should then be expected to emit gravitational- as well as scalar radiation in the process. Here, we will take into account that *the SGWB generated by domain walls is expected to be sourced by collapsing domains* rather than by the relatively slow-moving super-horizon sized walls that are still part of the network. Note that, although ultra-relativistic velocities may also sometimes be reached on highly curved regions on super-horizon walls — which would also naturally lead to an energy loss —, this process is akin to the collapse of sub-horizon domains and may thus be described similarly.

Since simulations show that the collapse of sub-horizon sized walls is a relatively quick process, occurring on timescales comparable to or shorter than one Hubble time, we will also assume that *domain walls decay effectively immediately on a cosmological timescale* once they detach from the Hubble flow. In this case, by drawing an analogy to small cosmic string loops [129] (which also evaporate almost instantaneously on cosmological timescales), we assume that the gravitational radiation is generated instantaneously by the collapsing walls. Assuming that a constant fraction $\mathcal{F} \leq 1$ of the total energy lost by the network is converted into gravitational radiation, the rate of emission of GWs at a time t measured by an observer at a time t_f is given by

$$\frac{d\rho_{\rm gw}}{dt} = \mathcal{F}\left.\frac{d\rho}{dt}\right|_{\rm loss}\left(\frac{a(t)}{a_{\rm f}}\right)^4 , \tag{6.1}$$

where $a_{\rm f} = a(t_{\rm f})$ and we have included the dilution caused by the expansion of the background.

Although Eqn. (6.1) is sufficient to determine the total energy density in GWs, to fully characterize the SGWB spectrum one also needs to know how this energy is distributed in frequency. Following [129], this may be achieved by resorting to a Probability Density Function (PDF) $p(f)$. The spectral energy density in GWs measured at a time $t_{\rm f}$ is then given by:

$$\frac{d\rho_{\rm gw}}{dtdf} = \frac{d\rho_{\rm gw}}{dt}p(f)\,. \tag{6.2}$$

The exact shape of $p(f)$ is unknown, but there are a few well-motivated assumptions that can be made about it. Since the emission of gravitational radiation can either be sourced by domains once they become relativistic in the final stages of collapse or by regions of high curvature on their surface, we can define a maximal radius of curvature $R_{\rm max}$ for GW emission. Here, we will assume that *this maximum radius is proportional to the characteristic length of the network:* $R_{\rm max}(t) = \alpha L(t)$*, where* $\alpha \lesssim 1$ *is a constant*. We will also assume that *the minimum frequency of the GWs at the time of emission* $f_{\rm min[e]}$ *is equal to* $f_{\rm min[e]} = 2/R_{\rm max}$. As we do not expect significant emission of gravitational radiation from wall segments with a curvature radius larger than $R_{\rm max}$, we will assume that there is a minimal frequency $f_{\rm min}$ associated with it below which the emission of GWs can be neglected. An observer at $t_{\rm f}$ then measures a minimal frequency of

$$f_{\rm min}(t) = f_{\rm min[e]}(t)\frac{a(t)}{a_{\rm f}} = \frac{2}{R_{\rm max}(t)}\frac{a(t)}{a_{\rm f}} = \frac{2}{\alpha L(t)}\frac{a(t)}{a_{\rm f}}\,, \tag{6.3}$$

where we have used the fact that $f(t_{\rm f}) = (a(t)/a_{\rm f})f_{\rm e}$.

The simplest PDF one may assume is a Dirac-δ function of the form:

$$p(f) = \delta(f - f_{\rm min})\,, \tag{6.4}$$

which corresponds to the unrealistic assumption that the gravitational radiation emitted by a collapsing domain wall has a frequency exactly given by $f_{\rm min}$. However, as a wall emits GWs, its energy should decrease until they eventually evaporate (although here we assume that this happens effectively immediately), so in general we should expect walls

to emit GWs with frequencies $f \geq f_{\rm min}$. By again drawing an analogy with small cosmic string loops, we would write [129]:

$$p(f) = p(R) \left| \frac{dR}{df_{\rm e}} \right| \frac{df_{\rm e}}{df} \theta(f - f_{\rm min}) \,, \tag{6.5}$$

where $f_{\rm e}$ is the emitted frequency, θ is the heaviside step function, $R \propto \sqrt{E}$ where E is the domain wall energy, and $p(R) = dE/dR \propto R$. Assuming that $f_{\rm e} = 2/R$, its distribution should be such that $p(f) \propto f^{-3}\theta(f - f_{\rm min})$. Note however that cosmic string loops survive for several oscillations while emitting GWs, which makes the distribution of energy in frequency during the evaporation process easier to predict. For domain walls this is not the case: due to their higher dimensionality, walls will in general self-intersect and evaporate upon first collapse without executing a quasi-periodical motion. This means that this direct generalization of the results of cosmic string loops would be questionable and that understanding what happens in these final stages of collapse (by means of numerical simulations) is crucial to determine the PDF. Given this, we will assume a more general power-law PDF that allows for the emission of frequencies larger than $f_{\rm min}$ with some arbitrary power f^{ν}:

$$p(f) = -\frac{\nu + 1}{f_{\rm min}^{\nu+1}} f^{\nu} \theta(f - f_{\rm min}) \,. \tag{6.6}$$

Here we shall treat ν as a free parameter with the only limitation that $\nu < -1$, in order for the PDF to be normalizable. In fact, as one can easily verify, Eqn. (6.6) fulfills the condition $\int_0^\infty p(f) df = 1$.

6.1.2 Energy Density in Gravitational waves

In this section, before venturing into a full characterization of the SGWB spectrum generated by domain walls, we study how the total energy density of GWs is expected to evolve in a cosmological background. This study can be performed with minimal assumptions, just requiring that a constant fraction of the energy lost by the network goes into GWs (no assumptions regarding its distribution in frequency are necessary). The results presented here, then, are quite general and should therefore help clarifying the potential role of domain walls as contributors to the SGWB.

Assuming a power-law evolution of the scale factor and that the domain wall network is in the corresponding linear scaling regime, Eqn. (6.1) may be rewritten as:

$$\frac{d\rho_{\rm gw}}{dt} = \mathcal{A}_\lambda \mathcal{F} \sigma \frac{t^{4\lambda - 2}}{t_{\rm f}^{4\lambda}} \,. \tag{6.7}$$

The total energy density in GWs measured by an observer at a time t_f is, for $\lambda \neq 1/4$, then given by:

$$\rho_\mathrm{gw}(t_\mathrm{f}) = \int_{t_\mathrm{i}}^{t_\mathrm{f}} \frac{d\rho_\mathrm{gw}}{dt} dt = \sigma \frac{\mathcal{F}}{t_\mathrm{f}} \frac{\mathcal{A}_\lambda}{4\lambda - 1} \left[1 - \left(\frac{t_\mathrm{i}}{t_\mathrm{f}} \right)^{4\lambda - 1} \right] \tag{6.8}$$

while, for $\lambda = 1/4$, we have

$$\rho_\mathrm{gw}(t_\mathrm{f}) = \sigma \frac{\mathcal{F}}{t_\mathrm{f}} \mathcal{A}_{\frac{1}{4}} \log \left(\frac{t_\mathrm{f}}{t_\mathrm{i}} \right) , \tag{6.9}$$

where we have assumed that the emission of GWs starts at a time $t = t_\mathrm{i}$. In figure 6.1, the evolution of the energy density of gravitational radiation for different expansion rates is plotted assuming a constant $\mathcal{F}$. Therein, it is shown that for $\lambda > 0$, after a short period of fast growth, the GW energy density decreases over time. In fact, by analyzing Eqn. (6.8), one can show that, asymptotically, $\rho_\mathrm{gw} \propto t_\mathrm{f}^{-1}$ for $\lambda > 1/4$ (which includes the cosmologically relevant radiation and matter backgrounds) and $\rho_\mathrm{gw} \propto t_\mathrm{f}^{-4\lambda}$ for $\lambda < 1/4$, while $\rho_\mathrm{gw} \propto \log(t_\mathrm{f})/t_\mathrm{f}$ for $\lambda = 1/4$. When $\lambda = 1/4$, the energy density of a domain

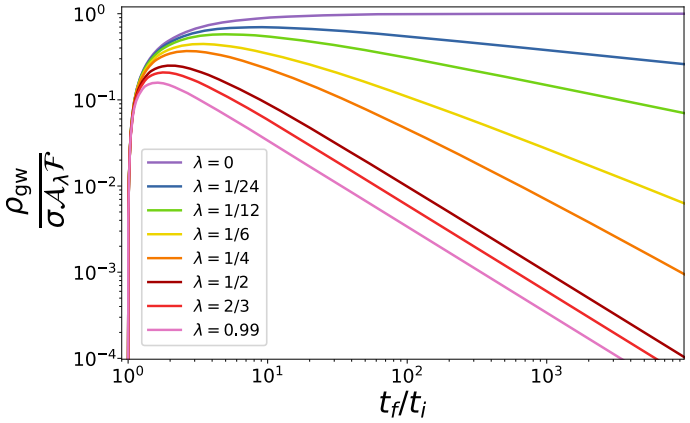

Figure 6.1: Evolution of the total energy density of gravitational waves generated by a domain wall network for different expansion rates λ. Here, we assume that $\mathcal{F}$ is a constant and a power-law expansion of the cosmological scale factor, such that $a \propto t^\lambda$.

wall network, in a linear scaling regime, scales as $\rho \propto a^{-4}$, which exactly counteracts the dilution caused by the expansion of the background. For faster expansion rates, then, this dilution is very efficient and ρ_gw is essentially dominated by the last GWs emitted. For $\lambda < 1/4$, dilution is quite slow and the gravitational radiation emitted in the initial stages of evolution of the network still contributes significantly to ρ_gw at the time of observation t_f. Interestingly, although in a non-expanding background ($\lambda = 0$) ρ_gw grows with time, one has that, for $t_\mathrm{f} \gg t_\mathrm{i}$, $\rho_\mathrm{gw} \to \mathcal{A}_0 \mathcal{F}/t_\mathrm{i}$ and remains roughly constant over time. This is explained by the fact that, in a linear scaling regime, the network becomes less dense over time and thus the energy lost by the network is smaller and smaller as time goes by. In an

expanding background, the combination of this overall decrease in the rate of emission of gravitational waves with the dilution caused by expansion means that the total energy density of gravitational radiation should asymptotically decrease over time. As a matter of fact, as illustrated in figure 6.1, this decreasing regime is reached faster for larger λ and, as a result, a smaller $\rho_{\rm gw}$ is measured at all times by observers in backgrounds with faster expansion rates.

Although these results were derived assuming that a constant fraction of the energy lost by the network goes into GWs, its main conclusion — namely that the total energy density of gravitational radiation generated by a domain wall network decreases over time in an expanding universe, after a relatively short-lived initial increase — should hold quite generally. It is straightforward to show that having an increasing or constant GW energy density necessarily requires that the fraction of the energy lost by the network that is converted into gravitational radiation grows over time as $\mathcal{F} \propto t^s$, with $s \geq 1$. However, one such scenario could only be transient as the energy density that goes into GWs naturally cannot exceed the energy lost by the network (notice that $\mathcal{F} \leq 1$ should be verified at all times). On the other hand, assuming a decreasing $\mathcal{F}$ would necessarily lead to a faster decrease of $\rho_{\rm gw}$ over time than in the constant $\mathcal{F}$ case.

Let us now consider a biased domain wall network that decays at a time $t_\star$ for which $a_\star = a(t_\star)$. The total GW energy density generated by the scaling domain wall network (ignoring, for now, the emission of gravitational waves during the decay of the network itself), in units of the critical density $\rho_{\rm crit} = 3H_0^2/(8\pi G)$, measured by an observer at the present time is given by:

$$\left.\frac{\rho_{\rm gw}^{\rm r}}{\rho_{\rm crit}}\right|_{t=t_0} = \frac{16}{3}\pi\mathcal{F}G\sigma\frac{\Omega_{\rm r}^{1/2}}{H_0}\mathcal{A}_{\rm r}\left(\frac{a_\star}{a_0}\right)^2 , \tag{6.10}$$

for $a_\star < a_{\rm eq}$, where $a_{\rm eq} = a(t_{\rm eq})$ and $t_{\rm eq}$ is the time of radiation-matter equality and we have assumed that GW emission started at a time $t_{\rm i} \ll t_{\rm f}$, and

$$\begin{aligned}\left.\frac{\rho_{\rm gw}^{\rm m}}{\rho_{\rm crit}}\right|_{t=t_0} &= \frac{16}{3}\pi\mathcal{F}G\sigma\frac{\Omega_{\rm r}^{5/2}}{H_0\Omega_{\rm m}^2}\mathcal{A}_{\rm r} + \\ &+ \frac{12}{5}\pi\mathcal{F}G\sigma\frac{\Omega_{\rm m}^{1/2}}{H_0}\mathcal{A}_{\rm m}\left(\frac{a_\star}{a_0}\right)^{5/2}\left[1-\left(\frac{a_{\rm eq}}{a_\star}\right)^{5/2}\right] ,\end{aligned} \tag{6.11}$$

for $a_\star \geq a_{\rm eq}$. In both cases, one may see that the fractional contribution of the GWs

emitted by domain walls to the energy density is a growing function of $t_\star$ (assuming that the other parameters are fixed). This is explained by the fact that the ratio between the energy density of domain walls and the background density rapidly grows with time both in the radiation and matter eras, and thus $\rho_{\rm gw}$ is dominated by late-time GW emissions.

Let us consider stable walls that survive until the present day. The gravitational waves generated during the radiation era provide a contribution to the energy density of the universe at the present time of

$$\left.\frac{\rho_{\rm gw}^{\rm r}}{\rho_{\rm crit}}\right|_{t=t_0} \frac{\sigma_{\rm Z}}{\mathcal{F}\sigma} = \mathcal{O}(10^{-14})\,, \tag{6.12}$$

where we have introduced $\sigma_{\rm Z} = (10^6\,{\rm eV})^3$ which corresponds to the mass of the heaviest walls that are still compatible with the Zel'dovich bound (cf. section 2.4). On the other hand, considering gravitational wave emission during the matter dominated era, the fractional contribution is significantly larger:

$$\left.\frac{\rho_{\rm gw}^{\rm m}}{\rho_{\rm crit}}\right|_{t=t_0} \frac{\sigma_{\rm Z}}{\mathcal{F}\sigma} = \mathcal{O}(10^{-6})\,. \tag{6.13}$$

This means that the GWs generated by stable domain walls compatible with the current CMB bounds [103] provide, at most, a relative contribution of 10^{-6} to the total energy density of the universe, which indicates that, in general, we should not expect GW constraints on σ to lead to significant improvements over the Zel'dovich bound. As a matter of fact, such a contribution would only arise in the unrealistic scenario in which all the energy lost by the network goes into GWs (i.e. $\mathcal{F}$= 1) and, quite generally, this amplitude can be significantly suppressed for a smaller efficiency of GW emission $\mathcal{F} \ll 1$. We will analyze these constraints in more detail in section 6.2.

6.1.3 Spectrum of the Stochastic Gravitational Wave Background

In this section, we will perform the full numerical characterization of the SGWB generated by domain wall networks in a ΛCDM background and develop an accurate analytical approximation to describe these results. This SGWB may be characterized by the spectral density in GWs in units of $\rho_{\rm crit}$, given by

$$\Omega_{\rm gw}(f) = \frac{1}{\rho_{\rm crit}} \frac{d\rho_{\rm gw}}{d\log f} = \frac{f}{\rho_{\rm crit}} \int_{t_{\rm i}}^{t_{\rm f}} \frac{d\rho_{\rm gw}}{dt df} dt \,. \tag{6.14}$$

Here $t_{\rm f} = \min(t_\star, t_0)$ and $t_{\rm i}$ denotes the time in which significant GW emission starts. Here, as is usually done for cosmic strings, we will assume that $t_{\rm i}$ corresponds to the time in which friction becomes negligible to the dynamics and not the time of creation of the domain wall network*. The SGWB generated by domain walls measured at the present time may then be found by setting $a_{\rm f} = a_0$ in Eqn. (6.1) and integrating Eqn. (6.2).

6.1.4 Full Numerical Computation in a ΛCDM Background

To fully characterize the SGWB spectrum produced by domain wall networks in a ΛCDM background, as a first step, we start by solving numerically the VOS Eqs. (2.16) and (2.17), coupled to the Friedmann equation, in order to get the realistic evolution of $L(t)$ and $\bar{v}(t)$. This enables us to compute the energy lost by domain wall networks throughout their evolution in a realistic cosmological background.

Let us first consider the case in which $p(f)$ is given by the δ-function in Eqn. (6.4). In this case, the integration in Eqn. (6.14) yields a spectrum of the form:

$$\Omega_{\rm gw}(f) = \frac{\pi \tilde{c} \mathcal{F} G \sigma}{6 H_0^2} \frac{\bar{v}(t_{\rm min}) L(t_{\rm min})^2}{H(t_{\rm min})} (\alpha f)^4 \theta \left(f - f_{\rm min}(t_\star) \right) \,. \tag{6.15}$$

Here we introduced $t_{\rm min}(f)$, defined as the time at which f equals the minimal frequency defined in Eqn. (6.3): $f = f_{\rm min}(t_{\rm min})$. Note that a $t_{\rm min}(f)$ that is larger than $t_\star$ corresponds to frequencies that are too low to be emitted by the network before its decay. We therefore expect a cut-off to the spectrum at the frequency $f = f_{\rm min}(t_\star)$. The resulting SGWB is plotted in figure 6.2 for $t_\star \geq t_0$, which corresponds to domain walls that survive until the present time. Therein one may see that this spectrum peaks at a frequency of $\alpha f \approx 10^{-18}\,{\rm Hz}$, corresponding to that of the gravitational radiation emitted by domain walls collapsing at late times. A lower value of α will shift the spectrum towards higher frequencies, without affecting its shape. The spectrum falls off steeply for frequencies larger

*Note however that since the largest contribution to the SGWB comes from later cosmological times, the choice of $t_{\rm i}$ should not have a significant impact on observational constraints derived using our results.

than the peak frequency, until it smoothly transitions to a flatter — but still rapidly decreasing — part that corresponds to the GWs emitted in the radiation era. Notice also that the frequency of peak of the spectrum is always determined by the last GWs emitted and so, for $t_\star < t_0$, the peak of the spectrum would appear at larger frequencies determined by the characteristic length of the network at $t_\star$ (as we shall see in the next sections). We will discuss the case of a δ-shaped PDF in more detail in section 6.1.5.

If we now consider the more general probability density function in Eqn. (6.6), the GWs are emitted with frequencies $f \geq f_{\rm min}$. This means that, for any frequency f, the SGWB will only have contributions from the domains that have decayed after $t_{\rm min}(f)$. We may then write the spectrum $\Omega_{\rm gw}(f)$ as:

$$\begin{aligned} \Omega_{\rm gw}(f) &= -(\nu+1)\frac{8\pi G}{3H_0^2}\mathcal{F}\tilde{c}\sigma\left(\frac{\alpha f}{2}\right)^{\nu+1} \\ &\times \int_{t_{\rm min}}^{t_{\rm f}}\left(\frac{a(t)}{a_0}\right)^{3-\nu}\bar{v}(t)L(t)^{\nu-1}dt\,. \end{aligned} \tag{6.16}$$

Figure 6.2 shows the SGWB generated by domain walls with $t_\star \geq t_0$ in a radiation + ΛCDM background for this more general PDF and for different values of the spectral index ν. The key feature of this spectrum is also a peak at the low-frequency end, corresponding to walls decaying late into the matter era — its position is also roughly given by $\alpha f \approx 10^{-18}\,{\rm Hz}$ if $t_\star \geq t_0$, but should appear at higher frequencies if the network decays earlier in cosmic history. However, an increase in ν represents a power shift towards higher frequencies and is thus associated with a decrease of the peak amplitude. In fact, the amplitude vanishes asymptotically in the $\nu \to -1$ limit. For smaller values of ν, on the other hand, the spectrum becomes steeper and asymptotically approaches that produced by the Dirac-δ PDF in Eqn. (6.15) in the $\nu \to -\infty$ limit, as this corresponds to concentrating all the energy produced by the network at any given time around $f_{\rm min}$. Moreover, as before, a smaller value of α will shift the spectrum to higher frequencies, without affecting its shape. Naturally, as will be shown in more detail later in this section, if the domain walls are biased and decay before the present time, the spectrum would have a cut-off at a frequency $f_{\rm min}(t_\star)$ and, therefore, the peak would appear at higher frequencies.

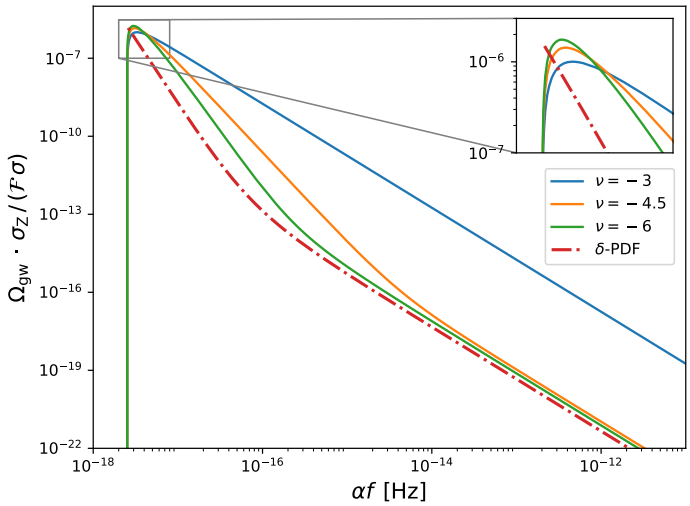

Figure 6.2: Stochastic Gravitational Wave Background generated by domain walls that survive until the present time. Here, $\Omega_{\rm gw}(f)$ is determined numerically as prescribed in Eqn. (6.16) for different values of ν (solid lines). The spectrum resulting from the Dirac-δ PDF, as given in Eqn. (6.15), is also plotted (dash-dotted line). The vertical axis is re-scaled by a factor of $\sigma_{\rm Z}/(\mathcal{F}\sigma)$, so that the spectra correspond to domain walls with $\sigma = \sigma_{\rm Z}$ (saturating the Zel'dovich bound) and a maximum efficiency of gravitational wave emission of $\mathcal{F} = 1$. The frequency on the horizontal axis is re-scaled by α, since a lower value of α will merely shift the spectrum towards higher frequencies.

6.1.5 Analytical Approximation to the Domain Wall SGWB

Assuming a power-law evolution for the scale factor and that the domain wall network is in a linear scaling regime — which, as we discussed, is a good approximation deep into the radiation and matter eras — it is possible to obtain an analytical approximation for the SGWB generated by domain wall networks that survive until a time $t_\star$. As we will show, this analytical approximation not only provides an excellent fit for the spectrum obtained numerically — thus enabling a simpler and faster computation — but also aids in understanding better its shape.

The following spectrum is obtained if $p(f)$ is given by a δ-function as in Eqn. (6.4):

$$\Omega_{\rm gw}(f) = \mathcal{A}_\lambda \mathcal{F} \mathcal{C}_\lambda^4 \frac{8\pi G\sigma}{3H_0^2(1-\lambda)} \left(\frac{\alpha\xi_\lambda f}{2\mathcal{C}_\lambda}\right)^{\frac{4\lambda-1}{\lambda-1}} \theta\left(f - f_{\rm min}(t_\star)\right) , \tag{6.17}$$

where we have $\mathcal{A}_{\rm r} = 0.102$ and $\xi_{\rm r} = 1.53$ during the radiation era and $\mathcal{A}_{\rm m} = 0.064$, $\xi_{\rm m} = 1.62$ for the matter era. The spectrum given in Eqn. (6.17) is shaped as a power-law, scaling proportionally to f^{-5} in the matter era and f^{-2} in radiation domination. As the GWs emitted during the matter era correspond to the low frequency part of the spectrum, while higher frequencies are emitted in the radiation era, this result is consistent with the general shape of the spectrum obtained numerically (as plotted in figure 6.2). We will return to this result later in this section.

Walls Decaying in the Radiation Era Let us now consider the case of the PDF in Eqn. (6.6) and consider domain walls that disappear, due to the effect of bias, at some time $t_\star < t_{\rm eq}$. In this case, assuming scaling, it is possible to obtain an explicit expression for $t_{\rm min}(f)$ — which yields $t_{\rm min} = [2\mathcal{C}_{\rm r}/(\alpha\xi_{\rm r} f)]^2$ — and to use it to perform the integration in Eqn. (6.14) analytically. We find

$$\begin{aligned}\Omega^{\rm r}_{\rm gw}(f, a_\star, \nu) &= \frac{32\pi}{3}\frac{\nu+1}{\nu+3}\mathcal{F}G\sigma\frac{\Omega_{\rm r}^{1/2}}{H_0}\mathcal{A}_{\rm r} \\ &\times \left(\frac{\alpha\xi_{\rm r} f}{4H_0\Omega_{\rm r}^{1/2}}\right)^{-2}\left[1-\left(\frac{\alpha\xi_{\rm r} f}{4H_0\Omega_{\rm r}^{1/2}}\frac{a_\star}{a_0}\right)^{\nu+3}\right],\end{aligned} \tag{6.18}$$

which is valid for $\nu \neq \nu^{\rm r}_{\rm pole} = -3$. Note that, if $\nu > \nu^{\rm r}_{\rm pole}$, the radiation era spectrum will be dominated by the second term in Eqn. (6.18) and will therefore scale proportionally to $f^{\nu+1}$. This means that, in this limit, the SGWB is dominated by the last GWs emitted by the domain wall network over all the frequency range. On the other hand, for all values of ν smaller than $\nu^{\rm r}_{\rm pole}$, the first term in Eqn. (6.18) dominates and the spectral shape will be independent of ν, showing a power-law decay with $\Omega_{\rm gw} \propto f^{-2}$ similar to that obtained for the δ-function PDF.

For $\nu = -3$, on the other hand, we find that:

$$\begin{aligned}\Omega^{\rm r}_{\rm gw}(f, a_\star, \nu^{\rm r}_{\rm pole}) &= \frac{64\pi}{3}\mathcal{F}G\sigma\frac{\Omega_{\rm r}^{1/2}}{H_0}\mathcal{A}_{\rm r} \\ &\times \left(\frac{\alpha\xi_{\rm r} f}{4H_0\Omega_{\rm r}^{1/2}}\right)^{-2}\log\left[\frac{\alpha\xi_{\rm r} f}{4H_0\Omega_{\rm r}^{1/2}}\frac{a_\star}{a_0}\right].\end{aligned} \tag{6.19}$$

In this case, the spectrum will again scale asymptotically as f^{-2} for sufficiently high frequencies, although in this case the logarithmic term in Eqn. (6.19) results in a slightly shallower decay in the low-frequency part.

For a biased domain wall network that disappears in the radiation era, the SGWB spectrum peaks at a frequency

$$\alpha f^{\rm r}_{\rm peak} = \begin{cases} \frac{4H_0\Omega_{\rm r}^{1/2}}{\tilde{\zeta}_{\rm r}}\left[-\frac{2}{\nu+1}\right]^{1/(\nu+3)}\left(\frac{a_0}{a_\star}\right), & \text{for } \nu \neq -3\,, \\ \frac{4H_0\Omega_{\rm r}^{1/2}}{\tilde{\zeta}_{\rm r}}{\rm e}^{1/2}\frac{a_0}{a_\star}, & \text{for } \nu = -3\,, \end{cases} \tag{6.20}$$

which corresponds to a peak amplitude of

$$\Omega^{\rm r}_{\rm peak} = \frac{32\pi}{3}\mathcal{F}G\sigma\frac{\Omega_{\rm r}^{1/2}}{H_0}\mathcal{A}_{\rm r}\left(\frac{a_\star}{a_0}\right)^2\left[-\frac{2}{\nu+1}\right]^{-2/(\nu+3)}, \tag{6.21}$$

for $\nu \neq \nu^{\rm r}_{\rm pole}$ and

$$\Omega^{\rm r}_{\rm peak} = \frac{32\pi}{3{\rm e}}G\sigma\mathcal{F}\frac{\Omega_{\rm r}^{1/2}}{H_0}\mathcal{A}_{\rm r}\left(\frac{a_\star}{a_0}\right)^2, \tag{6.22}$$

for $\nu = -3$. It is interesting to note that the amplitude of the peak, except for a factor $2[-2/(\nu+1)]^{-2/(\nu+1)}$ for $\nu \neq -3$ and $2/{\rm e}$ for $\nu = -3$, coincides with the total energy density in GWs in units of the critical density of the universe in Eqn. (6.10). These factors, except in the $\nu \to -1$ limit (in which significant power is shifted towards high frequencies) are, roughly, of order unity, which shows that, in general, the SGWB is dominated by the emission at late times. Notice that $\alpha f^{\rm r}_{\rm peak}$ scales proportionally to $a_\star^{-1}$, while $\Omega^{\rm r}_{\rm peak} \propto a_\star^2$. As a result, domain wall networks decaying earlier in the radiation era will peak at higher frequencies and will have a smaller amplitude for the same value of domain wall tension, as is shown in figure 6.4 (dashed lines). Note, however, that domain walls decaying before the time of decoupling evade the stringent Zel'dovich bound and may have significantly larger tensions and generate a strong and detectable SGWB as a result. This plot, as a matter of fact, shows that their peak may, in fact, coincide with the pulsar timing array window provided that they have decayed early enough in the radiation era. We will analyze this possibility in more detail in section 6.2.

Walls Decaying in the Matter Era For domain wall networks that survive through the radiation-matter transition and disappear at a time $t_\star \geq t_{\rm eq}$, we will assume, for simplicity, that the transition between these two eras happens suddenly at $t_{\rm eq}$. We assume then the universe to be effectively radiation (matter) dominated, with $\lambda = 1/2$ $(2/3)$ for $t < t_{\rm eq}$ $(t \geq t_{\rm eq})$ and that the network is in a scaling regime characterized by the parameters $\xi_{\rm r}$ $(\xi_{\rm m})$ and $\bar{v}_{\rm r}$ $(\bar{v}_{\rm m})$. During the matter era, $t_{\rm min} = [2\mathcal{C}_{\rm m}/(\alpha\xi_{\rm m} f)]^3$ and so the SGWB is given by*

$$\begin{aligned}\Omega_{\rm gw}^{\rm m}(f, a_\star, \nu) &= \Omega_{\rm gw}^{\rm r}(f, a_{\rm eq}, \nu) + 12\pi\frac{\nu+1}{\nu+6}\mathcal{F}G\sigma \\ &\times \frac{\Omega_{\rm m}^{1/2}}{H_0}\mathcal{A}_{\rm m}\left(\frac{\alpha\xi_{\rm m} f}{3H_0\Omega_{\rm m}^{1/2}}\right)^{-5}\left\{1-\left[\frac{\alpha\xi_{\rm m} f}{3H_0\Omega_{\rm m}^{1/2}}\left(\frac{a_\star}{a_0}\right)^{1/2}\right]^{\nu+6}\right\},\end{aligned} \tag{6.23}$$

which has a pole for $\nu \equiv \nu_{\rm pole}^{\rm m} = -6$. As was the case for the contribution of the radiation-era walls, if $\nu > \nu_{\rm pole}^{\rm m}$, this spectrum will scale proportionally to $f^{\nu+1}$, while for $\nu < \nu_{\rm pole}^{\rm m}$ we have that $\Omega_{\rm gw}^{\rm m} \propto f^{\nu_{\rm pole}^{\rm m}+1} = f^{-5}$ as in the case of the Dirac-δ PDF. For $\nu = -6$, we have an additional logarithmic dependency on the frequency just as in the radiation-dominated case:

$$\begin{aligned}\Omega_{\rm gw}^{\rm m}(f) &= \Omega_{\rm gw}^{\rm r}(f, a_{\rm eq}, \nu) + 60\pi\mathcal{F}G\sigma\frac{\Omega_{\rm m}^{1/2}}{H_0}\mathcal{A}_{\rm m} \\ &\times \left(\frac{\alpha\xi_{\rm m} f}{3H_0\Omega_{\rm m}^{1/2}}\right)^{-5}\log\left[\frac{\alpha\xi_{\rm m} f}{3H_0\Omega_{\rm m}^{1/2}}\left(\frac{a_\star}{a_0}\right)^{1/2}\right].\end{aligned} \tag{6.24}$$

In this case, the peak is located at a frequency

$$\alpha f_{\rm peak}^{\rm m} = \begin{cases}\frac{3H_0\Omega_{\rm m}^{1/2}}{\xi_{\rm m}}\left[-\frac{5}{\nu+1}\right]^{1/(\nu+6)}\left(\frac{a_0}{a_\star}\right)^{1/2}, & \text{for } \nu \neq -6, \\ \frac{3H_0\Omega_{\rm m}^{1/2}}{\xi_{\rm m}}e^{1/5}\left(\frac{a_0}{a_\star}\right)^{1/2}, & \text{for } \nu = -6,\end{cases} \tag{6.25}$$

which corresponds to a peak amplitude of

$$\Omega_{\rm peak}^{\rm m} = 12\pi\mathcal{F}G\sigma\frac{\Omega_{\rm m}^{1/2}}{H_0}\mathcal{A}_{\rm m}\left(\frac{a_\star}{a_0}\right)^{5/2}\left[-\frac{5}{\nu+1}\right]^{-5/(\nu+6)}, \tag{6.26}$$

for $\nu \neq \nu_{\rm pole}^{\rm m}$ and

*Technically, to compute the matter era contribution, the integration in Eqn. (6.14) should start at $t_{\rm i} = \max(t_{\rm min}, t_{\rm eq})$. Here, to maintain the analytical expressions presented as simple as possible, we always set $t_{\rm i} = t_{\rm min}(f)$. We found that, if $\nu < -6$, the matter-era contribution changes its slope at $f_{\rm min}(t_{\rm eq})$ and becomes steeper for $f > f_{\rm min}(t_{\rm eq})$, if one takes $t_{\rm i} = \max(t_{\rm min}, t_{\rm eq})$. However, since in this case the SGWB spectrum is dominated by the walls that decay in the radiation era in this frequency range, this has, in general, no significant impact on the final results. Note however that taking $t_{\rm i} = \max(t_{\rm min}, t_{\rm eq})$ is necessary if one is interested in computing solely the contribution of the walls that decay in the matter era.

$$\Omega_{\rm peak}^{\rm m} = \frac{12}{\rm e}\pi\mathcal{F}G\sigma\frac{\Omega_{\rm m}^{1/2}}{H_0}\mathcal{A}_{\rm m}\left(\frac{a_\star}{a_0}\right)^{5/2}, \tag{6.27}$$

for $\nu = -6$. As before, these amplitudes follow closely the total amplitude in GWs in units of the critical density in Eqn. (6.11), except for factors of $5[-5/(\nu+1)]^{-5/(\nu+6)}$ for $\nu \neq -6$ and $5/e$ for $\nu = -6$. Moreover, as in the radiation era, we may see that the later the domain wall network decays in the matter era, the lower the frequency of the peak and the stronger their signal would be (for the same tension). The maximum allowed tension of walls decaying in the matter era, however, is subject to more stringent bounds than those of walls decaying in the radiation era to avoid strong signatures on the CMB. In this case, figure 6.4 clearly shows that the SGWB generated by stable domain walls or by networks that decay in the matter era should not be detectable except for very small values of α.

6.1.6 Shape of the Full Spectrum

We may then divide the results produced by our model into three different regimes:

1. For $-3 \leq \nu < -1$, the spectra generated in the radiation- and matter-dominated eras have equal slopes. As a consequence, the spectrum will be globally dominated by walls that have decayed more recently, while the contribution from walls decaying early in the evolution of the network is negligible. This behaviour is clearly displayed in the top panel of figure 6.3, where we plot the analytical approximation to the the SGWB generated by domain walls derived here, for $\nu = -2$ and $t_\star \geq t_0$, alongside the full spectrum obtained numerically. This regime, which corresponds to having significant power emitted in higher frequencies, particularly includes the above mentioned case in which $\nu \to -1$, corresponding to a flat spectrum. However, as may be seen in the Eqs. (6.18, 6.23), the $\nu + 1$ pre-factor will lead to a suppression of the peak amplitude of the spectrum in this limit.

2. For $-6 < \nu < -3$, the radiation era spectrum scales as f^{-2}, while the matter-era contribution becomes steeper with decreasing ν. An example of the SGWB generated by walls in this regime, with $\nu = -4.5$ and $t_\star \geq t_0$, is depicted in the middle panel of figure 6.3. Therein, one may see that the contributions of the radiation and matter eras become clearly distinguishable in this regime and that, as the frequency increases, the spectrum is dominated by the GW emissions of domains emitted at progressively earlier times.

3. For all $\nu \leq -6$, the spectrum will scale proportionality to f^{-5} in matter- and f^{-2} in radiation-domination, as shown in the bottom panel of figure 6.3, where we plot the SGWB generated by domain walls with $\nu = -7$ and $t_\star \geq t_0$. In this regime, the spectrum follows very closely that obtained for a δ-shaped PDF [Eqn. (6.17)], since this corresponds to concentrating most of the GW power emitted around $f_{\rm min}$. The latter can therefore be regarded as an asymptotic limit for low values of ν, in agreement with the numerical results presented in figure 6.2.

The plots in figure 6.3 show that the analytical approximations derived here provide an excellent fit to the SGWB obtained numerically over the whole range of the spectrum and for all values of ν. This figure additionally shows the spectral index of the full numerically-obtained spectrum, defined as $d\log\Omega_{\rm gw}/d\log f$. One may see that, for the cases with a distinct scaling of the spectrum with frequency in the radiation- and matter-dominated eras, the transition between the two characteristic slopes is smooth. This is a consequence of the fact that the radiation-matter transition is a slow continuous process rather than an instantaneous one (as we have assumed for the purpose of deriving the analytical approximations). In fact, for low values of ν, the slope predicted by the analytical approximation in matter-domination is never fully reached and the spectrum will be shallower than predicted in the low-frequency regime. However, even in this case, our analytical approximation still provides a remarkably good fit to the numerical results.

Finally, it is worth noting that, with on average only about one wall existing per Hubble volume in a scaling network, the number of collapse events in the recent cosmic history should be relatively low. This raises questions regarding the stochastic nature of the gravitational wave background generated by domain walls decaying in the very recent past and this may result, in fact, in a “popcorn” signal or in individual resolvable bursts of GWs.

6.1.7 The Contribution of Bias

When bias becomes relevant to domain wall dynamics, it renders the whole network unstable and all the walls evaporate within about a Hubble time. In this process, domain walls emit further gravitational radiation and this emission should also contribute to the SGWB. We did not take this final emission into consideration in the previous sections. Here, we briefly discuss this additional contribution to the SGWB.

As was the case for the GWs emitted throughout the evolution of the network, in this case, it is not known *a priori* how much of the energy of the network is converted into gravitational radiation and how this energy is distributed in frequency in this almost instantaneous decay process. As a matter of fact, bias may have an impact on the emission of scalar radiation and the distribution of GWs in frequency may in fact be altered since, in this case, there is also a decay of super-horizon domains. Here, for simplicity and given all the unknowns, we will assume that both the PDF and $\mathcal{F}$ will be the same as in the case of the domains that collapse while the network is stable. As the final decay of a biased network occurs in roughly one Hubble time, we will assume it may be treated as instantaneous on cosmic time scales. In this approximation, all the energy stored in the network is assumed to be released at the time of decay, $t_\star$. Then, the contribution of this decay to the GW spectrum as measured today will be given by the Eqn. (6.1) and (6.2), but with the energy loss term replaced by [210]:

$$\left.\frac{d\rho}{dt}\right|_{\text{loss,bias}} = \rho\delta(t - t_\star)\,. \tag{6.28}$$

The integration of a term of this form will yield an additional contribution of the form $\Omega_{\text{gw}} \propto f^{\nu+1}$. For a network decaying in the radiation-dominated era, with $t_\star < t_{\text{eq}}$, the full spectrum may be obtained by multiplying the second term in Eqn. (6.18) by the following term:

$$\left[1 + \frac{\nu+3}{2\mathcal{A}_{\text{r}}\xi_{\text{r}}}\theta\left(f - f_{\min}(a_\star)\right)\right]. \tag{6.29}$$

As to the $\nu = -3$ case, one has to add the following term to Eqn. (6.19)

$$\frac{32}{3}\pi\mathcal{F}G\sigma\frac{\Omega_{\text{r}}^{1/2}}{H_0\xi_{\text{r}}}\left(\frac{\alpha\xi_{\text{r}}f}{4H_0\Omega_{\text{r}}^{1/2}}\right)^{-2}, \tag{6.30}$$

in order to account for the contribution of bias. If on the other hand $t_\star \geq t_{\text{eq}}$, the last term in Eqn. (6.23) should be corrected by a factor of

$$\left[1 + \frac{\nu+6}{3\mathcal{A}_{\text{m}}\xi_{\text{m}}}\theta\left(f - f_{\min}(a_\star)\right)\right], \tag{6.31}$$

for $\nu \neq -6$ and the term

$$20\pi\mathcal{F}G\sigma\frac{\Omega_{\rm m}^{1/2}}{H_0\xi_{\rm m}}\left(\frac{\alpha\xi_{\rm m}f}{3H_0\Omega_{\rm m}^{1/2}}\right)^{-5} \tag{6.32}$$

should be added to Eqn. (6.24) for $\nu = -6$.

Figure 6.4 displays examples of the full spectrum expected for a biased network decaying at different instants of time $t_\star$ (given as a fraction of the time of matter-radiation equality $t_{\rm eq}$) and for different values of ν. These plots show that the sudden decay of the network has the potential to increase the peak amplitude of the SGWB by up to one order of magnitude. This is to be expected, as the energy density in the network at any time is larger — but roughly of the same order — than the energy density lost by the network in a Hubble time. Moreover, as we have seen, the contribution of the decay of the biased network (in our simplified model) always scales as $f^{\nu+1}$. As a consequence, for $\nu \geq \nu_{\rm pole}^{\rm r}$ (the case in which the "scaling" spectrum also scales as $f^{\nu+1}$), the spectrum is globally dominated by the gravitational waves emitted during the decay of the network. This case is displayed in the top panel of figure 6.4. Besides the peak getting sharper — a consequence of assuming that the decay would happen instantaneously — this case is not distinguishable from the spectrum generated by a stable domain wall network with a larger tension σ or an increased $\mathcal{F}$ (as these would lead to an increase of the amplitude). On the other hand, for $\nu < \nu_{\rm pole}^{\rm r}$, the part of the spectrum emitted before bias comes into effect scales as f^{-2} for GWs sourced in the radiation era, as explained in section 6.1.5. This means that, for $t_\star < t_{\rm eq}$, the contribution of the decay of the network caused by bias dominates the spectrum only in a small frequency band close to the peak, while towards higher frequencies it is dominated by the contribution emitted while the network is stable. A similar situation arises for $t_\star \geq t_{\rm eq}$ when $\nu < \nu_{\rm pole}^{\rm m}$. These situations, as can be seen in the middle and bottom panels of figure 6.4, lead to a distinct, sharper peak with a different slope that becomes more pronounced the smaller ν gets, which may be regarded as a potential observational signature of bias.

As to the total energy density of gravitational radiation measured by an observer at a time $t_{\rm f}$, to account for the final collapse of the network, we need to include an additional contribution of ρ at $t = t_\star$ and to take into account that there is no emission of GWs for $t > t_\star$. We then have, for $\lambda \neq 1/4$, that:

$$\rho_{\rm gw}(t_{\rm f}) = \sigma\frac{\mathcal{F}}{t_\star}\frac{\mathcal{A}_\lambda}{4\lambda-1}\left[\left(1+\frac{4\lambda-1}{\mathcal{A}_\lambda\xi_\lambda}\right)\left(\frac{t_\star}{t_{\rm f}}\right)^{4\lambda} - \frac{t_\star}{t_{\rm i}}\left(\frac{t_{\rm i}}{t_{\rm f}}\right)^{4\lambda}\right], \tag{6.33}$$

while, for $\lambda = 1/4$, we have

$$\rho_{\rm gw}(t_{\rm f}) = \sigma \frac{\mathcal{F}}{t_f} \mathcal{A}_{\frac{1}{4}} \left[\log\left(\frac{t_\star}{t_{\rm i}}\right) + \frac{1}{\mathcal{A}_{\frac{1}{4}} \xi_{\frac{1}{4}}} \right] \tag{6.34}$$

for $t_{\rm f} \geq t_\star$, while Eqs. (6.8) and (6.9) remains valid if $t_{\rm f} < t_\star$. Assuming that $t_{\rm f} \gtrsim t_\star \gg t_{\rm i}$, the total GW energy density is enhanced by a factor of ~ 7, if bias comes into effect during the radiation era, and a factor of ~ 17 for $t_\star \geq t_{\rm eq}$. For times $t_{\rm f} > t_\star$, however, there is no new gravitational wave emission and, therefore, the energy density of gravitational radiation is merely redshifted due to expansion. Note that the enhancement factors predicted here should be taken as an upper limit since a more realistic non-instantaneous description of the decay of the wall network would necessarily lead to smaller values and to spectra with rounder peaks and a smaller maximum amplitude. Also, we have ignored the potential impact of bias on $\mathcal{F}$ and the PDF as this is currently unknown, but if these are significantly impacted this contribution would be significantly affected too.

6.1.8 Comparison With Previous Computations

The shape of the SGWB generated by domain wall networks computed here is different from other predictions in the literature [32, 131, 134, 135, 209–211]. These predictions all stem from the results of Ref. [32], wherein the spectrum of GWs is measured in field theory simulations of domain wall networks (see also [33, 219–221] for earlier estimates and [222] for a review). In [32], the authors propose a broken power-law shape for the spectrum, with the peak located at a frequency $f_{\rm peak}$ corresponding to the horizon scale at the time of disappearance of the network, if walls are biased, or the present time for standard walls. For $f > f_{\rm peak}$, simulations indicate that $\Omega_{\rm gw} \propto f^{-1}$ in the radiation era — which would correspond to a PDF for GW emission with a spectral index of $\nu = -2$ in our case — however the authors state that the exact dependence of $\Omega_{\rm gw}$ on f is not straightforward to estimate. For $f < f_{\rm peak}$, the dependence of $\Omega_{\rm gw}$ on f was not accurately determined in the simulations and the authors claim that causality requires that $\Omega_{\rm gw} \propto f^3$, as was shown to be the case for the SGWB generated by bubble collisions in first order phase transitions [223] (see however [224, 225]). Here, we obtained a much steeper spectrum for $f < f_{\rm peak}$ — as is, in fact, also found for the SGWB generated by cosmic strings [127–129], especially for fast-decaying small cosmic string loops [129] — and this steepness is a consequence of assuming that one may associate a well defined characteristic frequency to the collapsing domain walls. Note however that our predictions

for this spectrum (and the predictions for that generated by cosmic string loops in the literature) do not apply to superhorizon scales: we always consider a minimum frequency of emission that corresponds to a sub-horizon mode as, in fact, the GWs are sourced, in this case, by domains that are sub-horizon at the time of collapse. In reality, a less steep cut-off would be expected, and thus this framework cannot be expected to provide an accurate description of the spectra for frequencies smaller than that of the peak. As a matter of fact, a smooth transition towards a f^3 spectrum might be expected to occur in this regime, but the precise nature of this transition is a topic that warrants further investigation.

Our predictions for the shape of the spectrum qualitatively agree with the results in the literature for frequencies higher than that of the peak: in both cases the spectrum is dominated by the last GWs emitted and decreases as a power-law. The biggest disagreement between our predictions and those of [32] actually appears in the normalization of the spectrum. By comparing our results in Eqn. (6.21) to those therein, we find that the latter include an additional factor of $\sim G\sigma/H(t_\star)$. This factor may be quite significant and may have implications for the observational constraints derived using the results of [32]. In [32], the normalization of the spectrum is determined by assuming that the energy density in gravitational waves remains constant over time, as predicted in [33]. As we have argued in Sec. 6.1.2, this should not be the case: in an expanding background, if $\mathcal{F}$ is a constant, the total gravitational radiation energy density measured by an observer at a time t, after an initial period of quick growth, necessarily decreases as t increases. A constant GW energy density would necessarily require that the fraction of the energy lost by the network into GWs would increase over time (with $\mathcal{F} \propto t$, if linear scaling of L with cosmic time is assumed) and, as previously explained, such scenario would necessarily have to be transient since the condition $\mathcal{F} \leq 1$ must be satisfied at all times*. The measurements in Ref. [32] seem to be consistent with a constant $\rho_{\rm gw}$, and these are admittedly affected by several systematic uncertainties. In fact, these simulations are not able to resolve the dynamics of the domain walls in the ultrarelativistic regime, in which the dominant contribution of domain walls to the SGWB is expected to be generated, nor do they account for the GW backreaction that would necessarily affect domain wall dynamics, especially for values of $\mathcal{F}$ not much smaller than unity — a necessary condition for domain walls to provide a significant contribution to the SGWB background.

*Notice that, given that the domain walls will also lose energy through other channels, $\mathcal{F} = 1$ will never be attained in practice.

Our results about the evolution of $\rho_{\rm gw}$ are based on minimal assumptions: they are independent of both the characteristic scale and the spectrum of emission of GWs. The only underlying assumption is that the energy that goes into GWs is a constant fraction of that lost by the domain wall network. Although this assumption may not hold throughout the whole evolution of the network, it should be an excellent approximation during the final stages of the evolution of the domain walls, when most of the contribution to the SGWB is generated. The assumptions in [32, 33] are different, as the authors assume that the GWs are sourced by domain walls that are only mildly relativistic and that did not fully detach from the Hubble flow. Therein, following [226], the authors use the quadrupole formula to estimate the power emitted by a domain wall with a typical size of R:

$$P \sim G\sigma^2 R^8 f^6 \,. \tag{6.35}$$

Then, assuming that the frequency is determined by R, so that $f \sim R^{-1}$, one has

$$P \sim G\sigma^2 R^2 \,. \tag{6.36}$$

The energy in a volume L^3, containing a domain wall with area L^2, is then estimated in [32, 33] to be $E \sim P \cdot t \sim P \cdot L \sim G\sigma^2 L^3$, so that $\rho_{\rm gw} \sim E/L^3$ remains constant over time. This is the result that the authors use as a basis to derive the normalization of the spectra. In the last step of this derivation, the radius of the domain wall R was identified with the characteristic length L of the network and linear scaling of the network was assumed. However, *one cannot have a cake and eat it*: emission of radiation by a domain wall, in any form, would necessarily lead to a decrease of their size and, hence, the identification of R and L is questionable in this case. More formally, one would write the power emitted per unit volume by the domain wall network in the form of gravitational waves as

$$\frac{d\rho_{\rm gw[e]}}{dt} = Pn \,, \quad \text{where} \quad n = \rho/E_{\rm w} \tag{6.37}$$

is the wall number density, and $E_{\rm w}$ and P are, respectively, the average energy of a single wall and the average power emitted per wall in the form of GWs. Estimating P using the quadrupole formula, one obtains

$$P \sim G\sigma^2 L^2 \,, \tag{6.38}$$

which then implies

$$\frac{d\rho_{\mathrm{gw[e]}}}{dt} \sim \frac{G\sigma^2}{L} = \frac{\rho}{\tau}\,, \tag{6.39}$$

where $\tau = (G\sigma)^{-1}$ defines a characteristic time for the conversion of a constant fraction of the energy of the network into GWs (which for reasonable values of domain wall tension is always much larger than the age of the universe). Notice that, in this case, we are not following the evolution of a single wall and, therefore, no identification between R and L is necessary. By integrating and maintaining the assumption that the network is in linear scaling, one would in fact obtain a constant energy density. Note however that there is an underlying assumption when one proceeds this way: walls are assumed to only decay at this rather slow rate and to be extremely long-lived. This can only apply to walls that are part of the network and not to collapsing domain walls. The quadrupole formula, in fact, cannot capture what happens in the last ultra-relativistic stages of collapse and the potential bursts triggered by domain wall self-interactions which can lead to a smaller time-dependent characteristic time $\tau \propto L$ for the production of GWs (which for a scaling network would imply that $\tau \propto H^{-1}$). In this case, we would then have that the averaged power emitted per unit volume during the collapse scales proportionally to L^{-2}, precisely as predicted for the energy loss rate of the domain wall network (cf. Eqn. (4.27)). The radiation coming from the slowly moving walls that are part of the network should be subdominant when compared to that emitted in the last stages of the evolution of the many collapsing domains that exist at any time. The fact that the energy lost by a network of domain walls during its evolution is so well described by the rapid collapse of the domains that detach from the Hubble flow after entering the horizon [167] provides strong evidence for this.

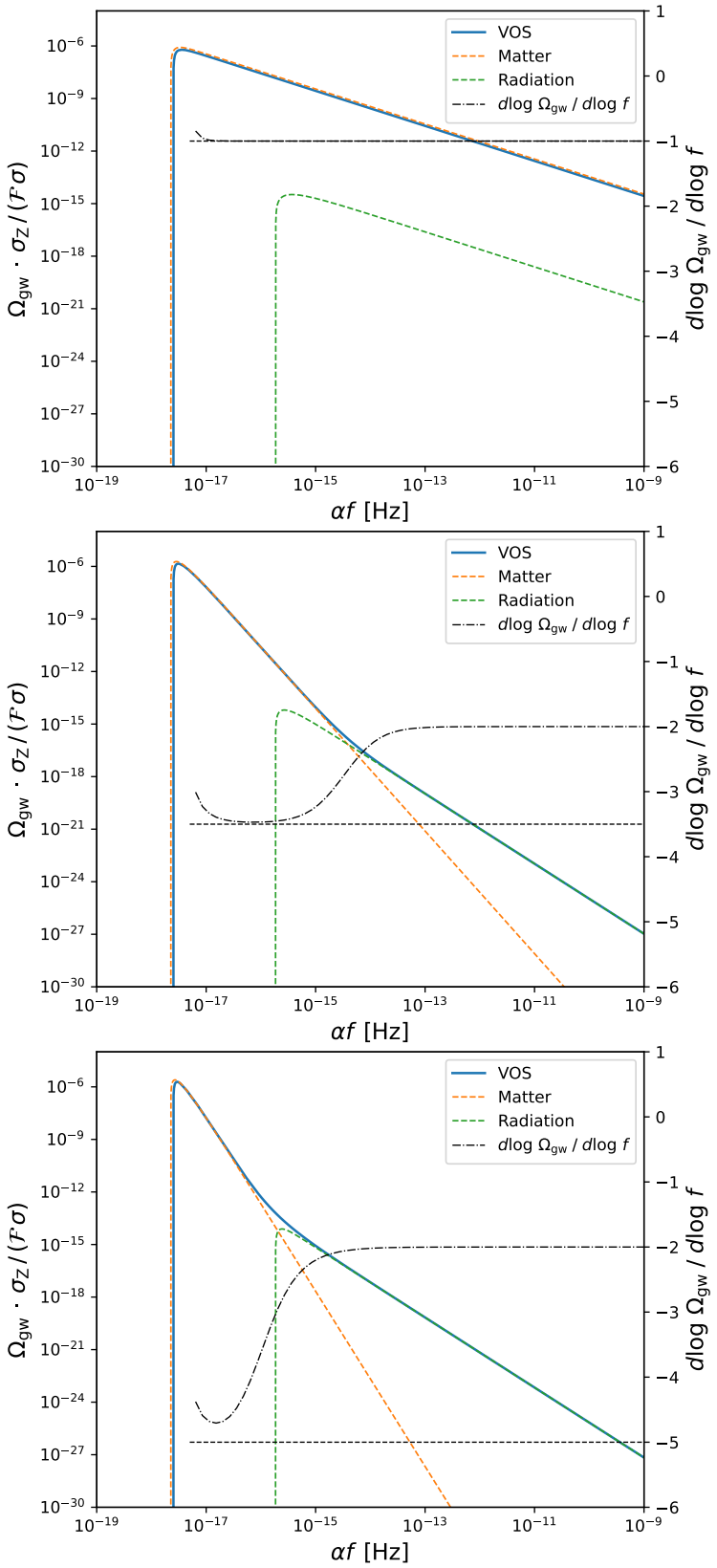

Figure 6.3: Analytical approximation to the SGWB generated by domain wall networks that decay, due to the effect of bias, at $t_\star \geq t_0$. These plots display the full spectra obtained numerically (solid lines) as well as the analytical approximations for the contributions generated during the matter (dashed orange lines) and radiation era (dashed green lines) for $\nu = -2$ (top panel), $\nu = -4.5$ (middle panel) and $\nu = -7$ (bottom panel). Each panel additionally displays the spectral index $d\Omega/d\log f$ of the numerical spectrum (dash-dotted lines) and that predicted by the analytical approximation during the matter era (black dashed line).

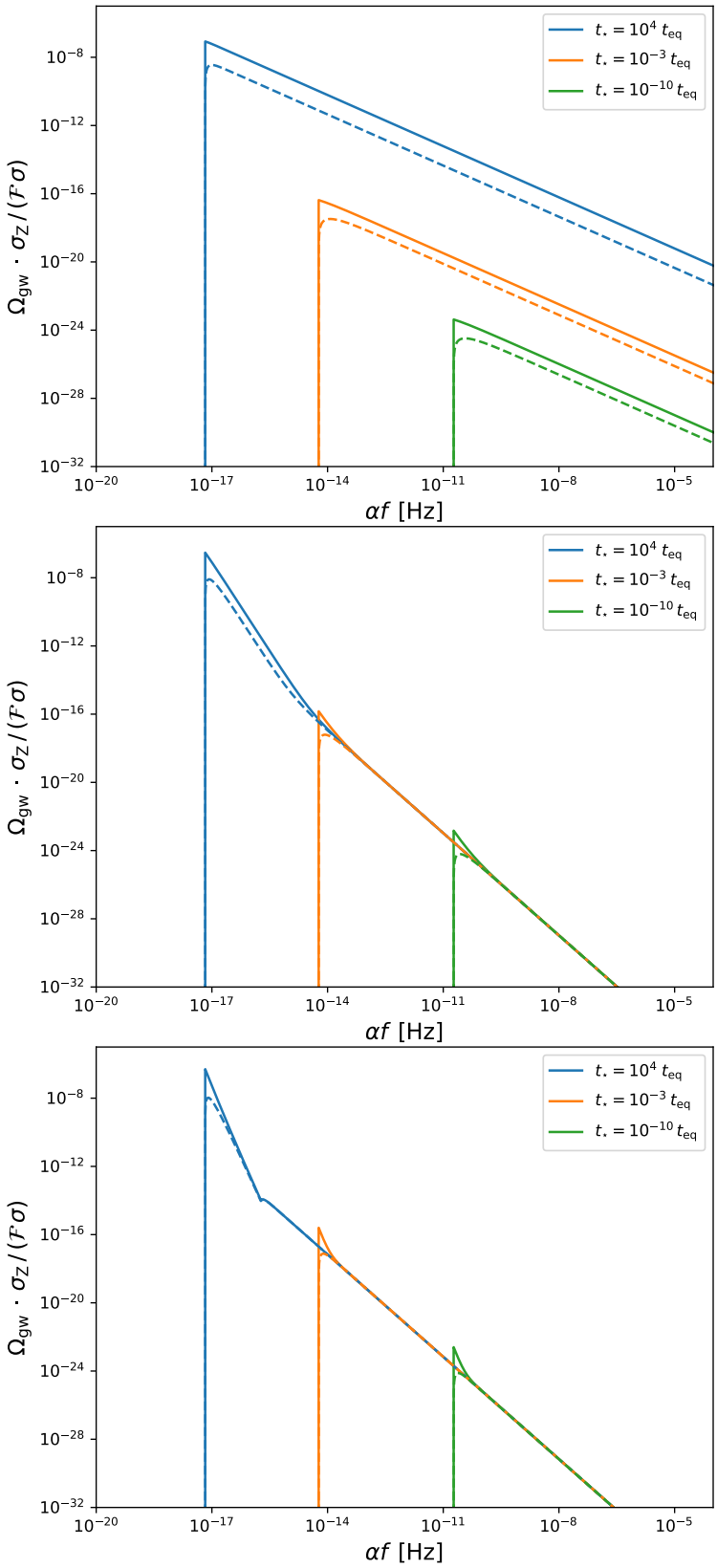

Figure 6.4: Stochastic gravitational wave background generated by biased domain wall networks. Each panel displays the analytical approximation the total SGWB spectrum generated by a biased network for different decay times $t_\star$ including the contribution of the final decay of the network (solid lines), alongside the spectrum generated by the network while it is stable up until time of decay (dashed lines). The top, middle and bottom panels correspond, respectively, to values of $\nu = -2$, $\nu = -4.5$ and $\nu = -7$.

6.2. Observational Constraints from the CMB and PTAs

In this section, we will apply the framework introduced above to current gravitational wave data. More specifically, we will use the expressions we derived for the total energy density in gravitational waves from a scaling domain wall network decaying at a time $t_\star$ (corresponding to a scale factor $a_\star$ and a redshift $z_\star = a_\star^{-1} - 1$) to constrain the characteristic energy scale $\eta \equiv \sigma_0^{1/3}$ at the time of domain wall formation.

For simplicity, in the previous section and in chapter 1, we have neglected the fact that, as the universe expands and cools, the effective number of relativistic degrees of freedom decreases, as its temperature drops below the mass scale of the standard model particles. This has an impact on the expansion rate on the cosmological background and, in order to derive accurate constraints, one needs to include this effect. Here, we follow the approach in reference [122] and modify the Friedmann equation in Eqn. (1.10) as follows

$$H(z) = H_0 \left[\Omega_\Lambda + \Omega_{\rm m}(1+z)^3 + \mathcal{G}(z)\Omega_{\rm r}(1+z)^4\right]^{1/2}, \tag{6.40}$$

where

$$\mathcal{G}(z) = \begin{cases} 1 & \text{for } z < z_{e^-e^+} \\ 0.83 & \text{for } z_{e^-e^+} < z < z_{\rm QCD} \\ 0.39 & \text{for } z > z_{\rm QCD} \end{cases} \tag{6.41}$$

describes the decreases in the number of degrees of freedom expected to occur, in the Standard Model of Particle Physics, at the QCD phase transition and as a result of the electron-positron annihilation (throughout this paper we shall take $z_{e^-e^+} = 10^9$ and $z_{\rm QCD} = 10^{12}$ [122]). This factor is responsible for a suppression of the fractional contribution of the gravitational waves emitted by domain wall networks to the cosmic energy budget, which we will account for by multiplying the RHS of Eqns. (6.10, 6.11) by a factor of $\mathcal{G}_\star^{1/2} \equiv \mathcal{G}(z_\star)^{1/2}$.

Notice that, throughout this section, we shall assume that the network is in a linear scaling regime before it is rendered unstable and instantaneously decays without producing further GWs. Including the potential contribution of the decay of the network to the SGWB could — as we have seen — increase its amplitude by up to an order of magnitude (but there is still some uncertainty regarding this contribution).

As we have seen, the power spectrum of the SGWB generated by domain walls can be roughly approximated by a broken power-law shape, with the power being a monotonically

increasing (decreasing) function of the frequency for frequencies smaller (larger) than the peak frequency (this applies to both, our framework described above as well as results from the literature [32]). The frequency of the peak of the spectrum is expected to be inversely proportional to the characteristic length of the network at the time of decay of the network, and is thus roughly given by*

$$f_{\rm p} = \frac{2}{\alpha}\frac{a_\star}{L_\star}\,, \tag{6.42}$$

where $L_\star = \xi_\star t_\star = \xi\lambda_\star H_\star^{-1}$. Most of the GW energy density is, in general, concentrated within a narrow frequency range around the peak of the spectrum and, as we discussed above, the peak amplitude is, aside from a factor that is generally of order unity, approximately given by Eqs. (6.10, 6.11).

6.2.1 Cosmic Microwave Background Constraints

The domain wall network is expected to have been formed at a temperature $T_{\rm birth} \sim \eta$. Since the network (obviously) cannot decay before it is formed, the characteristic energy scale of a domain wall network that survives until $z_\star$ necessarily has to fulfill the condition $T_\star < T_{\rm birth}$. Using the well-known temperature-redshift relation [82], and once again accounting for the change in the number of relativistic degrees of freedom, we should then have that:

$$\eta > \left(\frac{45}{4\pi^3}\frac{H_0^2 \mathcal{G}_\star \Omega_{\rm r}}{G g_\star}\right)^{1/4}(1+z_\star)\,, \tag{6.43}$$

where $g_\star = g(z_\star)$ and

$$g(z) = \begin{cases} 3.36 & \text{for } z < z_{e^+e^-} \\ 10.75 & \text{for } z_{\rm QCD} < z < z_{e^+e^-} \\ 106.75 & \text{for } z > z_{\rm QCD} \end{cases}\,, \tag{6.44}$$

describes the effective number of degrees of freedom at a redshift z [122].

Moreover, if domain walls were to dominate the energy budget, at any point in cosmic history, the evolution of the universe would be extremely inhomogeneous and anisotropic on Hubble volume patches intersected by domain walls. The volume pressure responsible for the decay of the domain wall network would also inevitably lead to the inflation of Hubble volume patches without domain walls before the network had a chance to decay.

*Aside from $\mathcal{O}(1)$ factors associated to the changes in the number of relativistic degrees of freedom and to the uncertainties regarding the spectral index ν (cf. Eqns. (6.20, 6.25)).

Domain walls then should always provide a subdominant contribution to the cosmic energy budget. This condition can be expressed as $\rho_{\rm dw}(t) = \sigma_0/L(t) < \rho_{\rm crit}(t)$ and it results in an additional constraint on the characteristic energy scale at domain wall formation, given by:

$$\eta < \left(\frac{3H_\star\lambda_\star\xi_\star}{8\pi G}\right)^{1/3} . \tag{6.45}$$

Here, $\lambda_\star = \lambda_{\rm r}$ and $\xi_\star = \xi_{\rm r}$ (or $\lambda_\star = \lambda_{\rm m}$ and $\xi_\star = \xi_{\rm m}$) for $z_\star$ greater (or smaller) than $z_{\rm eq}$.

Finally, the power spectrum of temperature and polarization anisotropies of the CMB is extremely sensitive to the expansion rate at the time of decoupling, which, for a flat universe, is fully determined by the energy density at that time. As a result, CMB observations impose stringent constraints on the effective number of relativistic degrees of freedom at the time of decoupling, which provides a tight limit on the total energy density in gravitational waves generated before that time. One recently derived constraint that takes into account the Planck 2018 data [56] places this limit at

$$\Omega_{\rm gw}^{\rm (CMB)}h^2 < 1.7\cdot 10^{-6} \tag{6.46}$$

for frequencies $f \gtrsim 10^{-15}\,{\rm Hz}$ [227]. There are also similar constraints at the time of primordial nucleosynthesis, but these apply only at much larger redshifts ($z \gtrsim 10^9$) [228, 229] and result, therefore, in weaker constraints. Other CMB bounds on domain wall networks have been derived in the literature [230, 231], however these differ from our analysis as they rely on μ-distortions and birefringence rather than the total GW energy density.

In figure 6.5, we display the values of $\mathcal{F}^{1/3}\eta$ allowed by CMB data (shaded area) as a function of the redshift of decay of the network. This allowed region of the $(z_\star, \mathcal{F}^{1/3}\eta)$-parameter space is obtained by combining the bound obtained by requiring that $\Omega_{\rm gw}(z_{\rm dec}) \leq \Omega_{\rm gw}^{\rm (CMB)}$ (green line) — where $z_{\rm dec}$ is the redshift at the time of decoupling — and that domain walls never dominate the energy budget (red lines). Regarding the latter bound, we include the cases in which $\mathcal{F} = 1$ (dashed line) and $\mathcal{F} = 10^{-6}$ (dot-dashed line). For $\mathcal{F} = 1$, this actually corresponds to an absolute constraint and it is only slightly less stringent than the upper bound on $\mathcal{F}^{1/3}\eta$ obtained from the CMB bound on $\Omega_{\rm gw}$ for $z < z_{\rm dec}$. However, since the CMB constrains only the total energy density of GWs created until decoupling, the resulting bounds for walls that survive past decoupling are independent of $z_\star$ and weaker than those that result from imposing that domain walls are always subdominant for $\mathcal{F} = 1$. For values of $\mathcal{F} \lesssim 0.3$, Eqn. (6.45) is always more constraining than

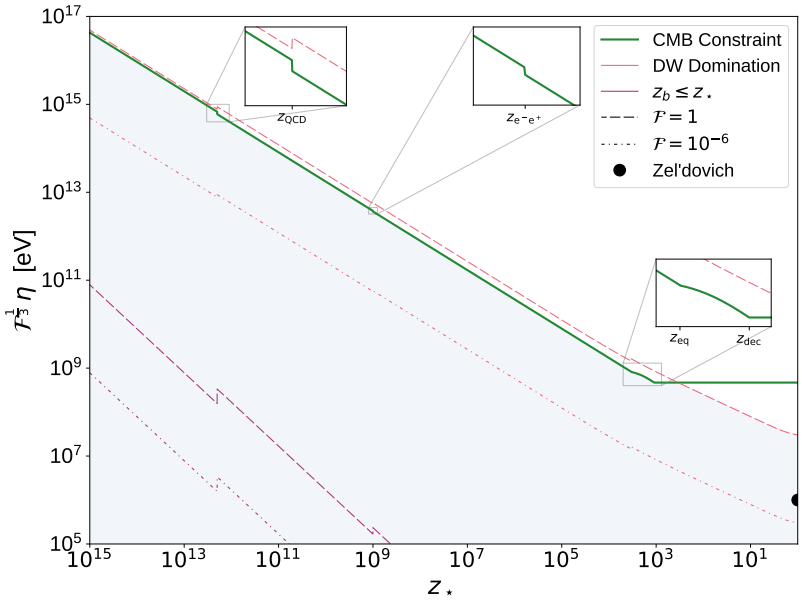

Figure 6.5: Combined constraints on $\mathcal{F}^{1/3}\eta$ as a function of the redshift $z_\star$ at the time of decay of the domain wall network. The green line represents the upper limit on $\mathcal{F}^{1/3}\eta$ resulting from the CMB bound in Eqn. (6.46). The red lines represent the limit in which domain walls dominate the universe's energy budget (area above is excluded), while the purple lines mark the boundary where the time of decay coincides with the time of formation of the domain wall network (area below is excluded). In the two latter cases, the dashed- and dashed dotted lines correspond to values of $\mathcal{F} = 1$ and $\mathcal{F} = 10^{-6}$ respectively. The Zel'dovich bound is indicated by the black marker in the plot. The shaded area represents the allowed region in parameter space if $\mathcal{F}$ is treated as a free parameter.

the CMB bound.

One may also derive lower bounds on $\mathcal{F}^{1/3}\eta$, using Eqn. (6.43), but these also depend on $\mathcal{F}$. These bounds are included in figure 6.5, as dashed and dot-dashed purple lines for $\mathcal{F} = 1$ and $\mathcal{F} = 10^{-6}$, respectively. Notice that, for a given value of $\mathcal{F}$, the allowed region of parameter space is also bounded from below by this constraint and then is given by a narrow band.

6.2.2 Domain Wall Interpretation of PTA Data

Recently, different Pulsar Timing Arrays — including NANOGrav [34], PPTA [36], EPTA [35] and CPTA [37] — have produced the first convincing evidence for a SGWB in the nanohertz frequency band. These results all indicate the existence of an excess signal with a characteristic strain amplitude of the order $\mathcal{O}(10^{-15})$ at a reference frequency of $1\,\mathrm{yr}^{-1} \simeq 31.7\,\mathrm{nHz}$. Assuming that the spectral index of the spectrum d — defined such that $\Omega_{\rm gw} \propto f^d$ locally — is free, this data may be translated into the following value for the spectral density of gravitational waves:

$$\Omega_{\rm gw}(f)h^2 \simeq 6.3 \times 10^{-10} A^2 \left(\frac{f}{\mathrm{yr}^{-1}}\right)^d , \tag{6.47}$$

with a range of allowed parameters of $A = 6.4^{+4.2}_{-2.7}$ and $d = 1.8 \pm 0.6$ for NANOGrav [34], $A = 2.9^{+2.6}_{-1.8}$ and $d = 0.81^{+0.63}_{-0.73}$ for EPTA [35] and $A = 3.1^{+1.3}_{-0.9}$ and $d = 1.1 \pm 0.4$ for PPTA [36]. This spectral shape is valid within a frequency range of roughly $[f_{\rm min}, f_{\rm max}]$, with $f_{\rm min} = 3.2 \cdot 10^{-8}\,\mathrm{Hz}$ and $f_{\rm max} = 10^{-7}\,\mathrm{Hz}$. Here, we will investigate whether such a signature could be produced by a biased domain wall network as was proposed in the literature [136, 232–235].

Given the uncertainty associated with the shape of the SGWB power spectrum, here we will again focus on the total gravitational wave energy density instead. A conservative lower bound on the fractional contribution of the SGWB to the cosmic energy budget in the PTA frequency range may be obtained by calculating

$$\Omega_{\rm gw}^{\rm (PTA)} = \int_{f_{\rm min}}^{f_{\rm max}} \Omega_{\rm gw}(f) \frac{df}{f} , \tag{6.48}$$

while considering the lower bounds on the parameters A and d. This gives us the minimum GW energy density one would need to have in this range to generate the observed signal in each PTA experiment:

$$\left(\Omega_{\rm gw}^{\rm (NANO)}, \Omega_{\rm gw}^{\rm (EPTA)}, \Omega_{\rm gw}^{\rm (PPTA)}\right) = \left(4.643 \cdot 10^{-8}, 1.995 \cdot 10^{-9}, 1.170 \cdot 10^{-8}\right) .$$

The observed PTA spectrum, fitted by the function given in Eqn. (6.47), appears to be an increasing function of frequency, as all experiments predict that $d > 0$. Hence, if the main contribution to this spectrum was to be provided by the gravitational radiation produced by biased domain walls, it should mostly correspond to the part of the spectrum that lies to the left of the peak (on the lower frequency side). Moreover, since for $f \ll f_{\rm p}$, one should have $\Omega_{\rm gw}(f) \propto f^3$ due to causality constraints [223], the peak of the spectrum cannot be located at a frequency that is much larger than $f_{\rm max}$. On one hand, PTA data seems to be consistent with smaller values of d — which would indicate that, if domain walls are to be the main source, the detected signal should correspond to the transitional region between the peak and the regime characterized by $d = 3$. On the other hand, if $f_{\rm p} \gg f_{\rm max}$, the amplitude of the peak would have to be very large in order to explain the signal within the PTA window and $\Omega_{\rm gw}$ would then exceed the stringent bounds discussed in the previous section. In fact, if the spectrum between $f_{\rm max}$ and $f_{\rm p}$ has a spectral index of $d = 3$, the total energy contained in the frequency interval $[f_{\rm max}, f_{\rm p}]$ would exceed the total energy limits dictated by the CMB bound for $f_{\rm p} \gtrsim 5 \cdot 10^{-7}\,{\rm Hz} = 5 \cdot {\rm f}_{\rm max}$. The upper limit we compute for the redshift $z_\star$ at the time of decay of the network, under the assumption that $f_{\rm p}$ is contained in $[f_{\rm min}, f_{\rm max}]$, may then increase at most by this factor of 5. We will then assume that the peak of the spectrum lies within the frequency interval $[f_{\rm min}, f_{\rm max}]$.

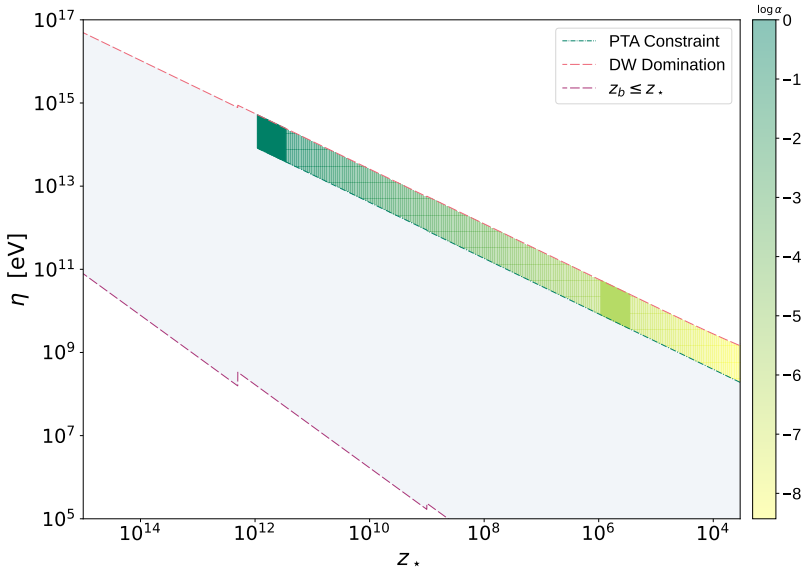

Figure 6.6: Allowed values for the characteristic energy scale η of domain walls as a function of the redshift of decay $z_\star$. The red and purple lines represent the constraints resulting from imposing that walls cannot dominate the energy budget of the universe and that their time of decay cannot be before the time of their formation. The area shaded in blue represents the region of parameter space compatible with these constraints. The color shaded band represents the region of parameter space compatible with the NANOGrav data, assuming domain wall networks constitute the main contribution to this signal. The dark- and light green rectangles represent the allowed regions assuming a fixed value of $\alpha = 1$ and $\alpha = 10^{-6}$ respectively. More details in the text.

If $f_{\rm p} \gtrsim f_{\rm min}$ and assuming that $\alpha \gtrsim 10^{-8}$, then the domain wall network must have decayed during the radiation dominated era. Eqn. (6.42) then implies

$$f_{\rm p} = \frac{8 H_0 \Omega_r^{\frac{1}{2}}}{\alpha \tilde{\zeta}_r} (1 + z_\star) \,. \tag{6.49}$$

The redshift of decay of the network may then be inferred from the location of the peak for each value of α. Then, using Eqn. (6.10) and the lower bounds we have derived for the value of $\Omega_{\rm gw}$ in different PTA experiments, we may derive constraints on $\mathcal{F}^{1/3}\eta$. Note that, in deriving these constraints, we will neglect the contribution to $\Omega_{\rm gw}$ outside of the $[f_{\rm min}, f_{\rm max}]$ range and therefore the bounds derived here should be conservative. Moreover, since the domain wall SGWB should be simultaneously consistent with the data of all PTA experiments, we consider $\Omega_{\rm gw}^{(\rm NANO)} = 4.64 \cdot 10^{-8}$, which corresponds to the strongest signal detected across the various PTA experiments.

In figure 6.6, we plot the allowed region of the $(z_\star, \eta)$-parameter space (shaded blue area) for domain wall networks. This figure includes the constraints in Eqs. (6.43) and (6.45) — again plotted as red and purple lines respectively — but here they become fixed boundaries of the allowed parameter space, since we display this only in terms of the energy scale η (i.e., independently of $\mathcal{F}$). Additionally, the green dashed line marks the minimal characteristic energy scale η required for domain wall networks to generate the PTA signals for $\mathcal{F} = 1$. Since a larger contribution of the fractional energy density in gravitational waves as well as a smaller value of $\mathcal{F}$ would both imply a stronger bound on η, only the region above this line is compatible with the observed PTA signal. There is then only a tight range of about one order of magnitude in η that is compatible with PTA experiments and avoids domain wall domination. Notice that, if one considers networks with $\mathcal{F} < 1$ — as one would realistically expect, since domain walls may also emit scalar radiation in their decay — this allowed range of η becomes even narrower. This means, in particular, that values of $\mathcal{F} \lesssim 0.004$ can be ruled out if domain walls are to be the main contributors to the PTA signal.

Additionally, under the assumption that the peak of the domain wall gravitational wave spectrum lies within the frequency interval [$f_{\rm min}$, $f_{\rm max}$], one may see that the allowed range of $z_\star$ is also very narrow for each value of α. figure 6.6 shows the region of the ($z_\star$, η) parameter space compatible with PTA data for $\alpha = 1$ and $\alpha = 10^{-6}$ (as the opaque dark and light green areas respectively). For an α of order unity, this would imply a decay time of the domain wall network shortly after the QCD phase transitions, while the redshift

of decay (roughly) linearly shifts with smaller α to later times as indicated by the color bar on the right side of the plot. Considering the constraints on the time of decay and on the energy scale η at domain wall formation, for a given value of α, the region of parameter space consistent with the signal detected by PTAs becomes extremely narrow, requiring a substantial fine tuning of the properties of the domain wall networks in order to explain the SGWB detected by the PTAs.

7. Summary and Outlook

In this thesis, we have presented a comprehensive study of domain walls in cosmology. We have employed numerical and (semi-) analytical techniques to cover many aspects related to domain wall physics, both on cosmological scales (by studying the macroscopic evolution of domain wall networks), as well as on smaller scales (for instance, by investigating the local interactions of domain walls with matter overdensities). We have also studied gravitational wave emission by domain wall networks and confronted our findings with current observational constraints. Here, we summarize our main results and outline directions for future research.

Chapters 1 and 2 of this thesis were dedicated to reviewing the foundations of modern cosmology as well as the state-of-the-art understanding of domain wall physics. We summarized ΛCDM — the cosmological standard model — and cosmic inflation and highlighted the importance of scalar fields in cosmology. This led us to classify topological defects and discuss their formation. We then focused on a more detailed study of domain walls, analyzing some properties of the Goldstone model, reviewing the VOS model and the PFM to study network evolution, and discussed biased walls.

In chapter 3, we described field theory simulations of cosmic domain walls using the PRS algorithm, which modifies the equation of motion to preserve a constant thickness of walls on a comoving lattice. We described how to implement this algorithm in *Python* with the focus on maximizing performance on systems comparable to personal computers. Although the simulations we performed during my PhD cannot compete with state-of-the-art simulations performed on supercomputers in terms of lattice size [159, 166], we managed to optimize the code sufficiently to not be restricted by computation time but only by the availability of RAM and VRAM, while still easily guaranteeing sufficient resolution to study many important aspects of domain wall dynamics.

We then explored the working principles of different methods commonly used in the literature to measure the characteristic length from simulations. This analysis was motivated by our efforts to better understand the differences between the predictions of the PFM and simulations in the relativistic regime. We first studied how the spatial discretization of the simulation grid can lead to discrepancies between the results extracted locally from a

simulation box with respect to what would be expected in the continuum limit. Further analysis showed, however, that these discretization errors essentially cancel in full network simulations and thus do not need to be considered as a significant source of error. We compared the different methods of extracting the domain wall length-scale and analyzed the impact of root mean squared velocity of walls on them. We showed that there exists a deviation of the quantitative results extracted with each of these methods, which can be attributed to the Lorentz contraction of walls in the relativistic regime, and which therefore grows as one considers smaller expansion rates of the cosmological background. We quantified this dependency on the Lorentz factor, which ultimately led us to introduce a novel method to extract the RMS velocity from simulations of domain wall networks that does not require knowledge of time derivatives of the field. We showed that there is a very good agreement between the measurements with this new method and the standard method to extract the RMS velocity of walls. This new method can easily be employed in large network simulations in a computationally cheap way. In the regime of low expansion rates, however, minor deviations between the methods become apparent, which are very likely attributed to the presence of large amounts of scalar radiation in this regime. It may be an interesting topic of future research to study the exact sources of those deviations in more detail and therefore explain the differences in a more quantitative manner.

In chapter 4 we then explored different aspects of the parameter-free model. We started by deriving analytical expressions for the evolution of the radius and the velocity of collapsing spherical- and cylindrical domains. One of these sets of equations is exact in the case of a Minkowski background, while another represents an excellent approximation in the regime of fast expansion rates. These expressions then allowed us to obtain two independent approximations for both the characteristic length and the RMS velocity, using the formalism of the PFM. The first approximation, A1, is useful due to its simplicity and analytical nature, which allows for an easy integration in analytical models. The second approximation, A2, on the other hand, is obtained numerically, but is closer to the predictions of the PFM; opposed to A1, it distinguishes between spherical and cylindrical domains. We then provided a simple analytical fitting function, which allows reproducing the values for the characteristic length and the RMS velocity predicted by the PFM, with an error below 1 % over the whole range of decelerated power-law expansion rates.

To gain a better understanding of the discrepancies of the PFM and simulations in the regime of low expansion rates, we then performed numerical tests of collapsing spherical and cylindrical domains. The goal here was to establish a bridge between these

field theory simulations and the PFM by simulating the collapse of single domains (whose evolution forms the basis of the predictions of the parameter-free model) using the same techniques typically used to measure the characteristic length and RMS velocities directly from large-scale network simulations. This should allow us to detect any systematic effects attributed to the extraction of parameters from simulations. We started by comparing the evolution of those simulated domains to the respective predictions obtained by solving the Nambo-Goto EOMs. This showed that there generally is a very good correspondence between both, and only in the last stages of collapse, when domains reach ultra-relativistic velocities, discrepancies begin to develop. Further investigation showed that the crucial parameter determining exactly when simulations begin to break down is the initial wall thickness.

We then used the evolution we measured from simulations to compute the characteristic length and the RMS velocity and compared those values to the predictions of the PFM. The relatively good correspondence of both suggests that systematic effects associated with the way quantities are extracted from field theory simulations cannot solely explain the discrepancy between the PFM and those simulations in the relativistic regime. We already discussed some possible other sources for this deviation at the end of section 4.3. There we mentioned the more complex geometry of realistic domains as opposed to the idealized domains considered here. Note that in the case of cylindrical and spherical domains, the radius has a very pictorial meaning. However, its extraction from simulations using the energy method is independent of the shape of domains. Consequently, the method can be applied to define an effective radius for domains with arbitrary complex geometries. Such a definition enables the reanalysis of the studies presented in this section for more realistic domains, such as those isolated from field theory network simulations. We then would be able to cross-check the evolution with predictions from our analytical approximation, in which we also derived predictions for the rate of change in area/volume of 2D/3D domains of arbitrary shapes. This would allow us to further test the influence of geometry on the prediction of the PFM and we have already performed some preliminary work in this direction.

In chapter 5 we studied two independent non-standard domain wall models. We began by analyzing the interaction of domain walls with compact objects using a toy model Lagrangian. We studied this interaction two-fold, by performing simulations and developing an analytical model to predict whether a wall would have sufficient energy to pass an object or not. In the case where the wall is much thinner than the radius of the object, this

model was able to predict the critical object density, above which a wall would get reflected with high accuracy. We were also able to get an estimate of the energy loss in such a collision, which increased around 2 % per unit increase of the Lorentz factor corresponding to the initial wall velocity. We also introduced an empirical model to describe the collisions of thick walls with objects and initial tests seem to indicate that this model performs well. This, however, has yet to be tested with a larger number of simulations over a wide range of parameters and initial conditions. It may also be interesting to perform more numerical tests in 2D or 3D lattices, which would allow us to further investigate the influence of the object and wall geometry on these results. Once the interactions with single objects are well understood, one may also want to study a distribution of objects underlying a domain wall network simulation, in order to determine possible effects on large scales due to this interaction. Another step in making these simulations more realistic would be to allow for a momentum transfer to the object, which in that case would have to be free to move within the simulation grid.

The study of wall-object interaction then led us to analyze small-scale structure developing on the wall as a consequence of collisions. We were primarily interested in the dominant frequency of the perturbations on the wall. We found that this frequency can well be described by the inverse of an effective wall thickness we defined. Moreover, we observed a beat in the oscillation which indicates the presence of a secondary relevant scale. These results show some similarity to the excitations described in [204] and a closer comparison could provide an interesting basis for future studies.

We also investigated a non-standard model based on a biased ϕ^6 potential. In this case, we observed using simulations that a collapsing domain wall between the false vacuum states can induce a cosmological phase transition into the true vacuum state. We constructed an analytical model to predict the minimal radius of the initial domain (and therefore the minimal energy) necessary to induce such a transition and made some preliminary predictions. These can be tested with further simulations. The model, which is currently restricted to cylindrical domains in the case of a Minkowski background, can then be extended to more realistic scenarios.

In chapter 6, we investigated the power spectrum of the SGWB produced by domain wall networks and compared it to current observational constraints. We started by introducing a novel analytical framework, which assumes that the main source of energy loss by the network is associated with the collapse, on a timescale of roughly one Hubble time,

of domain walls that detach from the Hubble flow and that these walls disappear quickly after, leaving behind a contribution to the gravitational wave and scalar radiation backgrounds. These basic assumptions were shown to be sufficient to estimate the energy density associated with the SGWB generated by domain walls, as a function of two crucial parameters of our model: the constant fraction of the energy lost by the network that goes into gravitational waves and the domain wall tension. We modeled the scale dependence of the average distribution in frequency of the GWs emitted by domain walls in the final collapse stages using a simple probability density function characterized by two further parameters: a minimum frequency inversely proportional to the characteristic length of the network at the time of collapse and a constant power spectrum slope. We also investigated the limiting case where all the emission happens at the minimum frequency. For all these cases, we were able to compute the power spectrum of the SGWB generated by domain walls as observed at the present time. Furthermore, we developed an analytical approximation assuming perfect linear scaling in both radiation and matter eras. We have shown that the power spectrum of the SGWB background generated by domain walls is a monotonically decreasing function of the frequency whose peak and slope depend mildly on the two parameters characterizing the average frequency distribution of the GWs generated by domain walls at the time of emission. We have additionally investigated the case of biased domain walls, considering both the contribution to the SGWB generated while the network is stable and the contribution associated with the sudden decay of the domain walls. As we discussed, there exist some discrepancies between the predictions made by our framework and results obtained in the literature, the latter being mainly based on numerical simulations. These should constitute a strong motivation for an in-depth characterization of the GWs generated by collapsing domain walls. Probing the dynamics of domain walls in the ultra-relativistic regime — during which their main contribution to the SGWB is expected to be generated — will probably require a new generation of field theory simulations, capable of dealing with the major challenge posed by the Lorentz contraction of the width of ultra-relativistic domain walls. Our results also seem to indicate that gravitational backreaction may play a more significant role in the evolution of domain wall networks than originally anticipated, and investigating this may also help clarify the discrepancies between the two approaches.

Using our analytical framework, we furthermore investigated the allowed domain wall scenarios in light of current CMB and PTA data. Our results show that indirect CMB bounds on the fractional density in gravitational waves at the time of decoupling have a limited

constraining power on domain wall scenarios and generally provide constraints that are less stringent than those that result from imposing that domain walls provide only a subdominant contribution to the cosmic energy budget. Only if the emission of gravitational radiation, and not scalar radiation, is the dominant decay mechanism of collapsing domain walls does this CMB bound lead to a decrease of the allowed region of the $(z_\star, \eta)$ parameter space. Notice, however, that the CMB constraints derived here are conservative because the computation of $\Omega_{\rm gw}$ only includes the GWs emitted before the whole domain wall network decays at $z_\star$. There may also be a significant emission of GWs during the final collapse of the network, which, as we have shown, should enhance $\Omega_{\rm gw}$ by up to one order of magnitude.

Despite this, we found that even without considering CMB bounds, the range of allowed energy scales for the domain-wall forming phase transition is already quite limited, especially for networks that decay early in cosmic history. For instance, for walls decaying at $z_\star \sim 10^{18}$ (at a temperature of roughly $T_\star \sim 100\,\mathrm{TeV}$), we should have that $10^2 \lesssim \eta \lesssim 10^6\,\mathrm{TeV}$ (roughly 4 orders of magnitude in range), while for $z_\star \sim 10^8$ ($T_\star \sim 10^{-1}\,\mathrm{MeV}$), the allowed parameter range is much wider: $10^{-1} \lesssim \eta \lesssim 10^6\,\mathrm{MeV}$.

We have also found that, if domain walls are to provide an explanation to the observed PTA signal, this would require a significant fine-tuning of the parameters of the model. Domain walls would not only need to have a significant GW emission efficiency — we found that $\mathcal{F} \gtrsim 10^{-3}$, however, as previously explained, we were quite conservative in deriving this constraint — but their energy density would have to be very close to dominating the energy density of the universe. As a matter of fact, the allowed range of parameters is very narrow: one should have, roughly, that $\eta \sim \mathcal{O}(10^2)\,\mathrm{TeV}$ and, for $\alpha = 1$, $T_\star \sim \mathcal{O}(10^2)\,\mathrm{MeV}$ ($T_\star$ would roughly decrease proportionally to α). Like in the previous case, this result was derived based on the contribution to the SGWB before the actual decay of the network. Here, in fact, taking an enhancement of the SGWB due to the network's decay into account could potentially increase the range of allowed parameter space by lowering the minimal domain wall tension required to reproduce the signal. As discussed before, this would be model dependent and at most lower the minimal σ by one order of magnitude, which would translate into less than a factor of one half in the characteristic energy scale. These results are in very good agreement with those presented in the literature [136, 232–235], but unlike those, ours are based on minimal assumptions and as model-independent as possible.

With the Square Kilometre Array (SKA), which is anticipated to be able to detect a much higher number of pulsars than current state-of-the-art experiments, likely going online within the next years, we expect the nano-hertz SGWB signal to be characterized with a significantly higher sensitivity, and possibly within a slightly extended frequency range [236, 237], which could in consequence allow for an improvement of our constraints. A true "game changer", however, may be the next generation of ground- and space-based gravitational wave observatories [38, 39, 208, 238, 239], which, if they were to detect a SGWB signal, could help to distinguish signals from different cosmological sources, due to the distinct power-law scaling of their spectra.

This summary concludes the results obtained during my PhD and points towards some interesting prospects on how this work may be followed up. Since a large portion of the work described here has not yet been published, an immediate goal for me will hence be the refinement of some of the results obtained here, with the goal of producing one or more additional research articles. Beyond that, cosmic defects, and domain walls in particular, will likely remain a hot topic in cosmology. With the aforementioned next generation of gravitational wave detectors, a potential detection of defects might eventually be in reach. Their close ties to particle physics mean that any discovery could shed valuable light on the conditions of the early universe and contribute to a better understanding of some of the most fundamental questions in physics.

References

[1] *Paul Tol's Colour Schemes and Templates*. url: https://personal.sron.nl/~pault/.

[2] Pedro Avelino, David Grüber, and Lara Sousa. "Analytical Scaling Solutions for the Evolution of Cosmic Domain Walls in a Parameter-Free Velocity-Dependent One-Scale Model". In: *Symmetry* 14.9 (9 Sept. 2022). doi: 10.3390/sym14091799. url: https://www.mdpi.com/2073-8994/14/9/1799.

[3] D. Grüber, P. P. Avelino, and L. Sousa. *Domain Walls in Light of Cosmic Microwave Background and Pulsar Timing Array Data*. June 4, 2024. doi: 10.48550/arXiv.2406.02288. arXiv: 2406.02288. url: http://arxiv.org/abs/2406.02288. Pre-published.

[4] D. Grüber, L. Sousa, and P. P. Avelino. "Stochastic Gravitational Wave Background Generated by Domain Wall Networks". In: *Phys. Rev. D* 110.2 (2024). doi: 10.1103/PhysRevD.110.023505.

[5] L. Verde, T. Treu, and A. G. Riess. "Tensions between the Early and the Late Universe". In: *Nature Astron.* 3 (2019). doi: 10.1038/s41550-019-0902-0.

[6] Wendy L. Freedman et al. "Status Report on the Chicago-Carnegie Hubble Program (CCHP): Three Independent Astrophysical Determinations of the Hubble Constant Using the James Webb Space Telescope". In: (Aug. 2024).

[7] Tanvi Karwal and Marc Kamionkowski. "Dark Energy at Early Times, the Hubble Parameter, and the String Axiverse". In: *Physical Review D* 94.10 (Nov. 28, 2016). doi: 10.1103/PhysRevD.94.103523. url: https://link.aps.org/doi/10.1103/PhysRevD.94.103523.

[8] Vivian Poulin et al. "Early Dark Energy Can Resolve The Hubble Tension". In: *Phys. Rev. Lett.* 122.22 (2019). doi: 10.1103/PhysRevLett.122.221301.

[9] Amir Aghamousa et al. "The DESI Experiment Part I: Science,Targeting, and Survey Design". In: (Oct. 2016).

[10] Luca Amendola et al. "Cosmology and Fundamental Physics with the Euclid Satellite". In: *Living Rev. Rel.* 21.1 (2018). doi: 10.1007/s41114-017-0010-3.

[11] C. Armendariz-Picon, Viatcheslav F. Mukhanov, and Paul J. Steinhardt. “A Dynamical Solution to the Problem of a Small Cosmological Constant and Late Time Cosmic Acceleration”. In: *Phys. Rev. Lett.* 85 (2000). doi: 10.1103/PhysRevLett.85.4438.

[12] R. R. Caldwell, Rahul Dave, and Paul J. Steinhardt. “Cosmological Imprint of an Energy Component with General Equation of State”. In: *Physical Review Letters* 80.8 (Feb. 23, 1998). doi: 10.1103/PhysRevLett.80.1582. url: https://link.aps.org/doi/10.1103/PhysRevLett.80.1582.

[13] Paulo M. Sá. “Triple Unification of Inflation, Dark Energy, and Dark Matter in Two-Scalar-Field Cosmology”. In: *Physical Review D* 102.10 (Nov. 13, 2020). doi: 10.1103/PhysRevD.102.103519. arXiv: 2007.07109. url: http://arxiv.org/abs/2007.07109.

[14] John Preskill, Mark B. Wise, and Frank Wilczek. “Cosmology of the Invisible Axion”. In: *Phys. Lett. B* 120 (1983). Ed. by M. A. Srednicki. doi: 10.1016/0370-2693(83)90637-8.

[15] Michael S. Turner. “Coherent Scalar-Field Oscillations in an Expanding Universe”. In: *Physical Review D* 28.6 (Sept. 15, 1983). doi: 10.1103/PhysRevD.28.1243. url: https://link.aps.org/doi/10.1103/PhysRevD.28.1243.

[16] P. P. Avelino and L. Sousa. “Observational Constraints on Varying-alpha Domain Walls”. In: *Universe* 1.1 (Feb. 5, 2015). doi: 10.3390/universe1010006. arXiv: 1404.3419. url: http://arxiv.org/abs/1404.3419.

[17] Vitor da Fonseca et al. “Fundamental Physics with ESPRESSO: Constraining a Simple Parametrisation for Varying α”. In: *Astron. Astrophys.* 666 (2022). doi: 10.1051/0004-6361/202243795.

[18] C. M. J. Marques, C. J. A. P. Martins, and C. S. Alves. “Fundamental Cosmology from ANDES Precision Spectroscopy”. In: *Mon. Not. Roy. Astron. Soc.* 522.4 (2023). doi: 10.1093/mnras/stad1359.

[19] Andrew Liddle. *An Introduction to Modern Cosmology*. John Wiley & Sons, Apr. 27, 2015. 200 pp. Google Books: 6n64CAAAQBAJ.

[20] Georges Aad et al. “Observation of a New Particle in the Search for the Standard Model Higgs Boson with the ATLAS Detector at the LHC”. In: *Phys. Lett. B* 716 (2012). doi: 10.1016/j.physletb.2012.08.020.

[21] Serguei Chatrchyan et al. “Observation of a New Boson at a Mass of 125 GeV with the CMS Experiment at the LHC”. In: *Physics Letters B* 716.CMS-HIG-12-028, CERN-PH-EP-2012-220 (2012). doi: 10.1016/j.physletb.2012.08.021. arXiv: 1207.7235.

[22] T W B Kibble. “Topology of Cosmic Domains and Strings”. In: *Journal of Physics A: Mathematical and General* 9.8 (Aug. 1976). doi: 10.1088/0305-4470/9/8/029. url: https://doi.org/10.1088/0305-4470/9/8/029.

[23] John Preskill. “MAGNETIC MONOPOLES”. In: *Ann. Rev. Nucl. Part. Sci.* 34 (1984). doi: 10.1146/annurev.ns.34.120184.002333.

[24] Andrei Lazanu, E. P. S. Shellard, and Martin Landriau. “CMB Power Spectrum of Nambu-Goto Cosmic Strings”. In: *Phys. Rev. D* 91.8 (2015). doi: 10.1103/PhysRevD.91.083519.

[25] Andrei Lazanu and Paul Shellard. “Constraints on the Nambu-Goto Cosmic String Contribution to the CMB Power Spectrum in Light of New Temperature and Polarisation Data”. In: *JCAP* 02 (2015). doi: 10.1088/1475-7516/2015/02/024.

[26] Joanes Lizarraga et al. “New CMB Constraints for Abelian Higgs Cosmic Strings”. In: *JCAP* 10 (2016). doi: 10.1088/1475-7516/2016/10/042.

[27] I. Yu. Rybak and L. Sousa. “CMB Anisotropies Generated by Cosmic String Loops”. In: *Phys. Rev. D* 104.2 (2021). doi: 10.1103/PhysRevD.104.023507.

[28] Benjamin Shlaer, Alexander Vilenkin, and Abraham Loeb. “Early Structure Formation from Cosmic String Loops”. In: *JCAP* 05 (2012). doi: 10.1088/1475-7516/2012/05/026.

[29] Benjamin M. Roberts et al. “Search for Domain Wall Dark Matter with Atomic Clocks on Board Global Positioning System Satellites”. In: *Nature Communications* 8.1 (Dec. 2017). doi: 10.1038/s41467-017-01440-4. arXiv: 1704.06844. url: http://arxiv.org/abs/1704.06844.

[30] Aneesh P. Naik and Clare Burrage. *Dark Sector Domain Walls Could Explain the Observed Planes of Satellites*. May 2, 2022. arXiv: 2205.00712. url: http://arxiv.org/abs/2205.00712. Pre-published.

[31] P. P. Avelino et al. “Frustrated Expectations: Defect Networks and Dark Energy”. In: *Physical Review D* 73.12 (June 15, 2006). doi: 10.1103/PhysRevD.73.123519. arXiv: astro-ph/0602540. url: http://arxiv.org/abs/astro-ph/0602540.

[32] Takashi Hiramatsu, Masahiro Kawasaki, and Ken'ichi Saikawa. "On the Estimation of Gravitational Wave Spectrum from Cosmic Domain Walls". In: *Journal of Cosmology and Astroparticle Physics* 2014.02 (Feb. 19, 2014). doi: 10.1088/1475-7516/2014/02/031. arXiv: 1309.5001. url: http://arxiv.org/abs/1309.5001.

[33] Takashi Hiramatsu, Masahiro Kawasaki, and Ken'ichi Saikawa. "Gravitational Waves from Collapsing Domain Walls". In: *Journal of Cosmology and Astroparticle Physics* 2010.05 (May 24, 2010). doi: 10.1088/1475-7516/2010/05/032. arXiv: 1002.1555. url: http://arxiv.org/abs/1002.1555.

[34] Gabriella Agazie et al. "The Nanograv 15 Yr Data Set: Evidence for a Gravitational-Wave Background". In: *Astrophysical Journal, Letters to the Editor* 951.1 (2023). doi: 10.3847/2041-8213/acdac6. arXiv: 2306.16213.

[35] J. Antoniadis et al. "The Second Data Release from the European Pulsar Timing Array - III. Search for Gravitational Wave Signals". In: *Astron. Astrophys.* 678 (2023). doi: 10.1051/0004-6361/202346844.

[36] Daniel J. Reardon et al. "Search for an Isotropic Gravitational-wave Background with the Parkes Pulsar Timing Array". In: *Astrophys. J. Lett.* 951.1 (2023). doi: 10.3847/2041-8213/acdd02.

[37] Heng Xu et al. "Searching for the Nano-Hertz Stochastic Gravitational Wave Background with the Chinese Pulsar Timing Array Data Release I". In: *Res. Astron. Astrophys.* 23.7 (2023). doi: 10.1088/1674-4527/acdfa5.

[38] Pau Amaro-Seoane et al. *Laser Interferometer Space Antenna*. Feb. 23, 2017. doi: 10.48550/arXiv.1702.00786. arXiv: 1702.00786. url: http://arxiv.org/abs/1702.00786. Pre-published.

[39] Pierre Auclair et al. "Probing the Gravitational Wave Background from Cosmic Strings with LISA". In: *Journal of Cosmology and Astroparticle Physics* 2020.04 (Apr. 22, 2020). doi: 10.1088/1475-7516/2020/04/034. arXiv: 1909.00819. url: http://arxiv.org/abs/1909.00819.

[40] Donald G. York et al. "The Sloan Digital Sky Survey: Technical Summary". In: *The Astronomical Journal* 120.3 (Sept. 1, 2000). doi: 10.1086/301513. url: https://iopscience.iop.org/article/10.1086/301513/meta.

[41] Jean-Philippe Uzan. "Varying Constants, Gravitation and Cosmology". In: *Living Reviews in Relativity* 14.1 (Dec. 2011). doi: 10.12942/lrr-2011-2. arXiv: 1009.5514. url: http://arxiv.org/abs/1009.5514.

[42] Julian A. King et al. “Spatial Variation in the Fine-Structure Constant – New Results from VLT/UVES”. In: *Monthly Notices of the Royal Astronomical Society* 422.4 (June 1, 2012). doi: 10.1111/j.1365-2966.2012.20852.x. arXiv: 1202.4758. url: http://arxiv.org/abs/1202.4758.

[43] Malcolm Longair. *Galaxy Formation*. 2nd ed. Astronomy and Astrophysics Library. Berlin Heidelberg: Springer-Verlag, 2008. doi: 10.1007/978-3-540-73478-9. url: https://www.springer.com/gp/book/9783540734772.

[44] Steven Weinberg. *Gravitation and Cosmology: Principles and Applications of the General Theory of Relativity*. New York: John Wiley and Sons, 1972.

[45] Albert Einstein. “Die Feldgleichungen Der Gravitation”. In: *Sitzungsberichte der Königlich Preussischen Akademie der Wissenschaften* (Jan. 1, 1915). url: https://ui.adsabs.harvard.edu/abs/1915SPAW.....844E.

[46] Albert Einstein. “Kosmologische Betrachtungen Zur Allgemeinen Relativitätstheorie”. In: *Sitzungsberichte der Königlich Preussischen Akademie der Wissenschaften* (Jan. 1, 1917). url: https://ui.adsabs.harvard.edu/abs/1917SPAW.....142E.

[47] Edwin Hubble. “A Relation between Distance and Radial Velocity among Extra-Galactic Nebulae”. In: *Proceedings of the National Academy of Science* 15 (Mar. 1, 1929). doi: 10.1073/pnas.15.3.168. url: https://ui.adsabs.harvard.edu/abs/1929PNAS...15..168H.

[48] S. Perlmutter et al. “Measurements of Ω and Λ from 42 High-Redshift Supernovae”. In: *The Astrophysical Journal* 517 (June 1, 1999). doi: 10.1086/307221. url: https://ui.adsabs.harvard.edu/abs/1999ApJ...517..565P.

[49] Adam G. Riess et al. “Type Ia Supernova Discoveries at z $>$ 1 from the Hubble Space Telescope: Evidence for Past Deceleration and Constraints on Dark Energy Evolution”. In: *The Astrophysical Journal* 607 (June 1, 2004). doi: 10.1086/383612. url: https://ui.adsabs.harvard.edu/abs/2004ApJ...607..665R.

[50] A. Rest et al. “Cosmological Constraints from Measurements of Type Ia Supernovae Discovered during the First 1.5 Years of the Pan-STARRS1 Survey”. In: *The Astrophysical Journal* 795.1 (Oct. 13, 2014). doi: 10.1088/0004-637X/795/1/44. arXiv: 1310.3828. url: http://arxiv.org/abs/1310.3828.

[51] Adam G. Riess et al. “A 3% Solution: Determination of the Hubble Constant with the Hubble Space Telescope and Wide Field Camera 3”. In: *The Astrophysical Journal* 730.2 (Apr. 1, 2011). doi: 10.1088/0004-637X/730/2/119. arXiv: 1103.2976. url: http://arxiv.org/abs/1103.2976.

[52] Karl Schwarzschild. “On the Gravitational Field of a Mass Point According to Einstein’s Theory”. In: *Sitzungsber. Preuss. Akad. Wiss. Berlin (Math. Phys.)* 1916 (1916).

[53] Roy P. Kerr. “Gravitational Field of a Spinning Mass as an Example of Algebraically Special Metrics”. In: *Phys. Rev. Lett.* 11 (1963). doi: 10.1103/PhysRevLett.11.237.

[54] E T. Newman et al. “Metric of a Rotating, Charged Mass”. In: *J. Math. Phys.* 6 (1965). doi: 10.1063/1.1704351.

[55] Steven Weinberg. “The Cosmological Constant Problem”. In: *Rev. Mod. Phys.* 61 (1989). Ed. by Jong-Ping Hsu and D. Fine. doi: 10.1103/RevModPhys.61.1.

[56] Planck Collaboration et al. “Planck 2018 Results. VI. Cosmological Parameters”. In: *Astronomy & Astrophysics* 641 (Sept. 2020). doi: 10.1051/0004-6361/201833910. arXiv: 1807.06209. url: http://arxiv.org/abs/1807.06209.

[57] Eleonora Di Valentino et al. “In the Realm of the Hubble Tension—a Review of Solutions”. In: *Class. Quant. Grav.* 38.15 (2021). doi: 10.1088/1361-6382/ac086d.

[58] Ali Rida Khalife et al. “Review of Hubble Tension Solutions with New SH0ES and SPT-3G Data”. In: *JCAP* 04 (2024). doi: 10.1088/1475-7516/2024/04/059.

[59] Nandita Khetan et al. “A New Measurement of the Hubble Constant Using Type Ia Supernovae Calibrated with Surface Brightness Fluctuations”. In: *Astron. Astrophys.* 647 (2021). doi: 10.1051/0004-6361/202039196.

[60] Yukei S. Murakami et al. “Leveraging SN Ia Spectroscopic Similarity to Improve the Measurement of H_0”. In: *JCAP* 11 (2023). doi: 10.1088/1475-7516/2023/11/046.

[61] Jian-Ping Hu and Fa-Yin Wang. “Hubble Tension: The Evidence of New Physics”. In: *Universe* 9.2 (2023). doi: 10.3390/universe9020094.

[62] Gordon Kane, Kuver Sinha, and Scott Watson. “Cosmological Moduli and the Post-Inflationary Universe: A Critical Review”. In: *Int. J. Mod. Phys. D* 24.08 (2015). doi: 10.1142/S0218271815300220.

[63] Edmund J. Copeland, M. Sami, and Shinji Tsujikawa. “Dynamics of Dark Energy”. In: *International Journal of Modern Physics D* 15.11 (Nov. 2006). doi: 10.1142/S021827180600942X. arXiv: hep-th/0603057. url: http://arxiv.org/abs/hep-th/0603057.

[64] Timothy Clifton et al. “Modified Gravity and Cosmology”. In: *Phys. Rept.* 513 (2012). doi: 10.1016/j.physrep.2012.01.001.

[65] Austin Joyce et al. “Beyond the Cosmological Standard Model”. In: *Phys. Rept.* 568 (2015). doi: 10.1016/j.physrep.2014.12.002.

[66] Andrew R. Liddle and D. H. Lyth. *Cosmological Inflation and Large Scale Structure*. 2000. doi: 10.1017/CBO9781139175180.

[67] Alan H. Guth. “The Inflationary Universe: A Possible Solution to the Horizon and Flatness Problems”. In: *Phys. Rev. D* 23 (1981). Ed. by Li-Zhi Fang and R. Ruffini. doi: 10.1103/PhysRevD.23.347.

[68] Alexander M. Polyakov. “Particle Spectrum in Quantum Field Theory”. In: *JETP Lett.* 20 (1974). Ed. by J. C. Taylor.

[69] Gerard ’t Hooft. “Magnetic Monopoles in Unified Gauge Theories”. In: *Nucl. Phys. B* 79 (1974). Ed. by J. C. Taylor. doi: 10.1016/0550-3213(74)90486-6.

[70] Michael B. Green, John H. Schwarz, and Edward Witten. *Superstring Theory Vol. 2: 25th Anniversary Edition*. Cambridge Monographs on Mathematical Physics. Cambridge University Press, Nov. 2012. doi: 10.1017/CBO9781139248570.

[71] John Preskill. “Cosmological Production of Superheavy Magnetic Monopoles”. In: *Phys. Rev. Lett.* 43 (1979). doi: 10.1103/PhysRevLett.43.1365.

[72] B. Acharya et al. “Search for Magnetic Monopoles with the MoEDAL Forward Trapping Detector in 13 TeV Proton-Proton Collisions at the LHC”. In: *Physical Review Letters* 118.6 (Feb. 10, 2017). doi: 10.1103/PhysRevLett.118.061801. url: https://link.aps.org/doi/10.1103/PhysRevLett.118.061801.

[73] M. Ambrosio et al. “Final Results of Magnetic Monopole Searches with the MACRO Experiment”. In: *Eur. Phys. J. C* 25 (2002). doi: 10.1140/epjc/s2002-01046-9.

[74] Charles W. Misner. “The Isotropy of the Universe”. In: *The Astrophysical Journal* 151 (Feb. 1, 1968). doi: 10.1086/149448. url: https://ui.adsabs.harvard.edu/abs/1968ApJ...151..431M.

[75] Y. Akrami et al. “Planck 2018 Results. X. Constraints on Inflation”. In: *Astron. Astrophys.* 641 (2020). doi: 10.1051/0004-6361/201833887.

[76] Tamara M. Davis and Charles H. Lineweaver. “Expanding Confusion: Common Misconceptions of Cosmological Horizons and the Superluminal Expansion of the Universe”. In: *Publications of the Astronomical Society of Australia* 21.1 (2004). doi: 10.1071/AS03040. arXiv: astro-ph/0310808. url: http://arxiv.org/abs/astro-ph/0310808.

[77] Edward W. Kolb. *The Early Universe*. Vol. 69. Taylor and Francis, May 2019. doi: 10.1201/9780429492860.

[78] V. Mukhanov. *Physical Foundations of Cosmology*. Oxford: Cambridge University Press, 2005. doi: 10.1017/CBO9780511790553.

[79] N. Aghanim et al. “Planck 2018 Results. I. Overview and the Cosmological Legacy of Planck”. In: *Astron. Astrophys.* 641 (2020). doi: 10.1051/0004-6361/201833880.

[80] Andrei D. Linde. *Particle Physics and Inflationary Cosmology*. Vol. 5. 1990.

[81] Andrei D. Linde. “Monopoles as Big as a Universe”. In: *Phys. Lett. B* 327 (1994). doi: 10.1016/0370-2693(94)90719-6.

[82] Phillip James Edwin Peebles. *Principles of Physical Cosmology*. Princeton University Press, May 9, 1993. 742 pp. Google Books: AmlEt6TJ6jAC.

[83] Andrei D. Linde. “A New Inflationary Universe Scenario: A Possible Solution of the Horizon, Flatness, Homogeneity, Isotropy and Primordial Monopole Problems”. In: *Phys. Lett. B* 108 (1982). Ed. by Li-Zhi Fang and R. Ruffini. doi: 10.1016/0370-2693(82)91219-9.

[84] John Ellis and David Wands. *Inflation (2023)*. Dec. 20, 2023. arXiv: 2312.13238. url: http://arxiv.org/abs/2312.13238. Pre-published.

[85] Jerome Martin. “The Theory of Inflation”. In: *Proc. Int. Sch. Phys. Fermi* 200 (2020). Ed. by E. Coccia, J. Silk, and N. Vittorio. doi: 10.3254/ENFI200008.

[86] Andrei D. Linde. “Chaotic Inflation”. In: *Phys. Lett. B* 129 (1983). doi: 10.1016/0370-2693(83)90837-7.

[87] L. F. Abbott and Mark B. Wise. “Constraints on Generalized Inflationary Cosmologies”. In: *Nuclear Physics B* 244.2 (Oct. 1, 1984). doi: 10.1016/0550-3213(84)90329-8. url: https://www.sciencedirect.com/science/article/pii/0550321384903298.

[88] F. Lucchin and S. Matarrese. “Power-Law Inflation”. In: *Physical Review D* 32.6 (Sept. 15, 1985). doi: 10.1103/PhysRevD.32.1316. url: https://link.aps.org/doi/10.1103/PhysRevD.32.1316.

[89] J. J. Halliwell. “Scalar Fields in Cosmology with an Exponential Potential”. In: *Physics Letters B* 185.3 (Feb. 19, 1987). doi: 10.1016/0370-2693(87)91011-2. url: https://www.sciencedirect.com/science/article/pii/0370269387910112.

[90] Christian T Byrnes, Ki-Young Choi, and Lisa M H Hall. “Conditions for Large Non-Gaussianity in Two-Field Slow-Roll Inflation”. In: *Journal of Cosmology and Astroparticle Physics* 2008.10 (Oct. 2008). doi: 10.1088/1475-7516/2008/10/008. url: https://dx.doi.org/10.1088/1475-7516/2008/10/008.

[91] David Polarski and Alexei A. Starobinsky. “Spectra of Perturbations Produced by Double Inflation with an Intermediate Matter Dominated Stage”. In: *Nucl. Phys. B* 385 (1992). doi: 10.1016/0550-3213(92)90062-G.

[92] Fedor L. Bezrukov and Mikhail Shaposhnikov. “The Standard Model Higgs Boson as the Inflaton”. In: *Phys. Lett. B* 659 (2008). doi: 10.1016/j.physletb.2007.11.072.

[93] Andrei Linde. “Hybrid Inflation”. In: *Physical Review D* 49.2 (Jan. 15, 1994). doi: 10.1103/PhysRevD.49.748. arXiv: astro-ph/9307002. url: http://arxiv.org/abs/astro-ph/9307002.

[94] A. D. Dolgov and A. D. Linde. “Baryon Asymmetry in the Inflationary Universe”. In: *Physics Letters B* 116.5 (Oct. 21, 1982). doi: 10.1016/0370-2693(82)90292-1. url: https://www.sciencedirect.com/science/article/pii/0370269382902921.

[95] Lev Kofman, Andrei Linde, and Alexei A. Starobinsky. “Reheating after Inflation”. In: *Physical Review Letters* 73.24 (Dec. 12, 1994). doi: 10.1103/PhysRevLett.73.3195. url: https://link.aps.org/doi/10.1103/PhysRevLett.73.3195.

[96] Alan H. Guth and S. Y. Pi. “Fluctuations in the New Inflationary Universe”. In: *Phys. Rev. Lett.* 49 (1982). doi: 10.1103/PhysRevLett.49.1110.

[97] S. W. Hawking. “The Development of Irregularities in a Single Bubble Inflationary Universe”. In: *Physics Letters B* 115.4 (Sept. 9, 1982). doi: 10.1016/0370-2693(82)90373-2. url: https://www.sciencedirect.com/science/article/pii/0370269382903732.

[98] James M. Bardeen, Paul J. Steinhardt, and Michael S. Turner. “Spontaneous Creation of Almost Scale-Free Density Perturbations in an Inflationary Universe”. In: *Physical Review D* 28.4 (Aug. 15, 1983). doi: 10.1103/PhysRevD.28.679. url: https://link.aps.org/doi/10.1103/PhysRevD.28.679.

[99] Lauren Anderson et al. “The Clustering of Galaxies in the SDSS-III Baryon Oscillation Spectroscopic Survey: Baryon Acoustic Oscillations in the Data Releases 10 and 11 Galaxy Samples”. In: *Mon. Not. Roy. Astron. Soc.* 441.1 (2014). doi: 10.1093/mnras/stu523.

[100] A. Vilenkin and E. P. S. Shellard. *Cosmic Strings and Other Topological Defects*. Cambridge University Press, July 2000.

[101] Robert H. Brandenberger. “Topological Defects and Structure Formation”. In: *International Journal of Modern Physics A* 09.13 (May 20, 1994). doi: 10.1142/S0217751X9400090X. arXiv: astro-ph/9310041. url: http://arxiv.org/abs/astro-ph/9310041.

[102] Ruth Durrer. “Cosmological Structure Formation with Topological Defects”. In: *35th Rencontres de Moriond: Energy Densities in the Universe*. 2000.

[103] L. Sousa and P. P. Avelino. “Cosmic Microwave Background Anisotropies Generated by Domain Wall Networks”. In: *Physical Review D* 92.8 (Oct. 20, 2015). doi: 10.1103/PhysRevD.92.083520. arXiv: 1507.01064. url: http://arxiv.org/abs/1507.01064.

[104] Neil Bevis et al. “CMB Power Spectrum Contribution from Cosmic Strings Using Field-Evolution Simulations of the Abelian Higgs Model”. In: *Physical Review D* 75.6 (Mar. 19, 2007). doi: 10.1103/PhysRevD.75.065015. arXiv: astro-ph/0605018. url: http://arxiv.org/abs/astro-ph/0605018.

[105] A. Lazanu, C. J. A. P. Martins, and E. P. S. Shellard. “Contribution of Domain Wall Networks to the CMB Power Spectrum”. In: *Physics Letters B* 747 (July 2015). doi: 10.1016/j.physletb.2015.06.034. arXiv: 1505.03673. url: http://arxiv.org/abs/1505.03673.

[106] Steven Weinberg. “A Model of Leptons”. In: *Phys. Rev. Lett.* 19 (1967). doi: 10.1103/PhysRevLett.19.1264.

[107] Graham G. Ross. *Grand Unified Theories*. Benjamin/Cummings Publishing Company, 1984. 520 pp. Google Books: Wl4sAAAAYAAJ.

[108] Sidney Coleman. “Fate of the False Vacuum: Semiclassical Theory”. In: *Physical Review D* 15.10 (May 15, 1977). doi: 10.1103/PhysRevD.15.2929. url: https://link.aps.org/doi/10.1103/PhysRevD.15.2929.

[109] Sidney Coleman and Frank De Luccia. “Gravitational Effects on and of Vacuum Decay”. In: *Physical Review D* 21.12 (June 15, 1980). doi: 10.1103/PhysRevD.21.3305. url: https://link.aps.org/doi/10.1103/PhysRevD.21.3305.

[110] T. W. B. Kibble. “Phase Transitions in the Early Universe”. In: *Jagellonian University. Institute of Physics. Acta Physica Polonica B* 13.ICTP-81-82-19 (1982).

[111] Tanmay Vachaspati. *Kinks and Domain Walls: An Introduction to Classical and Quantum Solitons*. Cambridge: Cambridge University Press, 2006. doi: 10.1017/CBO9780511535192. url: https://www.cambridge.org/core/books/kinks-and-domain-walls/98D525CCD885D53F51BDFC3B08A711A6.

[112] Blas Cabrera. “First Results from a Superconductive Detector for Moving Magnetic Monopoles”. In: *Physical Review Letters* 48.20 (May 17, 1982). doi: 10.1103/PhysRevLett.48.1378. url: https://link.aps.org/doi/10.1103/PhysRevLett.48.1378.

[113] Konstantinos Dimopoulos. “Primordial Magnetic Fields from Superconducting Cosmic Strings”. In: *Phys. Rev. D* 57 (1998). doi: 10.1103/PhysRevD.57.4629.

[114] Deepanshu Bisht et al. *Magnetic Field Amplification and Decay in Cosmic String Wakes*. Aug. 3, 2024. arXiv: 2408.01778. url: http://arxiv.org/abs/2408.01778. Pre-published.

[115] Dilip Kumar and Soma Sanyal. “Magnetic Reconnection in the Wakes of Cosmic Strings”. In: *Astrophys. J.* 944.2 (2023). doi: 10.3847/1538-4357/acb4ef.

[116] Andrew A. de Laix, Lawrence M. Krauss, and Tanmay Vachaspati. “Gravitational Lensing Signature of Long Cosmic Strings”. In: *Physical Review Letters* 79.11 (Sept. 15, 1997). doi: 10.1103/PhysRevLett.79.1968. url: https://link.aps.org/doi/10.1103/PhysRevLett.79.1968.

[117] M. V. Sazhin et al. “Gravitational Lensing by Cosmic Strings: What We Learn from the CSL-1 Case”. In: *Monthly Notices of the Royal Astronomical Society* 376 (Apr. 1, 2007). doi: 10.1111/j.1365-2966.2007.11543.x. url: https://ui.adsabs.harvard.edu/abs/2007MNRAS.376.1731S.

[118] Hayato Motohashi and Teruaki Suyama. “Detecting Cosmic String Passage through the Earth by Consequent Global Earthquake”. In: *Astrophysics and Space Science* 348.2 (Dec. 2013). doi: 10.1007/s10509-013-1591-2. arXiv: 1305.6676. url: http://arxiv.org/abs/1305.6676.

[119] Sameer Ahmed et al. *Black Hole Spin-down via Cosmic Strings*. July 3, 2024. arXiv: 2407.04743. url: http://arxiv.org/abs/2407.04743. Pre-published.

[120] B. P. Abbott et al. “Observation of Gravitational Waves from a Binary Black Hole Merger”. In: *Physical Review Letters* 116.6 (Feb. 11, 2016). doi: 10.1103/PhysRevLett.116.061102. url: https://link.aps.org/doi/10.1103/PhysRevLett.116.061102.

[121] Ajit Kumar Mehta et al. “New Binary Black Hole Mergers in the LIGO-Virgo O3b Data”. In: (Nov. 2023).

[122] Pierre Binétruy et al. “Cosmological Backgrounds of Gravitational Waves and eLISA/NGO: Phase Transitions, Cosmic Strings and Other Sources”. In: *Journal of Cosmology and Astroparticle Physics* 2012.06 (June 13, 2012). doi: 10.1088/1475-7516/2012/06/027. arXiv: 1201.0983. url: http://arxiv.org/abs/1201.0983.

[123] Yanou Cui et al. “Cosmic Archaeology with Gravitational Waves from Cosmic Strings”. In: *Physical Review D: Particles and Fields* 97.KCL-PH-TH-2017-51 (12 2018). doi: 10.1103/PhysRevD.97.123505. arXiv: 1711.03104.

[124] Sophie Henrot-Versillé et al. “Improved Constraint on the Primordial Gravitational-Wave Density Using Recent Cosmological Data and Its Impact on Cosmic String Models”. In: *Classical and Quantum Gravity* 32.4 (Feb. 19, 2015). doi: 10.1088/0264-9381/32/4/045003. arXiv: 1408.5299. url: http://arxiv.org/abs/1408.5299.

[125] Lara Sousa and Pedro P. Avelino. “Probing Cosmic Superstrings with Gravitational Waves”. In: *Physical Review D* 94.6 (Sept. 28, 2016). doi: 10.1103/PhysRevD.94.063529. arXiv: 1606.05585. url: http://arxiv.org/abs/1606.05585.

[126] The LIGO Scientific Collaboration et al. “Constraints on Cosmic Strings Using Data from the Third Advanced LIGO-Virgo Observing Run”. Jan. 28, 2021. arXiv: 2101.12248. url: http://arxiv.org/abs/2101.12248.

[127] Lara Sousa, Pedro P. Avelino, and Guilherme S. F. Guedes. “Full Analytical Approximation to the Stochastic Gravitational Wave Background Generated by Cosmic String Networks”. In: *Physical Review D* 101.10 (May 7, 2020). doi: 10.1103/PhysRevD.101.103508. arXiv: 2002.01079. url: http://arxiv.org/abs/2002.01079.

[128] L. Sousa and P. P. Avelino. “Stochastic Gravitational Wave Background Generated by Cosmic String Networks: Velocity-Dependent One-Scale Model versus Scale-Invariant Evolution”. In: *Physical Review D* 88.2 (July 16, 2013). doi: 10.1103/PhysRevD.88.023516. arXiv: 1304.2445. url: http://arxiv.org/abs/1304.2445.

[129] L. Sousa and P. P. Avelino. “The Stochastic Gravitational Wave Background Generated by Cosmic String Networks: The Small-Loop Regime”. In: *Physical Review D* 89.8 (Mar. 31, 2014). doi: 10.1103/PhysRevD.89.083503. arXiv: 1403.2621. url: http://arxiv.org/abs/1403.2621.

[130] I. Dankovsky et al. *Numerical Analysis of Melting Domain Walls and Their Gravitational Waves*. Oct. 29, 2024. arXiv: 2410.21971. url: http://arxiv.org/abs/2410.21971. Pre-published.

[131] Ricardo Z. Ferreira et al. “Gravitational Waves from Domain Walls in Pulsar Timing Array Datasets”. In: *JCAP* 02.CERN-TH-2022-214 (2023). doi: 10.1088/1475-7516/2023/02/001. arXiv: 2204.04228.

[132] Shuailiang Ge. “Stochastic Gravitational Wave Background: Birth from String-Wall Death”. In: *Journal of Cosmology and Astroparticle Physics* 2024.06 (June 1, 2024). doi: 10.1088/1475-7516/2024/06/064. arXiv: 2307.08185. url: http://arxiv.org/abs/2307.08185.

[133] Kenji Kadota, Masahiro Kawasaki, and Ken’ichi Saikawa. “Gravitational Waves from Domain Walls in the Next-to-Minimal Supersymmetric Standard Model”. In: *Journal of Cosmology and Astroparticle Physics* 2015.10 (Oct. 16, 2015). doi: 10.1088/1475-7516/2015/10/041. arXiv: 1503.06998. url: http://arxiv.org/abs/1503.06998.

[134] Naoya Kitajima and Fuminobu Takahashi. “Gravitational Waves from Higgs Domain Walls”. In: *Physics Letters B* 745.TU-991, IPMU15-0016 (2015). doi: 10.1016/j.physletb.2015.04.040. arXiv: 1502.03725.

[135] Tomasz Krajewski et al. “Domain Walls and Gravitational Waves in the Standard Model”. In: *Journal of Cosmology and Astroparticle Physics* 2016.12 (Dec. 19, 2016). doi: 10.1088/1475-7516/2016/12/036. arXiv: 1608.05719. url: http://arxiv.org/abs/1608.05719.

[136] Zhao Zhang et al. “Nano-Hertz Gravitational Waves from Collapsing Domain Walls Associated with Freeze-in Dark Matter in Light of Pulsar Timing Array Observations”. In: *Physical Review D: Particles and Fields* 108.9 (2023). doi: 10.1103/PhysRevD.108.095037. arXiv: 2307.11495.

[137] Daniel G. Figueroa et al. “Irreducible Background of Gravitational Waves from a Cosmic Defect Network: Update and Comparison of Numerical Techniques”. In: *Physical Review D* 102.10 (Nov. 13, 2020). doi: 10.1103/PhysRevD.102.103516. arXiv: 2007.03337. url: http://arxiv.org/abs/2007.03337.

[138] Takashi Hiramatsu et al. “Production of Dark Matter Axions from Collapse of String-Wall Systems”. In: *Physical Review D* 86.8 (Oct. 15, 2012). doi: 10.1103/PhysRevD.86.089902. arXiv: 1202.5851. url: http://arxiv.org/abs/1202.5851.

[139] Masahiro Kawasaki, Ken’ichi Saikawa, and Toyokazu Sekiguchi. “Axion Dark Matter from Topological Defects”. In: *Physical Review D* 91.6 (Mar. 12, 2015). doi: 10.1103/PhysRevD.91.065014. arXiv: 1412.0789. url: http://arxiv.org/abs/1412.0789.

[140] David I. Dunsky and Marius Kongsore. “Primordial Black Holes from Axion Domain Wall Collapse”. In: *JHEP* 06 (2024). doi: 10.1007/JHEP06(2024)198.

[141] Jing Liu, Zong-Kuan Guo, and Rong-Gen Cai. “Primordial Black Holes from Cosmic Domain Walls”. In: *Physical Review D* 101.2 (Jan. 14, 2020). doi: 10.1103/PhysRevD.101.023513. arXiv: 1908.02662. url: http://arxiv.org/abs/1908.02662.

[142] Robert R. Caldwell and Marc Kamionkowski. “The Physics of Cosmic Acceleration”. In: *Annual Review of Nuclear and Particle Science* 59.1 (Nov. 2009). doi: 10.1146/annurev-nucl-010709-151330. arXiv: 0903.0866. url: http://arxiv.org/abs/0903.0866.

[143] P. P. Avelino et al. “Scaling of Cosmological Domain Wall Networks with Junctions”. In: *Physics Letters B* 647.2-3 (Apr. 2007). doi: 10.1016/j.physletb.2007.02.025. arXiv: astro-ph/0612444. url: http://arxiv.org/abs/astro-ph/0612444.

[144] P. P. Avelino et al. “Dynamics of Domain Wall Networks with Junctions”. In: *Physical Review D* 78.10 (Nov. 7, 2008). doi: 10.1103/PhysRevD.78.103508. arXiv: 0807.4442. url: http://arxiv.org/abs/0807.4442.

[145] L. Sousa and P. P. Avelino. “Impact of String and Monopole-Type Junctions on Domain Wall Dynamics: Implications for Dark Energy”. In: *Physics Letters B* 689.4-5 (May 2010). doi: 10.1016/j.physletb.2010.04.074. arXiv: 0911.3902. url: http://arxiv.org/abs/0911.3902.

[146] Valentin V. Khoze and Daniel L. Milne. “Optical Effects of Domain Walls”. In: *Physics Letters B* 829 (June 2022). doi: 10.1016/j.physletb.2022.137044. arXiv: 2107.02640. url: http://arxiv.org/abs/2107.02640.

[147] M. Pospelov et al. “How Do You Know If You Ran through a Wall?” In: *Physical Review Letters* 110.2 (Jan. 11, 2013). doi: 10.1103/PhysRevLett.110.021803. arXiv: 1205.6260. url: http://arxiv.org/abs/1205.6260.

[148] Ya. B. Zeldovich, I. Yu. Kobzarev, and L. B. Okun. “Cosmological Consequences of the Spontaneous Breakdown of Discrete Symmetry”. In: *Zhurnal Eksperimental’noi i Teoreticheskoi Fiziki* 67.SLAC-TRANS-0165, IPM-MOSCOW-15 (1974).

[149] P. P. Avelino, C. J. A. P. Martins, and L. Sousa. “Dynamics of Biased Domain Walls and the Devaluation Mechanism”. In: *Physical Review D* 78.4 (Aug. 13, 2008). doi: 10.1103/PhysRevD.78.043521. arXiv: 0805.4013. url: http://arxiv.org/abs/0805.4013.

[150] Richard A. Battye, Apostolos Pilaftsis, and Dominic G. Viatic. “Domain Wall Constraints on Two Higgs Doublet Models with Z_2 Symmetry”. In: *Physical Review D* 102.12 (Dec. 23, 2020). doi: 10.1103/PhysRevD.102.123536. arXiv: 2010.09840. url: http://arxiv.org/abs/2010.09840.

[151] J. R. C. C. C. Correia, I. S. C. R. Leite, and C. J. A. P. Martins. “Effects of Biases in Domain Wall Network Evolution. II. Quantitative Analysis”. In: *Physical Review D* 97.8 (Apr. 27, 2018). doi: 10.1103/PhysRevD.97.083521. arXiv: 1804.10761. url: http://arxiv.org/abs/1804.10761.

[152] Tomasz Krajewski et al. “Stability of Domain Walls in Models with Asymmetric Potentials”. Mar. 4, 2021. arXiv: 2103.03225. url: http://arxiv.org/abs/2103.03225.

[153] D. Coulson, Z. Lalak, and B. Ovrut. “Biased Domain Walls”. In: *Physical Review D* 53.8 (Apr. 1996). doi: 10.1103/PhysRevD.53.4237. url: https://link.aps.org/doi/10.1103/PhysRevD.53.4237.

[154] J. R. C. C. C. Correia, I. S. C. R. Leite, and C. J. A. P. Martins. “Effects of Biases in Domain Wall Network Evolution”. In: *Physical Review D* 90.2 (July 2014). doi: 10.1103/PhysRevD.90.023521. url: https://link.aps.org/doi/10.1103/PhysRevD.90.023521.

[155] Oriol Pujolas and George Zahariade. “Domain Wall Annihilation – a QFT Perspective”. In: *Physical Review D* 107.12 (June 20, 2023). doi: 10.1103/PhysRevD.107.123527. arXiv: 2212.11204. url: http://arxiv.org/abs/2212.11204.

[156] William H. Press, Barbara S. Ryden, and David N. Spergel. “Dynamical Evolution of Domain Walls in an Expanding Universe”. In: *Astrophysical Journal, Part 1 (ISSN 0004-637X), vol. 347, Dec. 15, 1989, p. 590-604. Research supported by NASA and Alfred P. Sloan Foundation.* 347 (Dec. 1, 1989). doi: 10.1086/168151. url: http://adsabs.harvard.edu/abs/1989ApJ...347..590P.

[157] J. R. C. C. C. Correia and C. J. A. P. Martins. “General Purpose Graphics-Processing-Unit Implementation of Cosmological Domain Wall Network Evolution”. In: *Physical Review E* 96.4 (Oct. 26, 2017). doi: 10.1103/PhysRevE.96.043310. arXiv: 1710.10420. url: http://arxiv.org/abs/1710.10420.

[158] A. M. M. Leite and C. J. A. P. Martins. “Scaling Properties of Domain Wall Networks”. In: *Physical Review D* 84.10 (Nov. 22, 2011). doi: 10.1103/PhysRevD.84.103523. arXiv: 1110.3486. url: http://arxiv.org/abs/1110.3486.

[159] C. J. A. P. Martins et al. “Extending the Velocity-Dependent One-Scale Model for Domain Walls”. In: *Physical Review D* 93.4 (Feb. 17, 2016). doi: 10.1103/PhysRevD.93.043534. arXiv: 1602.01322. url: http://arxiv.org/abs/1602.01322.

[160] Naoya Kitajima et al. “Stability of Domain Walls with Inflationary Fluctuations under Potential Bias, and Gravitational Wave Signatures”. Nov. 2023. arXiv: 2311.14590.

[161] Claudio Llinares and Levon Pogosian. “Domain Walls Coupled to Matter: The Symmetron Example”. In: *Physical Review D* 90.12 (Dec. 15, 2014). doi: 10.1103/PhysRevD.90.124041. arXiv: 1410.2857. url: http://arxiv.org/abs/1410.2857.

[162] Jonathan A. Pearson. “Simulating the Symmetron: Domain Walls and Symmetry-Restoring Impurities”. In: *Physical Review D* 90.12 (Dec. 16, 2014). doi: 10.1103/PhysRevD.90.125011. arXiv: 1409.6570. url: http://arxiv.org/abs/1409.6570.

[163] De-Chang Dai, Djordje Minic, and Dejan Stojkovic. “Interaction of Cosmological Domain Walls with Large Classical Objects, like Planets and Satellites, and the Flyby Anomaly”. In: ().

[164] J. R. C. C. C. Correia and C. J. A. P. Martins. “Extending and Calibrating the Velocity Dependent One-Scale Model for Cosmic Strings with One Thousand Field Theory Simulations”. In: *Physical Review D* 100.10 (Nov. 13, 2019). doi: 10.1103/PhysRevD.100.103517. arXiv: 1911.03163. url: http://arxiv.org/abs/1911.03163.

[165] Theodore Garagounis and Mark Hindmarsh. “Scaling in Numerical Simulations of Domain Walls”. In: *Physical Review D* 68.10 (Nov. 17, 2003). doi: 10.1103/PhysRevD.68.103506. arXiv: hep-ph/0212359. url: http://arxiv.org/abs/hep-ph/0212359.

[166] A. M. M. Leite, C. J. A. P. Martins, and E. P. S. Shellard. “Accurate Calibration of the Velocity-dependent One-scale Model for Domain Walls”. In: *Physics Letters B* 718.3 (Jan. 2013). doi: 10.1016/j.physletb.2012.11.070. arXiv: 1206.6043. url: http://arxiv.org/abs/1206.6043.

[167] P. P. Avelino. “Parameter-Free Velocity-Dependent One-Scale Model for Domain Walls”. In: *Physical Review D* 101.2 (Jan. 15, 2020). doi: 10.1103/PhysRevD.101.023514. arXiv: 1910.07011. url: http://arxiv.org/abs/1910.07011.

[168] J. Alexandre and D. Tanner. “Quantization Leading to a Natural Flattening of the Axion Potential”. In: *Phys. Rev. D* 82 (2010). doi: 10.1103/PhysRevD.82.125035.

[169] Clay Cordova, Sungwoo Hong, and Lian-Tao Wang. “Axion Domain Walls, Small Instantons, and Non-Invertible Symmetry Breaking”. In: *JHEP* 05 (2024). doi: 10.1007/JHEP05(2024)325.

[170] Michael Dine. “Remarks on the Axion Domain Wall Problem”. In: (July 2023).

[171] C. J. A. P. Martins and E. P. S. Shellard. “Quantitative String Evolution”. In: *Physical Review D* 54.4 (Aug. 15, 1996). doi: 10.1103/PhysRevD.54.2535. arXiv: hep-ph/9602271. url: http://arxiv.org/abs/hep-ph/9602271.

[172] P. P. Avelino and L. Sousa. “Domain Wall Network Evolution in (N+1)-Dimensional FRW Universes”. In: *Physical Review D* 83.4 (Feb. 28, 2011). doi: 10.1103/PhysRevD.83.043530. arXiv: 1101.3360. url: http://arxiv.org/abs/1101.3360.

[173] P. P. Avelino, R. Menezes, and L. Sousa. “P-Brane Dynamics in N+1-Dimensional FRW Universes”. In: *Physical Review D* 79.4 (Feb. 23, 2009). doi: 10.1103/PhysRevD.79.043519. arXiv: 0811.1580. url: http://arxiv.org/abs/0811.1580.

[174] L. Sousa and P. P. Avelino. “The Cosmological Evolution of P-Brane Networks”. In: *Phys. Rev. D* 84 (2011). doi: 10.1103/PhysRevD.84.063502.

[175] Ivan Rybak. “Cosmic Paleontology: Searching for Superstrings”. In: ().

[176] C. J. A. P. Martins et al. “Stretching and Kibble Scaling Regimes for Hubble-damped Defect Networks”. In: *Physical Review D* 94.11 (Dec. 27, 2016). doi: 10.1103/PhysRevD.94.116017. arXiv: 1612.08863. url: http://arxiv.org/abs/1612.08863.

[177] C. J. A. P. Martins and M. M. P. V. P. Cabral. “Physical and Invariant Models for Defect Network Evolution”. In: *Physical Review D* 93.4 (Feb. 25, 2016). doi: 10.1103/PhysRevD.93.043542. arXiv: 1602.08083. url: http://arxiv.org/abs/1602.08083.

[178] Simone Blasi et al. “Friction on ALP Domain Walls and Gravitational Waves”. In: *JCAP* 04 (2023). doi: 10.1088/1475-7516/2023/04/008. arXiv: 2210.14246.

[179] P. P. Avelino, C. J. A. P. Martins, and J. C. R. E. Oliveira. “One-Scale Model for Domain Wall Network Evolution”. In: *Physical Review D* 72.8 (Oct. 7, 2005). doi: 10.1103/PhysRevD.72.083506. arXiv: hep-ph/0507272. url: http://arxiv.org/abs/hep-ph/0507272.

[180] Tanmay Vachaspati, Allen E. Everett, and Alexander Vilenkin. “Radiation from Vacuum Strings and Domain Walls”. In: *Physical Review D* 30.10 (Nov. 15, 1984). doi: 10.1103/PhysRevD.30.2046. url: https://link.aps.org/doi/10.1103/PhysRevD.30.2046.

[181] Sebastian E. Larsson, Subir Sarkar, and Peter L. White. “Evading the Cosmological Domain Wall Problem”. In: *Phys. Rev. D* 55 (1997). doi: 10.1103/PhysRevD.55.5129.

[182] Graciela B. Gelmini, Marcelo Gleiser, and Edward W. Kolb. “Cosmology of Biased Discrete Symmetry Breaking”. In: *Phys. Rev. D* 39 (1989). doi: 10.1103/PhysRevD.39.1558.

[183] Chandrasekar Chatterjee, Tetsutaro Higaki, and Muneto Nitta. “Note on a Solution to Domain Wall Problem with the Lazarides-Shafi Mechanism in Axion Dark Matter Models”. In: *Phys. Rev. D* 101.7 (2020). doi: 10.1103/PhysRevD.101.075026.

[184] Keisuke Harigaya and Masahiro Kawasaki. “QCD Axion Dark Matter from Long-Lived Domain Walls during Matter Domination”. In: *Phys. Lett. B* 782 (2018). doi: 10.1016/j.physletb.2018.04.056.

[185] Konstantin A. Beyer and Subir Sarkar. “Ruling out Light Axions: The Writing Is on the Wall”. In: *SciPost Phys.* 15.1 (2023). doi: 10.21468/SciPostPhys.15.1.003.

[186] Jose J. Blanco-Pillado et al. “Effective Actions for Domain Wall Dynamics”. In: (Nov. 2024).

[187] L. Sousa and P. P. Avelino. “Evolution of Domain Wall Networks: The PRS Algorithm”. In: *Physical Review D* 81.8 (Apr. 30, 2010). doi: 10.1103/PhysRevD.81.087305. arXiv: 1101.3350. url: http://arxiv.org/abs/1101.3350.

[188] Peter Frolkovič. “Numerical Recipes: The Art of Scientific Computing”. In: *Acta Applicandae Mathematica* 19 (June 1990). doi: 10.1007/BF01321860.

[189] R. Courant, K. Friedrichs, and H. Lewy. “On the Partial Difference Equations of Mathematical Physics”. In: *IBM Journal of Research and Development* 11.2 (Mar. 1967). doi: 10.1147/rd.112.0215. url: https://ieeexplore.ieee.org/document/5391985.

[190] John von Neumann. “Discussion Remark Concerning Paper of C. S. Smith, “Grain shapes and other metallurgical applications of topology””. In: *Metal Interfaces*. 1952.

[191] P. P. Avelino, R. Menezes, and J. C. R. E. Oliveira. “Unified Paradigm for Interface Dynamics”. In: *Physical Review E* 83.1 (Jan. 14, 2011). doi: 10.1103/PhysRevE.83.011602. arXiv: 1006.3564. url: http://arxiv.org/abs/1006.3564.

[192] Sascha Hilgenfeldt et al. “An Accurate von Neumann’s Law for Three-Dimensional Foams”. In: *Physical Review Letters* 86.12 (Mar. 19, 2001). doi: 10.1103/PhysRevLett.86.2685. url: https://link.aps.org/doi/10.1103/PhysRevLett.86.2685.

[193] Robert D. MacPherson and David J. Srolovitz. “The von Neumann Relation Generalized to Coarsening of Three-Dimensional Microstructures”. In: *Nature* 446.7139 (Apr. 2007). doi: 10.1038/nature05745. url: https://www.nature.com/articles/nature05745.

[194] “Evolution of a System of Cosmic Strings”. In: *Nuclear Physics B* 261 (Jan. 1, 1985). doi: 10.1016/0550-3213(85)90596-6. url: https://www.sciencedirect.com/science/article/pii/0550321385905966.

[195] P. P. Avelino. “Comparing Parametric and Non-Parametric Velocity-Dependent One-Scale Models for Domain Wall Evolution”. In: *Journal of Cosmology and Astroparticle Physics* 2020.04 (Apr. 9, 2020). doi: 10.1088/1475-7516/2020/04/012. arXiv: 2001.06318. url: http://arxiv.org/abs/2001.06318.

[196] Lawrence M. Widrow. “Dynamics of Thick Domain Walls”. In: *Physical Review D* 40.4 (Aug. 15, 1989). doi: 10.1103/PhysRevD.40.1002. url: https://link.aps.org/doi/10.1103/PhysRevD.40.1002.

[197] Mark Hindmarsh et al. “Improving Cosmic String Network Simulations”. In: *Physical Review D* 90.4 (Aug. 29, 2014). doi: 10.1103/PhysRevD.90.043539. url: https://link.aps.org/doi/10.1103/PhysRevD.90.043539.

[198] Michel Peyrard and Martin D. Kruskal. “Kink Dynamics in the Highly Discrete Sine-Gordon System”. In: *Physica D: Nonlinear Phenomena* 14.1 (Dec. 1, 1984). doi: 10.1016/0167-2789(84)90006-X. url: https://www.sciencedirect.com/science/article/pii/016727898490006X.

[199] J. Ipser and P. Sikivie. “Gravitationally Repulsive Domain Wall”. In: *Physical Review D* 30.4 (Aug. 15, 1984). doi: 10.1103/PhysRevD.30.712. url: https://link.aps.org/doi/10.1103/PhysRevD.30.712.

[200] Archil Kobakhidze. “Domain Walls and Gauge Field Localization in Strongly-Coupled Pure Yang-Mills Theories”. In: *International Journal of Theoretical Physics* 50.5 (May 1, 2011). doi: 10.1007/s10773-010-0640-7. url: https://doi.org/10.1007/s10773-010-0640-7.

[201] Kurt Hinterbichler and Justin Khoury. “Symmetron Fields: Screening Long-Range Forces Through Local Symmetry Restoration”. In: *Physical Review Letters* 104.23 (June 10, 2010). doi: 10.1103/PhysRevLett.104.231301. arXiv: 1001.4525. url: http://arxiv.org/abs/1001.4525.

[202] Vakhid A. Gani, Alexander E. Kudryavtsev, and Mariya A. Lizunova. “Kink Interactions in the (1+1)-Dimensional \phi^6 Model”. In: *Phys. Rev. D* 89.12 (2014). doi: 10.1103/PhysRevD.89.125009.

[203] Avinash Khare and Avadh Saxena. “Domain Wall and Periodic Solutions of a Coupled Φ6 Model”. In: *Journal of Mathematical Physics* 49 (June 1, 2008). doi: 10.1063/1.2938691. url: https://ui.adsabs.harvard.edu/abs/2008JMP...49f3301K.

[204] Jose J. Blanco-Pillado et al. *The Dynamics of Domain Wall Strings*. Sept. 26, 2022. arXiv: 2209.12945. url: http://arxiv.org/abs/2209.12945. Pre-published.

[205] B. P. Abbott et al. “GW151226: Observation of Gravitational Waves from a 22-Solar-Mass Binary Black Hole Coalescence”. In: *Physical Review Letters* 116.LIGO-P151226 (24 2016). doi: 10.1103/PhysRevLett.116.241103. arXiv: 1606.04855.

[206] B. P. Abbott et al. “GW170817: Observation of Gravitational Waves from a Binary Neutron Star Inspiral”. In: *Physical Review Letters* 119.LIGO-P170817 (16 2017). doi: 10.1103/PhysRevLett.119.161101. arXiv: 1710.05832.

[207] Pau Amaro Seoane et al. “Astrophysics with the Laser Interferometer Space Antenna”. In: *Living Rev. Rel.* 26.1 (2023). doi: 10.1007/s41114-022-00041-y. arXiv: 2203.06016.

[208] Pierre Auclair et al. “Cosmology with the Laser Interferometer Space Antenna”. In: *Living Rev. Rel.* 26.LISA CosWG-22-03, FERMILAB-PUB-22-349-SCD (1 2023). doi: 10.1007/s41114-023-00045-2. arXiv: 2204.05434.

[209] Ning Chen, Tong Li, and Yongcheng Wu. “The Gravitational Waves from the Collapsing Domain Walls in the Complex Singlet Model”. In: *JHEP* 08 (2020). doi: 10.1007/JHEP08(2020)117. arXiv: 2004.10148.

[210] David I. Dunsky et al. “GUTs, Hybrid Topological Defects, and Gravitational Waves”. In: *Physical Review D: Particles and Fields* 106.7 (2022). doi: 10.1103/PhysRevD.106.075030. arXiv: 2111.08750.

[211] Charles Badger et al. “Probing Early Universe Supercooled Phase Transitions with Gravitational Wave Data”. In: *Physical Review D: Particles and Fields* 107.KCL-PH-TH-2022-43 (2 2023). doi: 10.1103/PhysRevD.107.023511. arXiv: 2209.14707.

[212] R. R. Caldwell and Bruce Allen. “Cosmological Constraints on Cosmic String Gravitational Radiation”. In: *Physical Review D: Particles and Fields* 45.WISC-MILW-91-TH-14 (1992). doi: 10.1103/PhysRevD.45.3447.

[213] Matthew R. DePies and Craig J. Hogan. “Stochastic Gravitational Wave Background from Light Cosmic Strings”. In: *Physical Review D: Particles and Fields* 75 (2007). doi: 10.1103/PhysRevD.75.125006. arXiv: astro-ph/0702335.

[214] S. A. Sanidas, R. A. Battye, and B. W. Stappers. “Constraints on Cosmic String Tension Imposed by the Limit on the Stochastic Gravitational Wave Background from the European Pulsar Timing Array”. In: *Physical Review D: Particles and Fields* 85 (2012). doi: 10.1103/PhysRevD.85.122003. arXiv: 1201.2419.

[215] Jose J. Blanco-Pillado, Ken D. Olum, and Benjamin Shlaer. “The Number of Cosmic String Loops”. In: *Physical Review D* 89.2 (Jan. 14, 2014). doi: 10.1103/PhysRevD.89.023512. arXiv: 1309.6637. url: http://arxiv.org/abs/1309.6637.

[216] G. S. F. Guedes, P. P. Avelino, and L. Sousa. “Signature of Inflation in the Stochastic Gravitational Wave Background Generated by Cosmic String Networks”. In: *Physical Review D: Particles and Fields* 98.12 (2018). doi: 10.1103/PhysRevD.98.123505. arXiv: 1809.10802.

[217] J. C. R. E. Oliveira, C. J. A. P. Martins, and P. P. Avelino. “The Cosmological Evolution of Domain Wall Networks”. Oct. 27, 2004. doi: 10.1103/PhysRevD.71.083509. arXiv: hep-ph/0410356. url: http://arxiv.org/abs/hep-ph/0410356.

[218] P. P. Avelino, J. C. R. E. Oliveira, and C. J. A. P. Martins. “Understanding Domain Wall Network Evolution”. In: *Physics Letters B* 610.1-2 (Mar. 2005). doi: 10.1016/j.physletb.2005.02.003. arXiv: hep-th/0503226. url: http://arxiv.org/abs/hep-th/0503226.

[219] Marcelo Gleiser and Ronald Roberts. “Gravitational Waves from Collapsing Vacuum Domains”. In: *Physical Review Letters* 81.25 (Dec. 21, 1998). doi: 10.1103/PhysRevLett.81.5497. arXiv: astro-ph/9807260. url: http://arxiv.org/abs/astro-ph/9807260.

[220] Masahiro Kawasaki and Ken’ichi Saikawa. “Study of Gravitational Radiation from Cosmic Domain Walls”. In: *JCAP* 09.ICRR-REPORT-581-2010-14, IPMU11-0032 (2011). doi: 10.1088/1475-7516/2011/09/008. arXiv: 1102.5628.

[221] Takashi Hiramatsu et al. “Axion Cosmology with Long-Lived Domain Walls”. In: *JCAP* 01.ICRR-REPORT-620-2012-9, IPMU12-0140, YITP-12-58 (2013). doi: 10.1088/1475-7516/2013/01/001. arXiv: 1207.3166.

[222] Ken'ichi Saikawa. "A Review of Gravitational Waves from Cosmic Domain Walls". In: *Universe* 3.2 (May 5, 2017). doi: 10.3390/universe3020040. arXiv: 1703.02576. url: http://arxiv.org/abs/1703.02576.

[223] Chiara Caprini et al. "General Properties of the Gravitational Wave Spectrum from Phase Transitions". In: *Physical Review D: Particles and Fields* 79 (2009). doi: 10.1103/PhysRevD.79.083519. arXiv: 0901.1661.

[224] Daniel Cutting, Mark Hindmarsh, and David J. Weir. "Gravitational Waves from Vacuum First-Order Phase Transitions: From the Envelope to the Lattice". In: *Physical Review D: Particles and Fields* 97.HIP-2018-4-TH (12 2018). doi: 10.1103/PhysRevD.97.123513. arXiv: 1802.05712.

[225] Rong-Gen Cai, Shi Pi, and Misao Sasaki. "Universal Infrared Scaling of Gravitational Wave Background Spectra". In: *Physical Review D: Particles and Fields* 102.IPMU19-0135, YITP-19-88 (8 2020). doi: 10.1103/PhysRevD.102.083528. arXiv: 1909.13728.

[226] Alexander Vilenkin. "Cosmic Strings and Domain Walls". In: *Phys. Rept.* 121.PRINT-84-0840 (TUFTS) (1985). doi: 10.1016/0370-1573(85)90033-X.

[227] Thomas J. Clarke, Edmund J. Copeland, and Adam Moss. "Constraints on Primordial Gravitational Waves from the Cosmic Microwave Background". In: *Journal of Cosmology and Astroparticle Physics* 2020.10 (Oct. 1, 2020). doi: 10.1088/1475-7516/2020/10/002. arXiv: 2004.11396. url: http://arxiv.org/abs/2004.11396.

[228] Michele Maggiore. "Gravitational Wave Experiments and Early Universe Cosmology". In: *Phys. Rept.* 331 (2000). doi: 10.1016/S0370-1573(99)00102-7.

[229] Gary Steigman. "Primordial Nucleosynthesis in the Precision Cosmology Era". In: *Ann. Rev. Nucl. Part. Sci.* 57 (2007). doi: 10.1146/annurev.nucl.56.080805.140437.

[230] Nicklas Ramberg, Wolfram Ratzinger, and Pedro Schwaller. "One μ to rule them all: CMB spectral distortions can probe domain walls, cosmic strings and low scale phase transitions". In: *JCAP* 02 (2023). doi: 10.1088/1475-7516/2023/02/039. arXiv: 2209.14313.

[231] Ricardo Z. Ferreira et al. "Axionic Defects in the CMB: Birefringence and Gravitational Waves". In: *JCAP* 05.RUP-23-27 (2024). doi: 10.1088/1475-7516/2024/05/066. arXiv: 2312.14104.

[232] Ricardo Z. Ferreira et al. “Collapsing Domain Wall Networks: Impact on Pulsar Timing Arrays and Primordial Black Holes”. Jan. 2024. arXiv: 2401.14331.

[233] Adeela Afzal et al. “The Nanograv 15 Yr Data Set: Search for Signals from New Physics”. In: *Astrophysical Journal, Letters to the Editor* 951.1 (2023). doi: 10.3847/2041-8213/acdc91. arXiv: 2306.16219.

[234] Naoya Kitajima et al. “Gravitational Waves from Domain Wall Collapse, and Application to Nanohertz Signals with QCD-coupled Axions”. June 2023. arXiv: 2306.17146.

[235] Yann Gouttenoire and Edoardo Vitagliano. “Domain Wall Interpretation of the PTA Signal Confronting Black Hole Overproduction”. June 2023. arXiv: 2306.17841.

[236] Gemma Janssen et al. “Gravitational Wave Astronomy with the SKA”. In: *PoS* AASKA14 (2015). Ed. by Tyler L. Bourke et al. doi: 10.22323/1.215.0037.

[237] R. Smits et al. “Pulsar Searches and Timing with the Square Kilometre Array”. In: *Astronomy & Astrophysics* 493.3 (3 Jan. 1, 2009). doi: 10.1051/0004-6361:200810383. url: https://www.aanda.org/articles/aa/abs/2009/03/aa10383-08/aa10383-08.html.

[238] Pierre Auclair et al. *Cosmic String Bursts in LISA*. May 19, 2023. arXiv: 2305.11653. url: http://arxiv.org/abs/2305.11653. Pre-published.

[239] Jose J. Blanco-Pillado et al. *Gravitational Waves from Cosmic Strings in LISA: Reconstruction Pipeline and Physics Interpretation*. May 6, 2024. arXiv: 2405.03740. url: http://arxiv.org/abs/2405.03740. Pre-published.